The compressible starting jet: fluid mechanics and acoustics

vorgelegt von
Dipl.-Ing.
Juan José Peña Fernández
geb. in Madrid

von der Fakultät V – Verkehrs- und Maschinensysteme
der Technischen Universität Berlin
zur Erlangung des akademischen Grades

Doktor der Ingenieurwissenschaften
-Dr.-Ing.-

genehmigte Dissertation

Promotionausschuss:

Vorsitzender:	Prof. Dr. Julius Reiß
Gutachter:	Prof. Dr. sc. techn. habil. Jörn Sesterhenn
Gutachter:	Prof. Dr. Christophe Bogey

Tag der wissenschaftlichen Aussprache: 21. September 2017

Berlin, 2018

To my family, friends and those who helped me on my way.

Zusammenfassung

Freistrahlen, auch "Jets" genannt, kommen häufig sowohl in industriellen Anwendungen als auch in der Natur vor, so zum Beispiel bei der Treibstoffeinspritzung, Strahltriebwerken, Vulkanausbrüchen, Airbags, aber auch Wasserstrahlschneidemaschinen, Raketenrucksäcke, Impfpistolen, kosmische Jets, usw.

Kontinuierliche Freistrahlen werden seit ungefähr einem Jahrhundert, sowohl im inkompressiblen als auch im kompressiblen Bereich untersucht. Der Fokus liegt dabei hauptsächlich auf der Beschreibung der Bewegung des Fluides bezüglich der Freistrahlachsen sowie dem Einfluss der wichtigsten Parameter.

Der startende Freistrahl wurde bisher nur im inkompressiblen Bereich untersucht und der Fokus lag auf der Beschreibung der Entwicklung des Ringwirbels. Der kompressible, startende Freistrahl kann als ein neues Thema betrachtet werden. In dieser Dissertation wird dieser Fall untersucht, verwendet wird dabei ein numerischer Ansatz, der auf finiten Differenzen basiert und diese in einem parallelen numerischen Code auf einem der größten Rechnenzentren Europas implementiert.

Zusätzlich werden Experimente sowohl im Labor als auch auf Vulkanen durchgeführt um die Akustik der auftretenden Freistrahlen zu untersuchen. Ein theoretischer Ansatz wird verfolgt um die Wirkung des Hauptparameters eines solchen Freistrahles abzuschätzen.

Der Hauptbeitrag dieser Dissertation ist die Verbindung zwischen der Fluiddynamik und der Akustik des kompressiblen startenden Freistrahls. Durch eine umfangreiche Analyse sowohl der Strömungsmechanik als auch der Akustik, haben wir zwei Art und Weisen gefunden, wie der ausgebildete Jet mit dem Ringwirbel, welcher beim Start entsteht, interagiert, wodurch zwei der lautesten Lärmquellen der startende Freistrahl entstehen:

(*i*) die ***Stoß–Scherschicht*** Interaktion ist der Mechanismus wodurch der "Broadband shock noise" entsteht und

(*ii*) die ***Stoß–Scherschicht–Ringwirbel*** Interaktion wurde erstmals gefunden; obwohl sie nur eine einzige Druckwelle generiert, hat sie eine höhere Amplitude als die des "Broadband shock noise".

Während der Detailstudie über die Grenze zwischen des Ringwirbels und des trailing Jets haben wir gefunden, dass die Anwendung einer Wirbelstärkeschwelle von $\omega_{\mathrm{po}}/\omega_{\mathrm{vortex}} = 0.1$ eine geeignetere Definition des Pinch-off ist als die vorherigen Methoden aus der Literatur, welche hauptsächlich auf optische Auswertungen basiert sind.

Wir konnten bestätigen, dass die Entwicklung der Position des Ringwirbels in der axialen und radialen Richtung $x_{\mathrm{VR}}/D \sim (t^*)^{1/2}$ und $R_{\mathrm{VR}}/D \sim (t^*)^{1/3}$ über einen substantiellen Zeitbereich folgt.

Wir konnten auch bestätigen, dass die Kompressibilität die Verbreitung

des Ringwirbels verzögert. Wir haben zusätzlich gefunden, dass für ein Turbulenzgrad von 10%, die Stoßzellen-Struktur noch erhalten ist.

Mit umfassende Kentnissen über sowohl die Strömungsmechanik als auch die Akustik des startenden Freistrahls, als auch der Verbindung zwischen beiden, sind wir in der Lage, die Hauptparameter durch akustische und optische Messungen abzuschätzen. Das ist besonders wichtig für Anwendungen, wo kein direkter Zugang zum Strahl möglich ist (zum Beispiel im Fall von Vulkanausbrüchen), aber auch für die Entwicklung neuer vulkanische Überwachungsmethoden.

Abstract

Jets are involved in numerous industrial applications and in nature: fuel injection, jet engines, volcanic jets, air-bag devices, but also water jet cutters, jet packs (rocket belts), jet injectors for vaccination, astrophysical jets, etc. Continuous jets have been already studied in the incompressible and compressible case for almost a century, focused mainly on the characterization of the fluid motion at the jet centerline and the effect of the governing parameters. The starting jet has been studied only in the incompressible case, focused mainly on the radial and axial characterization of the vortex ring. The compressible starting jet can be considered a new topic.

The compressible starting jet has been studied in this thesis mainly with a numerical approach using finite differences with a massively parallel code running in one of the biggest supercomputing centres in Europe. Nevertheless, experiments in both laboratory and active volcanoes have been also carried out mainly to study the acoustics emanated. A small, but not insignificant theoretical work was performed in order to estimate some flow properties when changing the governing parameters.

The main contribution of this thesis is the link between the fluid mechanics and the acoustics in the compressible starting jet. With an extensive analysis of both the fluid flow and the acoustics, we found two ways in which the trailing jet and the head vortex ring interact, producing two of the loudest noise sources of the compressible starting jet: (*i*) the ***shock–shear layer*** interaction is the basic noise generation mechanism of the broadband shock noise and (*ii*) the ***shock–shear layer–vortex ring*** interaction was found for the first time and generates a single acoustic wave, but with a higher amplitude than those from the broadband shock wave. Studying in detail the interface trailing jet – vortex ring we found that using a ***pinch-off vorticity threshold*** $\omega_{\mathrm{po}}/\omega_{\mathrm{vortex}} = 0.1$ is a more appropriate definition of the pinch-off (separation between the vortex ring and the trailing jet) than the previous methods used in the literature, based mainly on optical interpretations.

We have also confirmed that the evolution of the axial position of the vortex ring follows $x_{\mathrm{VR}}/D \sim (t^*)^{1/2}$ and the radius of the vortex ring evolves as $R_{\mathrm{VR}}/D \sim (t^*)^{1/3}$ during a significant period of time. Comparing a low subsonic vortex ring with a high subsonic and a supersonic one, we confirmed that compressibility reduces significantly the propagation velocity of the vortex ring. We analysed the effect of turbulence intensity at the inlet as well as three different nozzle geometries and we found that even with perturbations intensities 10% of the mean flow, the shock-cell structure still remains present.

With a broad knowledge of both fluid mechanics and the acoustics of the compressible starting jet as well as the link between both of them we

predicted some of the governing parameters from acoustic and/or optical measurements. This is particularly important for those disciplines where the direct access to the jet is not possible (such as volcanic jets) or for the development of new monitoring techniques.

Acknowledgement

Firstly, I would like to express my sincere gratitude to my advisor Prof. Jörn Sesterhenn for the support during my Ph.D. study and related research. I am very grateful for the possibility to use the equipment of the department and for giving me the tools to become a better researcher and a stronger person.

Besides my advisor, I would like to thank the rest of my thesis committee: Prof. Dr. Bogey and Prof. Julius Reiß, for accepting the invitation to become part of my thesis defense tribunal. Your comments helped to improve the quality of this thesis indeed.

My sincere thanks also goes to Thomas Engels, Mathias Lemke and Lewin Stein for many fruitful and funny discussions and for their continuous help. Without their precious support it would not be possible to conduct this research. I thank my friends and colleagues who supported me and motivated me towards my goal. I will always keep in mind the members of the "Computational Fluid Mechanics" Department that I met during these years: Stefano Alois, Sergio Bengoechea Lozano, Elias Büchner, Gabriele Camerlengo, Martin Franke, Marian Fuchs, Sonja Hoßbach, Sophie Knechtel, Steffen Nitsch, Lars Oergel, Mario Sroka, Christian Westphal, Wolfgang Wiese and Robert Wilke.

Also I thank my advisor during my internship in spring 2013 at the Hong Kong Polytechnical University, Assoc. Prof. Dr. Randolph Leung, for the support and the fertile conversations. Also my appreciation to my friends and colleagues during my asian internship: Garret Lam, Ka Him Seid, Harris Fan, Horus Chan and Ian Wong.

During the expeditions to the volcanoes and the different meetings about volcanoes I met many people who helped me to understand better how a volcano works, but also another completely different way of doing research. Thank you Ulli Küppers, Valeria Cigala, Jacopo Tadeucci, Pierre-Yves Tournigand, Tullio Ricci and Andrea Cannata.

Last but not the least, my special thanks goes to my parents Juan José and Ana and my brother Alberto for being the best family in the world, being always there and encouraging me during the difficult times, and my girlfriend Sabrina for showing me endless support and love; without you all this thesis would not have been possible. Thank you also, Martin, Birgit and Kathi for your welcoming arms.

Contents

Zusammenfassung V

Abstract VII

Acknowledgement IX

Nomenclature XXIII

1 Introduction 1

1.1 Description of the flow 5
1.2 Set-up description 9
1.3 Effects of the governing parameters 9
1.3.1 Reynolds number (Re_D) 10
1.3.2 Dimensionless mass supply (L/D) 12
1.3.3 Pressure ratio (p_{0r}/p_∞) 15
1.3.4 Temperature ratio (T_{0r}/T_∞) 17

I Simulations of a compressible starting jet 21

2 Numerical background 23

2.1 Navier-Stokes equations 23
2.2 Grid considerations 24
2.3 Parallelization 29
2.4 Initial conditions 30
2.5 Boundary conditions 31
2.6 Porous media / volume penalisation method 33
2.7 Sponge region 34
2.8 Simulations setup 35

II Experiments of a compressible starting jet 41

3 Experimental setup 43
- 3.1 Schlieren photography 45
- 3.2 Acoustic measurements in the laboratory 48
- 3.3 Acoustic measurements at real volcanoes 49
  - 3.3.1 Mount Etna 49
  - 3.3.2 Stromboli 50

III Results of jet simulations and experiments 53

4 Characterisation of the compressible starting jet 55
- 4.1 Compression wave 55
- 4.2 Vortex ring dynamics 55
  - 4.2.1 Vortex ring radius and core radius 56
  - 4.2.2 Axial location and propagation velocity 59
  - 4.2.3 Effects of compressibility 65
- 4.3 Trailing jet formation and dynamics 67

5 Effects of the inflow condition 71
- 5.1 Laminar inflow 71
- 5.2 Tripped boundary layer synthetic turbulence 72
- 5.3 Nozzle flow 72
- 5.4 Effects on the flow field 73
- 5.5 Effects on the radiated acoustics 76
- 5.6 Effect of the nozzle geometry on the starting jet 79

6 Pinch-off definition 83
- 6.1 Pinch-off vorticity threshold ($\omega_{\text{po}}/\omega_{\text{vortex}}$) 83
- 6.2 Circulation divergence law 85
- 6.3 Kelvin-Benjamin variational principle 91

7 Interaction between the vortex ring and the trailing jet 93
- 7.1 Shock–shear layer–vortex interaction 93
- 7.2 Shock–shear layer interaction 99
- 7.3 Effect of shock-waves dynamics on BBSN 100

8 Acoustics of the starting jet 103
- 8.1 Compression wave 104
- 8.2 Vortex ring 105
- 8.3 Turbulent mixing noise 106
- 8.4 Broadband shock noise 107

8.5 Screech 109
8.6 Directivity of the noise radiated 109
8.7 Frequency-time domain (wavelet) analysis 113

9 Governing parameters prediction from acoustic and optical measurements 123
9.1 Reynolds number 123
9.2 Pressure ratio 125
9.3 Dimensionless mass supply 128
9.4 Temperature ratio 128

10 Volcanic jets 131
10.1 Crater location from acoustic measurements 132
10.2 Frequency-time domain (wavelet and STFT) analysis 133

11 Conclusions and perspectives 137

Appendices 141

A Gas dynamics of nozzle flows 143

B Fully expanded conditions 149

C Quasi-steady reservoir motion 151
C.1 Subsonic nozzle 151
C.2 Choked nozzle 153
C.3 Effect of the main parameters 159

D Cylindrical reservoir analogy 165

E Instrumentation 169
E.1 Acoustic measurements 169
E.2 Schlieren components 170

Publications related to this work 170

Bibliography 175

List of Tables

2.1 Grid spacing considerations for the three-dimensional simulations 26
2.2 Grid spacing considerations for the two-dimensional simulations. 29
2.3 Parameter summary for cases involved in the trailing jet analysis. 33
2.4 Overview of the different set-ups for the analyses in this study. 36
2.5 Setup for the analysis of the vortex ring dynamics. 37
2.6 Setup for the analysis of the existence of the trailing jet. . . 37
2.7 Setup for the analysis of the trailing jet for an infinite reservoir. 37
2.8 Setup for the analysis of the inflow conditions. 38
2.9 Setup for the analysis of the geometry, non-dimensional mass supply and pressure ratio. 38
2.10 Setup for the analysis of the governing parameters. 39
2.11 Setup for the analysis of the Reynolds number. 39

4.1 Vortex ring non-dimensional radius at the end of the formation stage 57
4.2 Coefficients of the proportionality law. 60
4.3 Setup for the analysis of the vortex ring. 66

5.1 Nozzle design parameters for the cases $11.a - 13.h$. 80

6.1 Prediction of the pinch-off dimensionless time using the Kelvin-Benjamin variational principle. 91

A.1 Parameters of the nozzle geometry used for the example. . . 145

C.1 Parameters of the example in the subsonic nozzle flow. . . . 153
C.2 Parameters of the example in the supersonic nozzle flow. . . 155
C.3 Set of parameters chosen as base flow for this analysis. . . . 159

List of Figures

1.1 Stages of the starting jet. 5
1.2 Flow configuration showing the development of the Kelvin-Helmholtz vortices. 6
1.3 Contour plot of a laminar and a turbulent vortex ring. . . . 7
1.4 Three-dimensional kinetic energy spectra 8
1.5 Sketch of the system set-up. 9
1.6 Vorticity isosurface of jets with $Re_D = 5\ 000$ and $10\ 000$ in the continuous stage. 11
1.7 Isosurface of the Q-criterion of jets with $Re_D = 5\ 000$ and $15\ 000$ in the starting stage. 12
1.8 Starting jet fluid flow for different parameter set-ups to show different configurations where compressibility and turbulence play a main role. 13
1.9 Fluid flow of a compressible turbulent vortex ring without trailing jet. 14
1.10 Side effect of L/D on the jet Mach number. 15
1.11 Effect of pressure ratio on the temporal evolution of the jet Mach number for a divergent nozzle 16

2.1 Grid stretching and spacing. 25
2.2 Computational grid for the finest simulation. 26
2.3 Turbulent kinetic energy spectra for $Re_D = 5\ 000,\ 10\ 000$ and the highest resolution. 27
2.4 Turbulent kinetic energy spectra for $Re_D = 5\ 000,\ 10\ 000$ and different resolutions. 28
2.5 Strong and weak scaling plots. 30
2.6 Nozzle exit conditions. 32
2.7 Discretisation of the nozzle exit for different resolutions. . . 33
2.8 Sponge damping function. Linear and logarithmic representation. 35

3.1 General set-up in the anechoic chamber. 44
3.2 Sketch of a classical Z-type schlieren set-up. 45
3.3 General set-up for Schlieren photography. Detail view of the razor blade. 46
3.4 Detail view of the light source. Detail view of the razor blade at the camera. 47
3.5 Long exposure and high-speed Schlieren examples. 47
3.6 Disposition of the microphones in the acoustic measurements. 48
3.7 Active craters at Mount Etna. 49
3.8 Deployment of the microphones at Mount Etna. 50
3.9 General view of the craters at Mount Etna. Detail view of a laminar vortex ring ejected by Mount Etna. 50
3.10 Crater configuration at Stromboli on the 31$^{\text{th}}$ May 2016. . . 51
3.11 Microphones measuring the acoustic from Stromboli. 51

4.1 Characteristic diagram of the classical shock tube problem. Involved Mach numbers in the region after the compression wave for different reservoir to ambient pressure ratios. . . . 56
4.2 Geometrical parameters of the vortex ring 57
4.3 Evolution of the vortex ring non-dimensional radius. 58
4.4 R_{VR}/D-model trend lines and comparison with the literature. 59
4.5 Dynamics of the vortex ring core. 60
4.6 Evolution of the non-dimensional x-location of the vortex ring. 61
4.7 Evolution of the axial location of the vortex ring with the square root of the non-dimensional time. 62
4.8 Vortex ring propagation velocity over the non-dimensional time 63
4.9 Vortex ring propagation velocity for every case. 64
4.10 Evolution of the fully expanded Mach number and the circulation Mach number. 65
4.11 Evolution of the axial position, the radius and the core radius of the vortex ring. 66
4.12 Vorticity contour when the vortex ring is at $x/D \sim 11$ . . . 67
4.13 Characteristic diagram showing the dynamics of the shock waves. 69

5.1 Velocity perturbations imposed at the inflow for the TBL case. 72
5.2 Compressible Blasius inlet profile and sketch of the straight nozzle used in case 8 72
5.3 Instantaneous Mach number contours for the analysis of the inflow conditions. 74
5.4 Instantaneous entropy contours for the analysis of the inflow conditions. 75

5.5 Distribution of average Mach number and r.m.s. entropy perturbations along the jet axis 76
5.6 Sound pressure level spectra at 90° for the three inlet conditions in the analysis 77
5.7 Wavelet coefficient contour at 90°. 78
5.8 Sketch of the nozzles used in cases $11 - 13$. 80
5.9 Temporal evolution of the exit (left) and fully expanded (right) Mach number. 81

6.1 Sketch of the pinch-off vorticity threshold method. 84
6.2 Time evolution of the separation vorticity and the pinch-off vorticity threshold. 85
6.3 Sketch of the different methods used to compute the circulation. 86
6.4 Evolution of the circulation contained in the fluid flow for the starting jet. 87
6.5 Entrainment affects the circulation during the vortex ring growth 88
6.6 When entrainment disappears, the circulation recovers the normal behaviour. 89
6.7 3D effects to take into account when computing the circulation 89
6.8 Pinch-off prediction law. 90
6.9 Application of the Kelvin-Benjamin variational principle to predict the vortex ring pinch-off. 92

7.1 Stages of the shock cell structure during its interaction with the vortex ring. 94
7.2 Optical comparison of the fluid flow with the literature. . . 95
7.3 Acoustic radiated by the interaction and measured by the microphone at $r/D = 5$ 97
7.4 The noise produced by the interaction between the vortex ring and the trailing jet is at least as loud as the loudest noise source in the continuous jet in terms of sound pressure level. 98
7.5 The interaction wave propagates with the speed of sound. . 99
7.6 The acoustic waves radiated when a vortex passes by a shock wave (BBSN). 100
7.7 Characteristic diagrams showing the development of the first acoustic wave, vortex ring and shock waves for different inlet conditions. 102

8.1 Typical sound pressure level spectra for a continuous supersonic jet. 103

8.2 Pressure profile through the first wave for different inlet conditions in original and similarity axes. 104
8.3 Sound pressure level spectrum in a moving reference frame showing the directivity of the vortex ring noise. 105
8.4 Large scale turbulence noise waves visible in a schlieren picture of an under-expanded jet. 107
8.5 Noise generation mechanism of broadband shock noise. Numerical Schlieren contour with $M = 1$ iso-line. 108
8.6 Directivities of the different components of the jet noise. . . 110
8.7 Sound pressure level spectra radiated downstream and in the transverse direction. 111
8.8 Sound pressure level spectra of subsonic and supersonic jets. 112
8.9 Time series and sound pressure level spectrum of case 7.a. . 113
8.10 Wavelet coefficient contour of case 7.a. 114
8.11 Time series and sound pressure level spectrum of case 5. . . 115
8.12 Wavelet coefficient contour of case 5. 116
8.13 Time series and sound pressure level spectrum of case 4. . . 117
8.14 Wavelet coefficient contour of case 4. 118
8.15 Time series and sound pressure level spectrum of case 3. . . 119
8.16 Wavelet coefficient contour of case 3. 120
8.17 Time series and sound pressure level spectrum of case 1.a. . 121
8.18 Wavelet coefficient contour of case 1.a. 122

9.1 Variation with the Reynolds number of the peak Strouhal number for the fine-scale turbulent mixing noise. 124
9.2 Variation of the BBSN peak Helmholtz number with the pressure ratio. 127
9.3 Schlieren picture of an under-expanded jet to predict the fully expanded Mach number. 127

10.1 Crater location results of the eruptions measured during the mount Etna campaign in July 2014 134
10.2 Short time Fourier coefficient contour of the acoustics at Stromboli 135
10.3 Wavelet coefficient contour of the acoustics recorded at Stromboli. 136

A.1 Area - Mach number function for $\gamma = 1.4$. 144
A.2 Geometry, pressure ratio and Mach number along the Laval nozzle axis for the example case. 146

B.1 Fully expanded conditions in a jet. 150

C.1 Dimensionless pressure evolution in the reservoir. 153
C.2 Exit and fully expanded Mach number evolution in the subsonic nozzle. 154
C.3 Dimensionless pressure evolution in the reservoir for the supersonic nozzle flow. 155
C.4 Exit and fully expanded Mach number evolution in the choked nozzle. 156
C.5 PRANDTL-MEYER expansion angle evolution in the choked nozzle. 157
C.6 Evolution of the thermodynamic state in the reservoir during the discharge of the choked nozzle. 157
C.7 Fully expanded and exit density and temperature evolution of the choked nozzle. 158
C.8 Evolution of the shock-cell spacing and fully expanded diameter in the choked nozzle. 158
C.9 Evolution of the reservoir pressure and exit and fully expanded Mach number for the baseline case for the analysis of the main parameters. 160
C.10 Fully expanded Mach number contour plot over the pressure ratio and the non-dimensional time. 161
C.11 Fully expanded Mach number evolution with the non-dimensional time as a function of the non-dimensional mass supply. . . . 162
C.12 Fully expanded Mach number evolution with the non-dimensional time when changing the reservoir to ambient temperature ratio. 163
C.13 Fully expanded Mach number evolution with the normalised non-dimensional time $t^*/(T_r/T_\infty)$ when changing the reservoir to ambient temperature ratio. 164

E.1 Frequency response of the PCB microphone with the grid cap at 0 degrees incidence. 169
E.2 Frequency response of the G.R.A.S. microphone with the grid cap at 0 degrees incidence. 170

Nomenclature

Abbreviations

BBSN	Broadband shock noise
DSLR	Digital single-lens reflex
FSS	Fine scale similarity (spectrum), see Tam et al. [1996]
LSS	Large scale similarity (spectrum), see Tam et al. [1996]
LRZ	Leibniz-Rechenzentrum (Leibniz Supercomputing Centre)
MPI	Message Passing Interface
NPR	Nozzle pressure ratio. NPR $= p_{0r}/p_e$
r.m.s.	root mean square
STFT	Short Time Fourier Transform
SPL	Sound pressure level
TBL	Tripped boundary layer
TMN	Turbulent mixing noise

Greek Symbols

θ	As suggested by Tam [1995], the jet angle from the upstream direction
σ	Damping function of the sponge region to treat numerically the outflow condition
ρ	Density (kg/m^3)
μ	Dynamic viscosity. For air at normal conditions $\mu = 1.7 \times 10^{-5}$ kg/(m s)

λ	Heat conductivity (m^2/s)
γ	Isentropic exponent: $\gamma = C_p/C_v$
ν	Kinematic viscosity (m^2/s)
η	Kolmogorov length scale. $\eta = \left(\nu^3/\varepsilon\right)^{1/4}$
ω_{vortex}	Maximum vorticity in the vortex ring
K	Permeability of a porous medium (m^2)
ω_{po}	Pinch-off vorticity threshold
ϕ	Porosity of a porous medium $\phi = V_f/V$
τ_{ij}	Shear stress tensor
ε	Turbulent kinetic energy dissipation rate. $\varepsilon = \nu\langle \frac{\partial u_i'}{\partial x_j}\frac{\partial u_i'}{\partial x_j}\rangle$
δ	Vortex ring core radius
ω	Vorticity vector $\omega = \nabla \times u$

Mathematical operators

$\langle\,\cdot\,\rangle_\theta$	Average in the azimuthal direction
$\widehat{(\,\cdot\,)}$	Variable in Fourier Space

Roman Symbols

x_{VR}	Axial position of the vortex ring
U	Characteristic velocity
A^*	Critical nozzle cross section area
R	Gas constant. For air at normal conditions $R = 287.058$ J $\mathrm{kg}^{-1}\mathrm{K}^{-1}$
d_{grid}	Grid characteristic length. $d_{\text{grid}} = \left(dx_{\min} + dy_{\min} + dz_{\min}\right)/3$ for the three-dimensional case and $d_{\text{grid}} = \left(dx_{\min} + dy_{\min}\right)/2$ for the two dimensional case.
H	Helmholtz number $H = fD/c_\infty$
V_0	Injected fluid volume
Kn	Knudsen number

L	Length of the hypothetical cylindrical reservoir with diameter D that contains the same mass as the real reservoir
M_Γ	Mach number based on the vortex ring circulation
m	Mass contained in the reservoir
$(p_r/p_\infty)_{\mathrm{blast}}$	Necessary pressure ratio to generate a blast wave. See Ishii et al. [1999]
t^*	Non-dimensional time $t^* = t/(D/u_j)$
A	Nozzle cross section area
D	Nozzle diameter
Pr	Prandtl number
R_{VR}	Radial position of the vortex ring
Re	Reynolds number
L_s	Shock cell length
c	Speed of sound (m/s)
St	Strouhal number $St = fD/u_j$
S_{ij}	Symmetric part of the shear stress tensor. $S_{ij} = \frac{1}{2}\left(\frac{\partial u_i}{\partial x_j} + \frac{\partial u_j}{\partial x_i}\right)$
T	Temperature (K)
u	Velocity (m/s)
$(L/D)_{\mathrm{lim}}$	*Formation number*, the limiting value that defines the existence of a trailing jet, see Gharib et al. [1998]

Subscripts

$(\,\cdot\,)_j$	Fully expanded conditions. See appendix B
$(\,\cdot\,)_e$	Nozzle exit conditions
$(\,\cdot\,)_r$	Reservoir conditions
$(\,\cdot\,)_\infty$	Unbounded chamber conditions

Chapter 1

Introduction

Continuously blowing jets have been reported in an extensive literature both in the incompressible (e.g. [Ryhming, 1973]) and in the compressible case (e.g. [Tam, 1995]). This work focuses on the starting phase of a compressible jet, this is, the formation of the jet flow from a quiescent condition if the jet is ejected from an infinite reservoir or the generation of a vortex ring with no jet at all in the extreme case of a very small reservoir compared to the nozzle diameter. A full range of starting and decaying jets can be generated for different values of the governing parameters between these two extremes.

The starting jet has been already reported in the literature: the incompressible case has initiated a considerable literature, mainly playing a secondary role in the study of vortex ring dynamics, which are typically generated by a piston-driven device in incompressible flows; the compressible case has been recently presented in [**J.J. Peña Fernández** and Sesterhenn, 2017a]. In this work, we examine the compressible starting and decaying jet in detail and discuss the effects of the governing parameters in the jet flow and the radiated acoustics.

Turner [1962] developed the first model of the starting jet composed by a spherical vortex followed by a steady jet experimenting with a buoyant plume and found that the tip of the spherical vortex moves slightly faster than half of the maximum velocity in the jet at the same location for a later time. In a similar manner, reporting for incompressible flows experimentally, Witze [1980, 1983] proposed a theoretical model that assumes the transient jet as a spherical vortex interacting with a steady jet and demonstrated that the ratio of the nozzle diameter (D) to the characteristic jet velocity (U) defines a time constant $\tau = D/U$ that uniquely characterises the behaviour of impulsively started jets leading to the dimensionless time $t^* = t/(D/U)$. Recently, Gao and Yu [2015] reviewed the basic ideas on the incompressible starting jet and stated that the two broad directions of the current research are (*i*) the vortex ring pinch-off and (*ii*) entrainment enhancement in pulsed-jet propulsion systems.

Starting jets have been typically used in most of the experimental work to produce vortex rings, being only the latter the focus of the research. Based on experimental observations, Maxworthy [1972] described the flow field, the vortex ring's velocity and the growth rate for stable rings. The reviews of Shariff and Leonard [1992] and Lim and Nickels [1995] provide a detailed background of vortex ring properties and their dynamics. In the literature, most of the experimental studies generate the vortex rings by ejecting an incompressible fluid moving a piston inside a cylindrical tube of diameter D for a length L into an open chamber, giving rise to the definition of the parameter (L/D). However, L/D can be regarded with a more general view through the continuity equation as the non-dimensional mass supply: the mass contained in a cylinder of diameter D and length L ($m_{\mathrm{cyl,L}}$), compared to the one contained in a cylinder with $L = D$ ($m_{\mathrm{cyl,L=D}}$):

$$\frac{m_{\mathrm{cyl,L}}}{m_{\mathrm{cyl,L=D}}} = \frac{\pi(\frac{D}{2})^2 L\rho}{\pi(\frac{D}{2})^2 D\rho} = \frac{L}{D}, \tag{1.1}$$

which is more convenient in compressible flows, because it is the available budget to generate the flow and it directly relates to the basic equation (continuity), rather than relating to geometrical factors.

Concerning the vortex ring dynamics, Didden [1979] proposed that the axial and radial positions of the vortex ring (x_{VR} and r_{VR}, respectively) vary in the very early stage of the process ($0.1 < t^* < 1$) as $x_{\mathrm{VR}}/D \sim (t^*)^{3/2}$ and $R_{\mathrm{VR}}/D \sim (t^*)^{2/3}$. In a later stage, for $t^* > 1$, the variation of the axial and radial positions of the vortex ring were found to be $x_{\mathrm{VR}}/D \sim (t^*)^{1/2}$ Witze [1980] and $R_{\mathrm{VR}}/D \sim (t^*)^{1/3}$ Kelvin [1867], respectively. We present in chapter 4 the characterisation of the compressible starting jet. Gharib et al. [1998] found a limiting value for the non-dimensional mass supply $(L/D)_{\mathrm{lim}}$ of approximately four that universally defines the existence of a trailing jet after the vortex ring. This limiting value was called 'formation number'. These results were reproduced by Rosenfeld et al. [1998] and many others but it was reported that this limiting value is not universal and it may vary within the range $1 < (L/D)_{\mathrm{lim}} < 5$ depending on the spatial and temporal distribution of the inlet condition or the Reynolds number, like Zhao et al. [2000], Gao and Yu [2010] or Rosenfeld et al. [1998]. This problem is discussed for the compressible starting jet in section 4.3. Hermanson et al. [2000] defined the limiting parameter as $(L/D)_{\mathrm{lim}}^{1/3}$ in order to relate it to the characteristic length of a cylinder defined by the authors as the cubic root of the injected volume ($V_0^{1/3}$), resulting $(L/D)_{\mathrm{lim}}^{1/3} \sim V_0^{1/3}/D$.

The numerical studies related to this work have been typically focused on the vortex ring, because of the relatively low requirements of computational resources. The most closely related numerical studies in the literature are presented here.

James and Madnia [1996] found that during the formation of the vortex ring, the momentum and the total circulation are approximately the same generating the vortex ring through an orifice in a wall or through a nozzle, where no wall is around the lip of the nozzle. We address the effect of the inflow conditions in chapter 5.

Investigating the trailing jet instabilities numerically, Zhao et al. [2000] found that the Kelvin-Helmholtz instabilities from the shear layer drive the *pinch-off* process, defined as the physical separation of the vortex ring from the trailing jet. Several attempts have been made to model the pinch-off of the incompressible starting jet in the last decade (e.g. [Gao and Yu, 2010]). An appropriate definition of the pinch-off process and a discussion of the pinch-off in the compressible starting jet are given in chapter 6. Shortly before the pinch-off takes place, the vortex ring interacts with the trailing jet in the compressible case, leading to one of the loudest noise sources of the compressible starting jet. This interaction is examined in chapter 7.

Zaitsev et al. [2001] compared the noise measurements of a turbulent vortex ring with theory and confirmed that the turbulent vortex ring noise can be represented as the sum of three quadrupoles. Ran and Colonius [2009] proposed three stages for the sound generation of a turbulent vortex ring: the instability waves which generate relatively weak sound, the vortex breakdown (connected with the maximum sound pressure level) and the turbulent decay, which leads to a decay in the sound pressure level of 30dB.

There exists a very extensive literature of the jet flow. Interested readers are directed to the review by Ball et al. [2012], which provides a very clear and detailed overview of the different contributions. We give here a brief overview of the milestones in the jet flow research.

Tollmien [1926], one of the first works in turbulent jets, considered an incompressible jet flow through Prandtl's mixing length theory. The first experimental studies of a round jet were carried out by Ruden [1933] and Kuethe [1935], who reported the similarity of velocity profiles was reached before $10D$. The jet similarity and the region in which this takes place is still under debate. The first direct numerical simulation of a supersonic jet was reported by Freund et al. [2000], who considered a jet with a Reynolds number $Re_D = 2000$ based on the nozzle diameter and on the fully expanded Mach number $M_j = 1.92$ at adapted conditions, focusing mainly on the confirmation of the direct numerical simulation and the acoustic radiated by the supersonic jet. As shown, the main focus until now has been to characterise the fluid flow through statistical analyses to obtain universal laws that define the behaviour of the jet flow.

The noise generated by the jet flow has been intensively studied since the decade of 1950, starting with Powell [1953], who considered the noise radiated by a choked nozzle flow. The jet noise, especially from supersonic continuous jets, is a very useful reference for the acoustics of the compressible starting jet, which can be considered a new topic. A short overview of the closest jet noise references is presented here focusing on supersonic jets.

The reviews of Seiner and Yu [1984] and Tam [1995] focus on the supersonic jet noise, providing a detailed discussion about the three different noise components and their generation. The *turbulent mixing noise* is produced by the turbulent scales of the shear layer and therefore it is radiated in both subsonic and supersonic cases. The *broadband shock noise* is generated by the interaction between the shock waves and the vortices of the shear layer where the shock waves are reflected. The *screech tones* are generated by a feedback loop in which the acoustic waves travel backwards (in the subsonic surroundings of the jet) to the lip of the nozzle triggering new disturbances that are again convected downstream until the point in which these acoustic waves were generated, where the shear layer vortices interact with the shock waves, closing in this way the loop with a specific frequency. The acoustics of the starting jet are presented in chapter 8.

As typical in jet noise, the angle θ that characterises the directivity is measured from the jet axis in the upstream direction, Tam [1995]. We use here the same convention.

As proposed by Tam et al. [1996], the TMN can be described by two similarity spectra produced by two noise sources: (*i*) the *large-scale similarity* (LSS) spectrum produced by the large and coherent structures and (*ii*) the *fine-scale similarity* (FSS) spectrum produced by the fine turbulent scales. Some time later, Tam et al. [2008] confirmed that only two different sources of jet TMN exist: the fine-scale turbulence and the large turbulent structures of the jet flow. Comparing the noise of a perfectly expanded with an under-expanded jet from a convergent-divergent nozzle, Kim et al. [1994] provided evidence that the presence of a shock cell structure does not modify the TMN.

Linking the governing parameter of the compressible starting jet (section 1.3) to the acoustics generated (chapter 8) we can predict the governing parameters from acoustic measurements. We handle this problem in chapter 9. This is especially useful when no direct access to the jet flow is possible, as in volcanic flows. This is expected to be relevant for volcanic monitoring purposes. We included as well in this work a chapter dedicated to volcanic jets, chapter 10.

1.1 Description of the flow

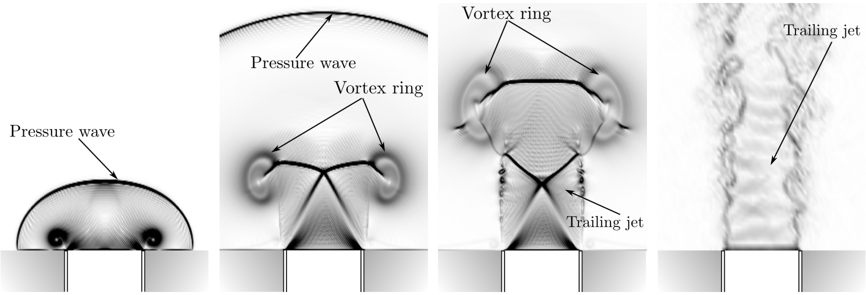

(*a*) Pressure wave (*b*) Vortex ring (*c*) Trailing jet (*d*) Decay stage

Figure 1.1: Stages of the starting jet. Numerical schlieren ($|\nabla\rho|$) is shown. The case 7.*c* is represented in (*a*) for $t^* = 0.8$, (*b*) $t^* = 3.2$ and (*c*) $t^* = 5.9$ and case 6 is represented in (*d*) for $t^* = 72$.

During the impulsive discharge of the reservoir, just after the release of the pressure through the nozzle, a compression wave is formed in the vicinity of the nozzle exit. This compression wave is generated by the impulsive start of the jet. The compression wave has a half-spherical form and travels into the unbounded chamber with the speed of sound if it is a pressure wave, as in figure 1.1*a*, or faster if it is a blast wave. The basic idea of a blast wave is a violent propagating disturbance, produced historically by an explosion, that consist of an abrupt rise in pressure followed by a drop to or below atmospheric pressure. The interested reader is directed to Taylor [1950] for more information.

During the propagation of the compression wave in the first few diameters, a vortex ring is always generated due to the large velocity gradients, figure 1.1*b*. The vortex ring grows until a critical size is reached ($1.08D$ proposed by Didden [1979]) and then it starts propagating in the axial direction. Shortly after the beginning of the vortex ring propagation, the vortex ring separates from the trailing jet (if existing) and propagates further, detached from the rest of the flow. The pinch-off process is driven by the Kelvin-Helmholtz instabilities from the shear layer in the trailing jet, Zhao et al. [2000]. When the successive Kelvin-Helmholtz vortices in the shear layer are generated, they start rotating and drawing in vorticity from upstream and downstream of the vortex in the shear layer and this leads to a vorticity distribution along the shear layer with concentrated regions of large vorticity (the vortices) separated by regions of relatively low vorticity (the spaces between two consecutive vortices). These spaces between vortices are the potential locations where the pinch-off would take place, see figure 1.2. The first Kelvin-Helmholtz vortex after the vortex ring is the first which is generated and therefore the one which will create the first a region of very low vorticity around it (if it is not ingested by the head vortex ring), leading to the pinch-off when the low vorticity reaches the pinch-off criterion. The dynamics of the shear layer vortices play a crucial role in the pinch-off process. A detailed analysis of the pinch-off definition is presented in section 6.1. In order to predict the pinch-off, a relationship between the normalised circulation injected until the pinch-off and the non-dimensional time is provided in section 6.2.

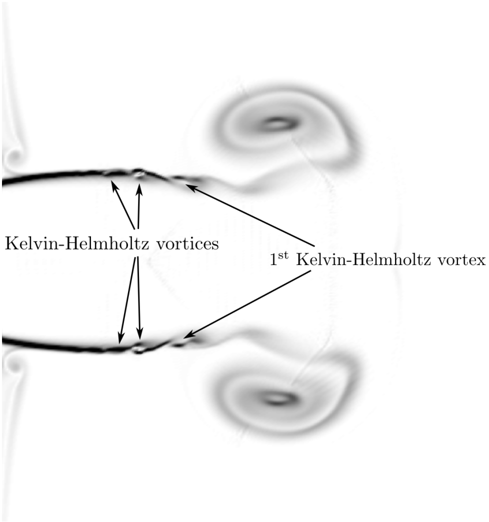

Figure 1.2: Flow configuration for $t^* = 5.5$ showing the development of the Kelvin-Helmholtz vortices in the case 7.*c*. The vorticity magnitude is shown in a black and white colour-scale.

Figure 1.3 shows a snapshot of the Mach number flow field of a laminar and a turbulent vortex ring. A very well organised flow with one main big structure describes the laminar case in figure 1.3*a*. As opposed to that, the turbulent vortex ring in figure 1.3*b* includes a wide range of scales with different sizes, but still with the global structure of a vortex ring. To verify that the instabilities present in the turbulent vortex ring are true turbulence we show in figure 1.4 the three-dimensional energy spectra calculated using the velocity fluctuations with respect to the azimuthal average: $u' = u - \langle u_\theta \rangle$, where u is the instantaneous velocity and $\langle u_\theta \rangle$ is the mean velocity averaged in the azimuthal direction. The Kolmogorov length scale was calculated as $\eta = \left(\nu^3/\varepsilon\right)^{1/4}$, where $\varepsilon = \nu \langle \frac{\partial u_i'}{\partial x_j} \frac{\partial u_i'}{\partial x_j} \rangle$ and ν is the kinematic viscosity. The same procedure was performed for both cases.

For the laminar case, we used the Kolmogorov length scale of the turbulent case because we focus on the shape of the curves rather than their position in the diagram. The dashed line corresponds to the laminar case, showing one big structure with the most of the energy and a rapid decay for small scales. The solid line, corresponding to the turbulent case, shows a big structure with a lot of energy, but for smaller scales, we can see a decay of the energy very close to the $-5/3$ exponent of the Kolmogorov law. This confirms that inside the vortex ring a wide range of scales with different sizes dissipate the kinetic energy in the turbulent way: this is a turbulent vortex ring.

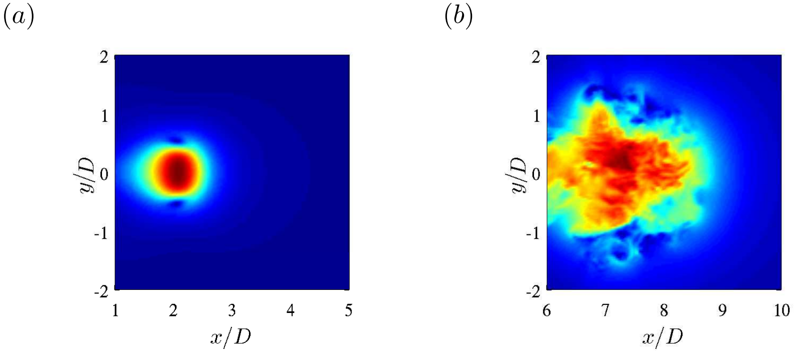

Figure 1.3: Mach number magnitude contour plot of (a) a laminar (M in the range $[0, 0.16]$) corresponding to case 1.a and (b) a turbulent vortex ring (M in the range $[0, 1.85]$) corresponding to case 7.a.

In the case of the existence of a trailing jet, the jet interacts with the vortex ring already for a Reynolds number of 5 000. This interaction, here called *shock-shear layer-vortex ring interaction*, is explained in detail in section 7, leading to one of the loudest noise sources of the starting jet and comparable to those of the continuous jet.

The trailing jet can be either subsonic during the whole process or supersonic during the impulsive period and subsonic during the final decay, (see figure 1.1d), but it cannot be subsonic during the first stage, followed by a supersonic stage and a final subsonic decay because we focus on the impulsively starting jet: the acceleration time interval to have supersonic flow at the nozzle exit should be shorter than the time in which the vortex ring is completely generated, so in the onset of the trailing jet there are already supersonic conditions. Since the pressure at the inlet changes continuously with time, the jet will be adapted for a specific time (when the pressure ratio is the one the nozzle was designed for), being imperfectly expanded for the rest, which means that the supersonic associated phenomena such as shock waves and expansion fans will be present for most of the supersonic stage.

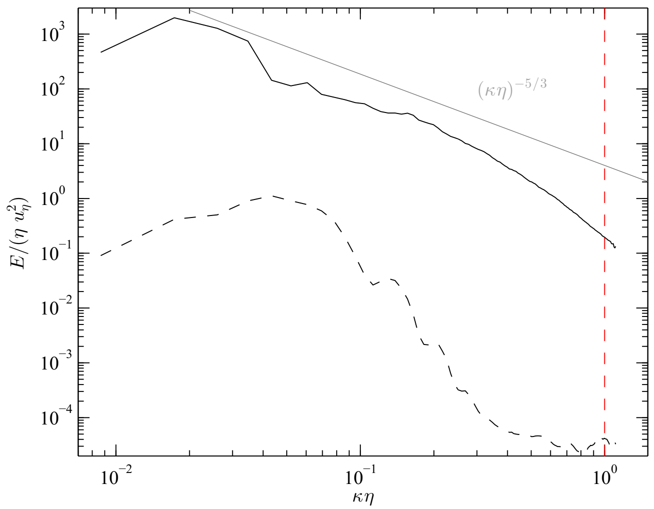

Figure 1.4: Three-dimensional kinetic energy spectra. $Re_D = 5000$. The solid black line corresponds to a turbulent vortex ring. Case 7.*a*. The dashed black line corresponds to a laminar vortex ring. Case 1.*a*. The vertical red dashed line indicates the Kolmogorov scale and the grey solid line the $-5/3$ reference decay.

The combination of shock waves and expansion waves is usually called in the literature 'shock cell structure', and its properties depend mainly on the working fluid via the isentropic exponent γ, the geometry of the nozzle, via the exit to critical area ratio A_e/A^* and the operation conditions via the reservoir to ambient pressure ratio p_{0r}/p_∞. The relationship between the operating conditions and the geometrical properties of the shock cell structure of the trailing jet can be used to characterise the jet flow using the correlations of the literature when the governing parameters are unknown.

Also due to the evolution of the inlet condition during the decay phase, the shock waves present in the trailing jet translate with a specific velocity, which can be comparable to the speed of sound, especially during the decay stage, having a strong effect on the acoustic radiated. More details about this phenomenon are given in section 7.3.

The noise radiation directionality of the continuous jet is very well known in the community. In section 8.6 we study the angular dependence of the sound pressure level for the starting jet and compare it with the continuous one.

The physical process finishes when the reservoir reaches the pressure of the unbounded chamber, assuming that the effects of buoyancy or mass diffusion due to temperature differences between the reservoir and the unbounded chamber can be neglected.

1.2 Set-up description

The basic configuration considered here for a compressible starting jet is a pressurised reservoir separated from an unbounded chamber by a convergent nozzle ($A_e/A^* = 1$, where A_e is the nozzle exit cross section area and A^* is the critical cross section area) through which the fluid is discharged, see figure 1.5. The conditions in the reservoir are denoted with a subscript 'r' (p_r) and the total conditions at the reservoir are indicated with a subscript '0r' (p_{0r}), while the conditions in the unbounded chamber are denoted with a subscript '∞' (p_∞).

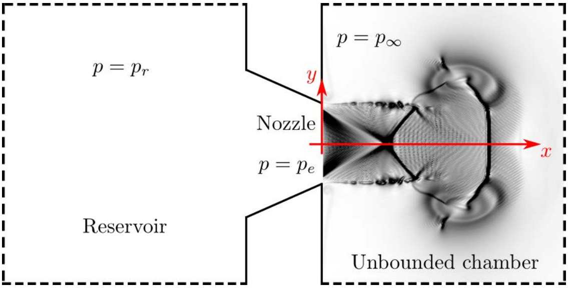

Figure 1.5: System set-up. The reservoir (left) is pressurised initially at p_{0r} and the fluid is injected through a convergent nozzle into the unbounded chamber (right), at a pressure p_∞. The pressure at the centre of the nozzle exit is p_e.

We restrict our analysis to the neutral temperature case, this is, $T_{0r} = T_\infty$, where T_∞ is the temperature in the unbounded chamber. The inlet is chosen to be adiabatic and therefore an isentropic flow takes place from the reservoir up to the lip of the nozzle.

1.3 Effects of the governing parameters

The behaviour of the starting jet is governed by four main dimensionless parameters: the **Reynolds number** (Re_D), affecting mainly the size of the Kelvin-Helmholtz instabilities relative to the nozzle diameter and therefore the turbulence; the **non-dimensional mass supply** (L/D) given by the length (L) of a hypothetical cylindrical reservoir with a constant diameter (D) (the same diameter as the nozzle) and the same volume than the real reservoir, influencing mainly the existence of the trailing jet, the **reservoir**

to unbounded chamber pressure ratio (p_{0r}/p_{∞}), having an effect on the compressibility and the **reservoir to unbounded chamber temperature ratio** T_{0r}/T_{∞}.

In this section, we address the questions of what changes take place in the compression wave, vortex ring or trailing jet when changing the governing parameters and what are the limiting values of the governing parameters that define a specific behaviour.

1.3.1 Reynolds number (Re_D)

The main effect of the Reynolds number in the starting jet is the size of the Kelvin-Helmholtz instabilities in the shear layer of the trailing jet compared to the nozzle diameter assuming a constant shear layer thickness of $0.1D$. A larger Reynolds number leads to a smaller size of instabilities, and vice-versa. This has several consequences.

We observed that a smaller size of the Kelvin-Helmholtz instabilities leads to an earlier pinch-off. The smaller vortices are earlier formed in the jet and they start earlier to absorb vorticity upstream and downstream of the vortex which leads to a situation in which the vorticity threshold defined for the pinch-off is reached earlier. Therefore, there is a critical Reynolds number ($Re_{D,\text{interaction}}$) that makes the first Kelvin-Helmholtz vortex to be already formed when it passes through the first shock wave, see figures 1.1*c* and 1.2. The *shock-shear layer-vortex* interaction takes place only if the Reynolds number is larger than this critical value. The Reynolds numbers in this study ($Re_D = 5\ 000$ and $10\ 000$) exceed this critical value, but the Reynolds number in Zhao et al. [2000], ($Re_D = 3\ 800$) is clearly under the critical one. The critical Reynolds number $Re_{D,\text{interaction}}$ for the *shock-shear layer-vortex* interaction is an open question and future work should answer this question. For more details see section 7.

Ricou and Spalding [1961] suggested that the entrainment coefficient does not vary in turbulent jets for Reynolds number larger than 10 000 and this value might be the starting of the Reynolds independence regime for turbulent jets. Based on the relative magnitude of dimensional spatial scales, Dimotakis [2000] reported that the fully-developed turbulent flow requires an outer-scale Reynolds number of $Re_D \gtrsim 10\ 000 - 20\ 000$. With these arguments, and with the limitations of computational capacity, we chose a Reynolds number of 10 000 for the starting jet without decay (case 7.*c* in table 2.7) as the largest practical Reynolds number to be fully resolved. A Reynolds number of 15 000 was simulated (case 7.*d* in table 2.7) with the same resolution as chosen for $Re_D = 10\ 000$ to explore the limits of the spatial resolution. As a direct comparison we show in figure 1.6 the vorticity isosurface of two jets with $Re_D = 5\ 000$ and $10\ 000$ in the continuous stage, where it can be seen, that the smallest turbulent scales in the case with $Re_D = 10\ 000$ are smaller than the ones for $Re_D = 5\ 000$,

(*a*)

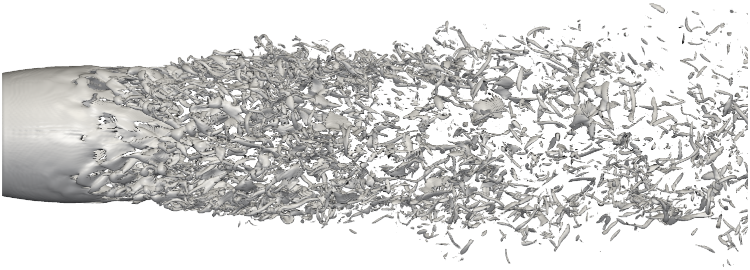

(*b*)

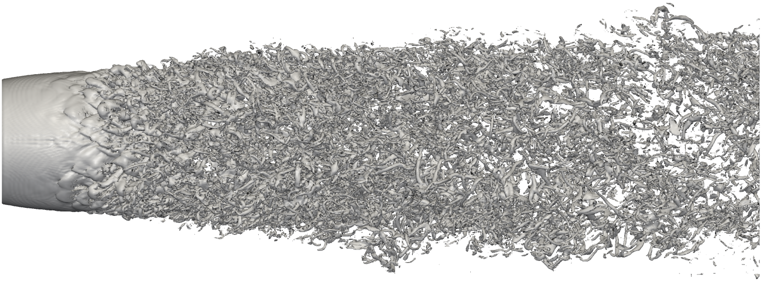

Figure 1.6: Vorticity isosurface. (*a*) $Re_D = 5\ 000$, $\omega/\omega_{\max} = 0.1$. Case 7.*b* (*b*) $Re_D = 10\ 000$, $\omega/\omega_{\max} = 0.1$. Case 7.*c*.

while the largest turbulent scales remain the same size. In figure 1.7 we show a comparison between two jets in their starting stage at $Re_D = 5\ 000$ and 15 000, with the same conclusion, but where the inner structure of the vortex ring can be seen.

Examining the needed conditions to generate an incompressible laminar vortex ring, a laminar vortex ring that transitions to turbulence and an initially turbulent vortex ring, Glezer [1988] generated a map, specifying that for Reynolds numbers (defined as Γ/ν) larger than 2.5×10^4 an initially turbulent vortex ring was generated. For laminar-generated vortex rings, an azimuthal instability (similar in appearance to the Kelvin-Helmholtz instability of a free shear layer) amplifies and makes the vortex ring to breakdown to turbulence. They also reported that for larger velocities at the nozzle exit, the axial distance to the turbulent transition of the vortex ring was shorter. This interaction is hereafter called *shear layer-vortex* interaction. We observed that compressibility accelerates the onset of this interaction. This interaction is examined in detail in chapter 7.

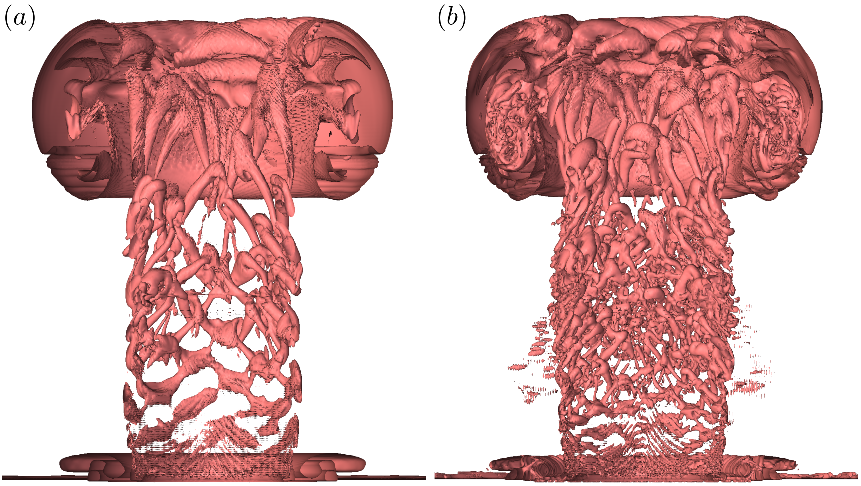

Figure 1.7: Isosurface Q-criterion. (a) $Re_D = 5\ 000$, $Q = 10^9$. Case 7.b (b) $Re_D = 15\ 000$, $Q = 10^9$. Case 7.d.

1.3.2 Dimensionless mass supply (L/D)

Often can be seen L/D as the 'stroke ratio' in experimental works of the literature when dealing with an incompressible starting jet. Typically the starting jet of an incompressible fluid was driven by a piston in a cylinder of diameter D over a stroke of length L, giving rise to the definition of L/D as one of the governing parameters. In compressible flows, we showed already in the introduction (equation 1.1) how L/D can be seen in a more general way as the non-dimensional mass supply. The main effect of the dimensionless mass supply is on the existence of the trailing jet.

The limiting value of the non-dimensional mass supply $(L/D)_{\text{lim}}$ dictates the existence of a trailing jet after the vortex ring in the starting jet. The more mass is injected by the nozzle, the more vorticity is provided to the vortex ring. If the vortex ring takes all the vorticity ejected by the nozzle we call it *not saturated*, because it could take some more vorticity. If the vortex ring does not take all the vorticity ejected by the nozzle, a trailing jet is generated with the rest of the vorticity that the vortex ring is not able to take. In this case, the vortex ring is *saturated*. A limit has been already been set for the value of L/D to saturate the vortex ring Gharib et al. [1998], $(L/D)_{\text{lim}} \simeq 3.6 - 4.5$, but it has been stated that this limit is not universal and it depends on the temporal and spatial inlet condition distributions, as well as the Reynolds number, Zhao et al. [2000]; Rosenfeld et al. [1998]; Gao and Yu [2010]. More details are given in 6.2. The limiting value $(L/D)_{\text{lim}}$ for compressible flows is an open question that should be addressed by future work, but from observations in this study the value appears to be very close to the incompressible one.

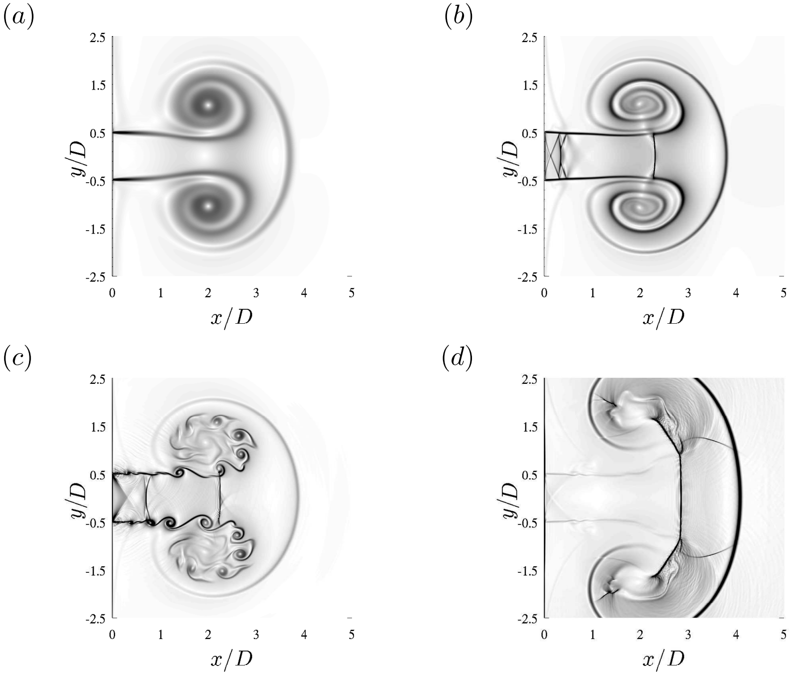

Figure 1.8: Starting jet fluid flow with different sets of parameters of several two-dimensional simulations to exemplify the differences not only between the incompressible and the compressible cases, but also among the compressible cases for different regimes. (*a*) Incompressible, case 15. $t^* = 6.41$. $M_j = 0.1$. $|\nabla\rho| \in [0, 0.025]$. (*b*) Supersonic laminar, case 20. $t^* = 13.37$. $M_j = 1.27$. $|\nabla\rho| \in [0, 2]$. (*c*) Supersonic turbulent, case 18. $t^* = 12.72$. $M_j = 1.32$. $|\nabla\rho| \in [0, 3]$. (*d*) Supersonic with blast wave, case 22. $t^* = 6.91$. $M_j = 1.70$. $|\nabla\rho| \in [0, 4]$. The axial position of the vortex ring is $x_{VR}/D = 2$ for all cases.

The stability of the shear layer might also be influenced by this parameter. On the one hand, the jet in figure 1.8*c* shows an unstable shear layer. This jet comes from an infinite reservoir ($L/D \to \infty$), blowing continuously and the combination of the governing parameters lead to an unstable shear layer and a turbulent jet. On the other hand, the jet in figure 1.8*b* shows a stable shear layer. This jet comes from a finite reservoir ($L/D = 8$) and is already in the decay stage, so it does not blow with the maximum velocity and the shock waves are travelling towards the nozzle exit. However, the leading vortex ring is propagated in the axial direction. This leads to a stable shear layer and a laminar jet.

Figures 1.8*a* and *d* are included to show how similar are the effects of the pressure ratio, Reynolds number and dimensionless mass supply. Comparing optically the figures 1.8*a* and *c*, we would expect a change in the Reynolds number between both cases, although the only different parameter is the pressure ratio $p_{0r}/p_\infty = 1.007$ in *a* and $p_{0r}/p_\infty = 2.84$ in figure 1.8*c*; the rest of the parameters have the same value: $L/D \to \infty$, $Re_D = 5000$ and $T_{0r}/T_\infty = 1$. While figure 1.8*a* shows a laminar and incompressible starting jet, figure 1.8*c* shows a supersonic and turbulent starting jet.

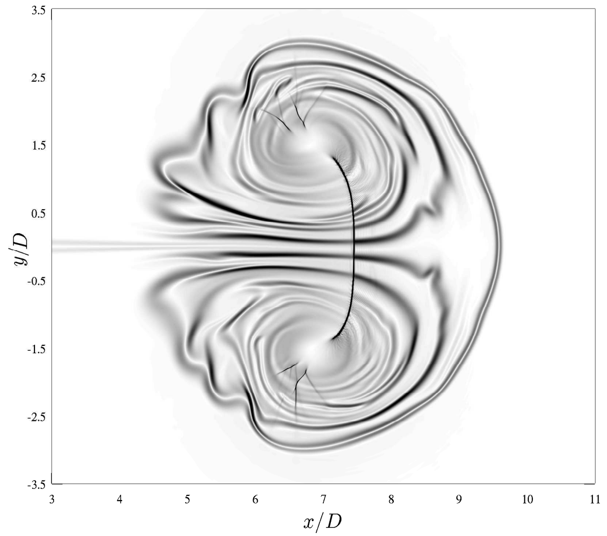

Figure 1.9: Numerical schlieren for the case $p_{0r}/p_\infty = 50$, $L/D = 0.1659$, $Re = 5000$. $|\nabla\rho| \in [0, 4]$. $t^* = 38.0378$. $M_j = 1.6979$. A very weak trailing jet is present although the jet was generated with a very large pressure ratio, due to the low value of the non-dimensional mass supply ($L/D = 0.1659$).

Figure 1.8*d* shows a starting jet generated with a pressure ratio of $p_{0r}/p_\infty = 50$, a Reynolds number of $Re_D = 5\ 000$ (same as the other subfigures) and with a relatively small non-dimensional mass supply ($L/D = 0.1345$). Comparing this set of parameters with those of figure 1.8*b*, we agree on expecting a larger Mach number, because of a stronger expansion, but due to the small value of L/D, one could expect a fully laminar vortex ring, but we can identify the turbulent character of the vortex ring. Figure 1.9 shows, for a later stage, the turbulent and compressible vortex ring generated in the same case as figure 1.8*d*.

The starting jet with a finite L/D will not reach the same maximum fully expanded Mach number expected for the continuous jet ($L/D \rightarrow \infty$) at the same pressure ratio (p_{0r}/p_∞). The maximum fully expanded Mach number decreases with lower L/D values. After the release of the pressure, the expansion wave that travels inside the nozzle is reflected at the bottom of the reservoir for an earlier time, so the expansion takes place during a shorter period.

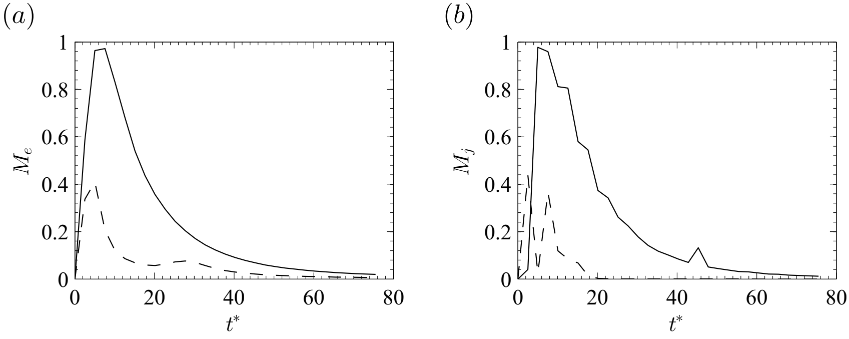

Figure 1.10: Effect of the non-dimensional mass supply on the temporal evolution of the exit (*a*) and fully expanded (*b*) Mach number. Straight nozzle ($A_e/A^* = 1$), $p_{0r}/p_\infty = 4$. Dashed: $L/D = 2$ (case 11.*c*), solid: $L/D = 8$ (case 11.*d*).

Figure 1.10 represents the effect of the non-dimensional mass supply L/D in the exit and fully expanded Mach number. With a straight nozzle ($A_e/A^* = 1$) and a pressure ratio of $p_{0r}/p_\infty = 4$ we see how a bigger reservoir (solid line, $L/D = 8$) leads to a faster flow during a longer time than the case with a smaller reservoir (dashed line, $L/D = 2$).

1.3.3 Pressure ratio (p_{0r}/p_∞)

The steady fully expanded Mach number (M_j) of a continuous jet can be determined just by p_{0r}/p_∞, assuming $\gamma = 1.4$ for diatomic gases, by using the one-dimensional isentropic theory, see equation (1.2). The larger is p_{0r}/p_∞ the stronger is the expansion through the nozzle and the larger is the fully expanded Mach number. In the compressible starting jet, p_{0r}/p_∞ plays a crucial role determining the existence of shock waves, expansion fans and their geometrical distribution. This parameter does not appear in the incompressible case.

$$M_j = \sqrt{\frac{2}{\gamma - 1}\left(\left(\frac{p_{0r}}{p_\infty}\right)^{\frac{\gamma-1}{\gamma}} - 1\right)} \tag{1.2}$$

The minimum reservoir to unbounded chamber pressure ratio needed to chock a one-dimensional isentropic convergent nozzle is given by $\left(\frac{p_{0r}}{p_\infty}\right)^* = \left(\frac{\gamma+1}{2}\right)^{\frac{\gamma}{\gamma-1}}$ (e.g. Becker [1968]). The pressure ratio must have at least this value to achieve supersonic flow. In this case, due to the time dependency of the nozzle exit pressure ratio and the fixed geometry, the flow is imperfectly expanded. This leads to the existence of the supersonic phenomena and the corresponding acoustic components (mainly broadband shock noise).

Ishii et al. [1999] found by applying the Rankine-Hugoniot relations across a moving shock that the required pressure ratio to generate a blast wave in a shock tube is $(p_{0r}/p_\infty)_{\text{blast}} = 41.2$. An example of a set-up with a blast wave is shown in figure 1.8*d*. In this study, the typical values for p_{0r}/p_∞ are about 3.6 and therefore only pressure waves are formed.

Didden [1979] proposed a critical size of an incompressible vortex ring ($2R_{VR}/D = 1.08$) at which it stops growing and starts propagating in the axial direction. For large values of p_{0r}/p_∞, a Prandtl-Meyer expansion was observed, leading to a widening of the flow after the nozzle exit and therefore leading to larger vortex rings before starting to propagate, see figure 1.8*d*. For values of p_{0r}/p_∞ that lead to a supersonic flow, the vortex ring has a shock wave in its front, so that the pressure of the supersonic flow inside the vortex ring is matched to the pressure ahead of the vortex ring. This is presented in figures 1.8*b*, 1.8*c* and 1.8*d*.

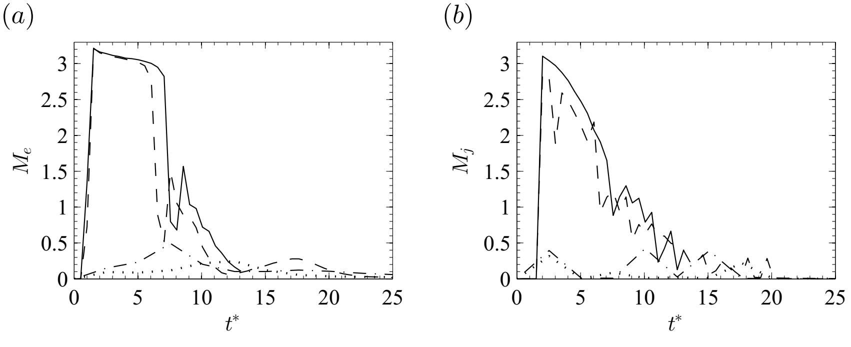

Figure 1.11: Temporal evolution of the exit (left) and fully expanded (right) Mach number. Effect of the pressure ratio. 30°, $L/D = 2$. Dotted: $p_{0r}/p_\infty = 3$ (case 13.*a*), dash-dotted: $p_{0r}/p_\infty = 4$ (case 13.*c*), dashed: $p_{0r}/p_\infty = 50$ (case 13.*e*), solid: $p_{0r}/p_\infty = 80$ (case 13.*g*).

Figure 1.11 shows the effect of the pressure ratio p_{0r}/p_∞ on the exit and fully expanded Mach number. With a divergent nozzle characterised by $A_e/A^* = 4$ and non-dimensional mass supply $L/D = 2$; the larger the pressure ratio the larger the exit Mach number. For the largest pressure ratio, $p_{0r}/p_\infty = 80$, the exit Mach number remains in the supersonic regime for a longer time than the case with $p_{0r}/p_\infty = 50$. The two smaller pressure ratios ($p_{0r}/p_\infty = 3,\ 4$) show a subsonic Mach number at all times because their pressure ratio leads to a shock wave in the divergent part of the nozzle and they have a subsonic flow at the nozzle exit. Concerning the fully expanded Mach number, the behaviour is very similar with the exception that the fully expanded Mach number does not remain constant while the nozzle is choked, while the exit Mach number does.

1.3.4 Temperature ratio (T_{0r}/T_∞)

In this study, we focused on the compressible starting jet where $\frac{T_{0r}}{T_\infty} = 1$, so this analysis is purely based on applying the principles of the isentropic one-dimensional theory of gas dynamics and results from the literature.

As a general trend, an increase of the jet temperature (T_{0r}) leads to an increase in the fully expanded temperature (T_j), since their ratio depends only on the pressure ratio p_{0r}/p_∞. Keeping a fixed pressure ratio, the fully expanded Mach number (M_j) remains constant (see equation (1.2) in the previous point). The combination of both conditions leads to:

$$\frac{T_{0r}}{T_j} = 1 + \frac{\gamma - 1}{2} M_j^2 = \left(\frac{p_{0r}}{p_\infty}\right)^{\frac{\gamma-1}{\gamma}} . \tag{1.3}$$

An increase of the fully expanded temperature causes an increase in the fully expanded speed of sound ($c_j^2 = \gamma R T_j$). A straightforward consequence of this is an increasing fully expanded velocity ($u_j = M_j c_j$).

A similar analysis can be done for the fully expanded density. The ratio ρ_{0r}/ρ_j remains constant for a fixed pressure ratio, but an increase in the reservoir temperature leads to a decrease of the reservoir density ($\rho_{0r} = p_{0r}/(R T_{0r})$).

Now, in order to evaluate the change in momentum, we have to evaluate the changes in the fully expanded velocity and density. While the velocity increases by a factor of the square root of the changes in the temperature ratio, the density decreases by the same factor than the changes in the temperature ratio, and due to this, the change in the momentum decreases by a factor of the square root of the changes of the temperature ratio, see equation (1.4c).

$$\frac{u_{j,\text{hot}}}{u_{j,\text{neutral}}} = \frac{M_{j,\text{hot}}\sqrt{\gamma R T_{0r,\text{hot}}\frac{T_{j,\text{hot}}}{T_{0r,\text{hot}}}}}{M_{j,\text{neutral}}\sqrt{\gamma R T_{0r,\text{neutral}}\frac{T_{j,\text{neutral}}}{T_{0r,\text{neutral}}}}} = \sqrt{\frac{T_{0r,\text{hot}}}{T_{0r,\text{neutral}}}} \tag{1.4a}$$

$$\frac{\rho_{j,\text{hot}}}{\rho_{j,\text{neutral}}} = \frac{p_{0r,\text{hot}}}{R T_{0r,\text{hot}}}\frac{R T_{0r,\text{neutral}}}{p_{0r,\text{neutral}}} = \frac{T_{0r,\text{neutral}}}{T_{0r,\text{hot}}} \tag{1.4b}$$

$$\frac{\rho_{j,\text{hot}} u_{j,\text{hot}}}{\rho_{j,\text{neutral}} u_{j,\text{neutral}}} = \sqrt{\frac{T_{0r,\text{neutral}}}{T_{0r,\text{hot}}}} \tag{1.4c}$$

According to Cigala et al. [2017], the effect of the jet temperature ratio is positively correlated with the maximum particle ejection velocity. This experimental observation agrees with the previous analytical argumentation. The same authors confirm that the velocity decay rate is not correlated to the temperature ratio.

Objectives of this thesis

As seen in the introduction, the continuously blown jet has been intensively studied in the literature both in the incompressible and the compressible case. The starting-decaying jet has been also extensively investigated, but only in the incompressible case. The assumption of incompressibility excludes some important features of the starting jet that are crucial for some applications, like pulse-jets, fuel injection in engines, air-bag devices and volcanoes.

The objectives of this thesis are first of all to identify the governing parameters of the compressible starting jet and to analyse the effect of them on the fluid flow and on the radiated acoustics. Second, the characterisation of the different elements of the jet when changing the governing parameters. Third, the effects of the inflow conditions by means of turbulence level and in terms of the nozzle geometry. Fourth, a full description of the acoustics radiated by the starting-decaying jet separated by its noise sources. Last, but not least, the prediction of the governing parameters of a compressible starting jet from acoustic and/or optical measurements.

With this set of objectives, a very good understanding of such a complex problem should be achieved.

Overview of this thesis

This thesis is divided into three main parts: The first part deals with the numerical framework used to perform the numerical work of this thesis. The description of the numerical model, initial and boundary conditions as well as the grid considerations are described in this part. The second part describes the experimental set-up used in this thesis as well as the equipment and the configuration used. The third part is the body of this thesis, we present here most of the outcome of this thesis, together with the discussion of the results. We tried to separate the parts concerning the fluid flow and the acoustics, with an overlap there where it was necessary. Chapter 4 deals with the characterisation of the different elements of the compressible starting jet, comparing where necessary to the incompressible case. Chapter 5 handles the effect of the inflow conditions in terms of the turbulence level. Chapter 6 defines the pinch-off in a more general and convenient way for compressible and turbulent flows. Chapter 7 presents how the trailing jet interacts with the vortex ring in the supersonic case, giving rise to one of the dominant acoustic sources of the supersonic starting jet. In this direction, chapter 8 introduces the acoustic sources of the starting jet. Having described the effect of the governing parameters and the acoustics of the starting jet, chapter 9 gives an insight in the prediction of the governing parameters from acoustic measurements. We included in this chapter also some relation with optical measurements when appropriate. As the biggest and most impressive of the applications in the nature related to the compressible starting jet, chapter 10 has been dedicated to volcanic jets.

Part I

Simulations of a compressible starting jet

Chapter 2

Numerical background

2.1 Navier-Stokes equations

An unsteady turbulent flow is generally described by the Navier - Stokes equations. They describe the conservation of mass, momentum and energy. These equations are highly non-linear and coupled with each other, but it is possible to de-couple them by applying a linearisation of small perturbations around a base-flow, obtaining three main modes: (*i*) vorticity, (*ii*) entropy and (*iii*) sound-wave. To perform this linearisation, the equations are written in pressure (p), velocity (u_i) and entropy (s) formulation and they read:

$$\frac{\partial p}{\partial t} + u_i \frac{\partial p}{\partial x_i} = -\gamma\, p\, \frac{\partial u_i}{\partial x_i} + \frac{p}{C_v}\left(\frac{\partial s}{\partial t} + u_i \frac{\partial s}{\partial x_i}\right) \tag{2.1a}$$

$$\frac{\partial u_i}{\partial t} + u_j \frac{\partial u_i}{\partial x_j} = -\frac{1}{\rho}\frac{\partial p}{\partial x_i} + \frac{1}{\rho}\frac{\partial \tau_{ij}}{\partial x_j} \tag{2.1b}$$

$$\frac{\partial s}{\partial t} + u_i \frac{\partial s}{\partial x_i} = \frac{1}{\rho T}\left(-\frac{\partial}{\partial x_i}\left(-\lambda \frac{\partial T}{\partial x_i}\right) + \Phi\right) \tag{2.1c}$$

where

$$\tau_{ij} := 2\mu\left(S_{ij} - \frac{1}{3} S_{kk}\delta_{ij}\right) \tag{2.2}$$

$$S_{ij} := \frac{1}{2}\left(\frac{\partial u_i}{\partial x_j} + \frac{\partial u_j}{\partial x_i}\right) \tag{2.3}$$

$$\Phi := \tau_{ij} S_{ij}. \tag{2.4}$$

In this set of equations, δ_{ij} denotes the Kronecker delta.

To close this set of equations, the classical assumption of an ideal gas was made:

$$p = \rho R T \tag{2.5}$$

with the gas constant $R = C_p - C_v$ and the isentropic exponent $\gamma = C_p/C_v = 1.4$. C_p is the heat capacity at constant pressure and C_v is the heat capacity at constant volume.

The viscosity is modelled using SUTHERLAND's law:

$$\frac{\mu}{\mu_{0r}} = \frac{T_{0r} + T_S}{T + T_S} \left(\frac{T}{T_{0r}} \right)^{3/2}, \tag{2.6}$$

where $T_S = 110.4$ K is the Sutherland's temperature. T_{0r} denotes the total temperature and μ_{0r} the corresponding viscosity.

We modelled the heat conductivity (λ) following Fourier's law:

$$\lambda = \mu \frac{C_p}{\mathrm{Pr}}, \tag{2.7}$$

with Pr$= 0.71$ as Prandtl number.

The three-dimensional compressible Navier-Stokes equations ((2.1)$a-c$) are solved in characteristic form as in [Sesterhenn, 2000]. This has two main advantages: (*i*) the implementation of boundary conditions for aeroacoustic applications is straightforward (for example a non-reflecting boundary condition is implemented by setting the incoming wave to zero) and (*ii*) the suitability of upwind schemes, where the up- and down travelling waves are discretised with the up- and downwind schemes, respectively.

The hyperbolic part of the Navier-Stokes equations is discretised with a fifth-order upwind scheme following [Adams and Shariff, 1996]. The remaining terms of the equations (heat flux and friction terms) are of parabolic nature and are discretised with a sixth-order central scheme with spectral-like resolution following [Lele, 1992].

For the time integration, a classical low-storage Runge-Kutta method of fourth-order is used. All simulations have an explicit CFL number in the range $[0.3 - 0.7]$, leading to a time step size of $dt = 1.545 \cdot 10^{-5}$ for the largest resolution ($2048 \times 1024 \times 1024$), $dt = 1.768 \cdot 10^{-5}$ for the medium resolution ($1024 \times 512 \times 512$) and $dt = 2.788 \cdot 10^{-5}$ for the lowest resolution ($512 \times 256 \times 256$).

2.2 Grid considerations

Since we mainly focus on turbulence and acoustics, the strongest requirement for the computational grid in our direct numerical simulations (DNS) is to resolve the smallest turbulent scales present in the flow field. As a consequence, the smallest resolved acoustic wavelengths are of the same size than the Kolmogorov length. The Cartesian geometry of length $25D \times 15D \times 15D$ was chosen to be discretised with $2048 \times 1024 \times 1024$ grid-points for the cases 7.b (with $Re_D = 10\,000$) and 7.c (with $Re_D = 5000$ highly resolved). The resolution $512 \times 256 \times 256$ was chosen for the rest. While the grid is equidistant in the axial direction, both transverse directions have been discretised using a grid stretching, as proposed by Anderson et al. [1984] and shown in figure 2.1:

$$y(\eta) = y_0 + \eta_c \left(\frac{\sinh(\tau_y(\eta - B))}{\sinh(\tau_y B)} + 1 \right) L_y, \tag{2.8}$$

where L_y represents the length of the domain in y direction (the same applies for z direction) and y_0 is the offset to the centre of the domain in the corresponding direction, to work with η_c and τ_y in non-dimensional units from 0 to 1. η_c is the centre of the refinement in non-dimensional units (we used the value $\eta_c = 0.5$) and τ_y is the amount of refinement (we used the value $\tau_y = 4$), so that the ratio biggest to smallest element are in the ratio τ_y. The parameter B is defined as:

$$B = \frac{1}{2\tau_y} \ln \left(\frac{1 + (e^{\tau_y} - 1)\eta_c}{1 + (e^{-\tau_y} - 1)\eta_c} \right). \tag{2.9}$$

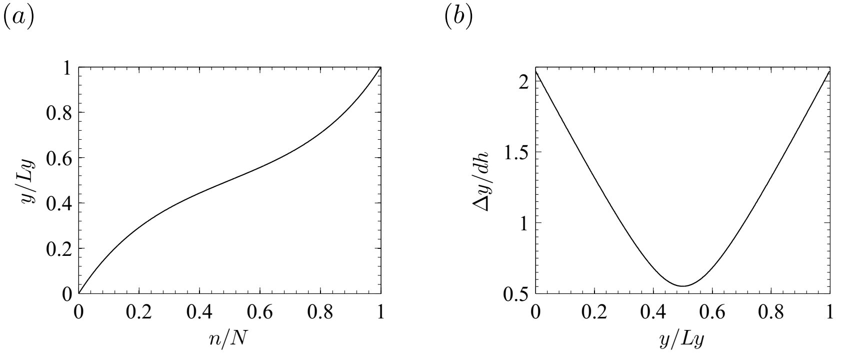

Figure 2.1: Grid stretching used in a typical simulation of this thesis. (a) Grid distribution presenting the physical space versus the computational one. (b) Grid cell spacing normalised to the equivalent equidistant cell spacing ($dh = L_y/N$). Values below one show the refined area.

A schematic representation of the finest grid is shown in figure 2.2. The resolution chosen for all simulations is sufficient to resolve the Kolmogorov scale, see figure 2.3. This is supported and extended in tables 2.1 and 2.2 and figure 2.4. The turbulent spectra of figures 2.3 and 2.4 were calculated using the velocity fluctuations with respect to the azimuthal average: $u' = u - \langle u \rangle_\theta$, where u is the instantaneous velocity and $\langle u \rangle_\theta$ is the

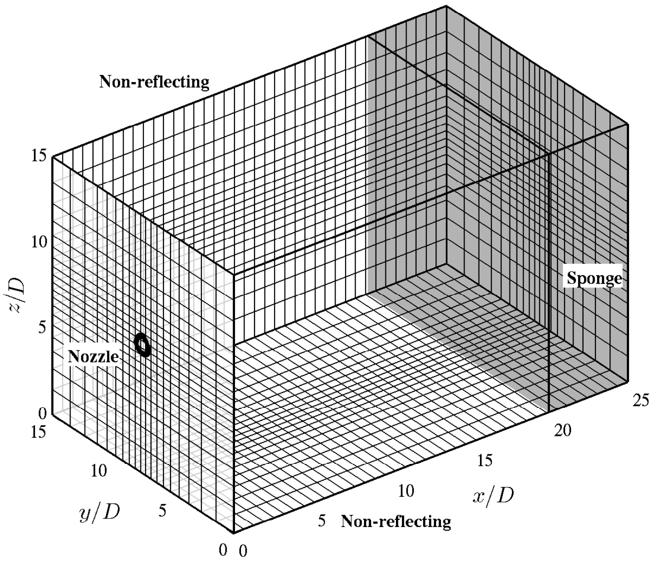

Figure 2.2: Computational grid for the finest simulation (case 7.c). Only every 50^{th} point is shown.

Table 2.1: Grid spacing considerations for the three-dimensional cases in this study. The characteristic length of the smallest element in the domain is defined as $d_{\text{grid}} = (dx_{\min} + dy_{\min} + dz_{\min})/3$. $\eta_{\min}$ is the minimum Kolmogorov length scale found in the flow field. $\nu_\infty = \nu(T_\infty)$ is the kinematic viscosity at the temperature of the unbounded chamber in m^2/s. Here λ is, exceptionally, the free mean path of the fluid.

Case	Re_D	$n1 \times n2 \times n3$	$\frac{D}{d_{\text{grid}}}$	$\frac{\eta_{\min}}{d_{\text{grid}}}$	$\frac{10\lambda}{d_{\text{grid}}}$
$1-7.a$	5 000	$512 \times 256 \times 256$	25.84	0.91	0.11
$7.b.$	10 000	$2048 \times 1024 \times 1024$	103.09	1.93	0.23
$7.c.$	5 000	$2048 \times 1024 \times 1024$	103.09	2.99	0.23
$7.d.$	15 000	$2048 \times 1024 \times 1024$	103.09	0.87	0.23
$7.e.$	5 000	$512 \times 256 \times 256$	25.84	0.91	0.11
$8-10$	5 000	$640 \times 256 \times 256$	25.84	0.91	0.11
$11-13$	3 000	$1024 \times 512 \times 512$	51.68	1.365	0.017

mean velocity averaged in the azimuthal direction. The minimum value of the Kolmogorov length scale $\eta_{\min}$ compared to the characteristic length

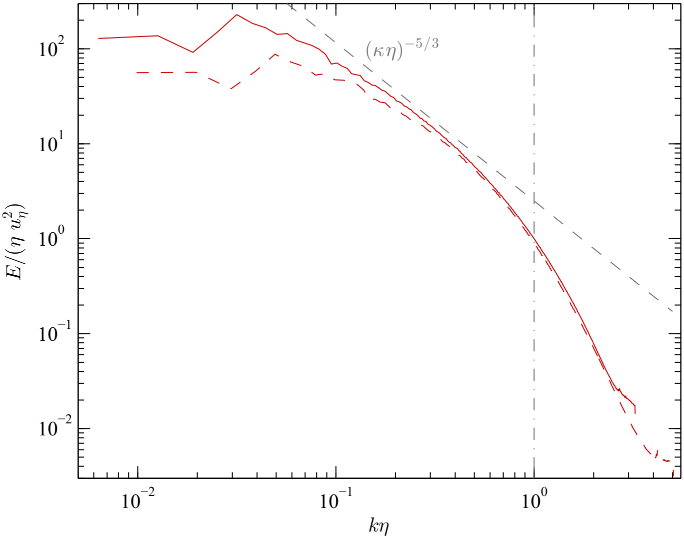

Figure 2.3: Non-dimensional turbulent kinetic energy spectra for the cases 7.*b* (solid red) with a $Re_D = 10\ 000$ and 7.*c* (dashed red) with a $Re_D = 5\ 000$. The grey dot-dashed line represents the wavenumber associated to the Kolmogorov length scale. As a reference, the $-5/3$ decay line has been plotted in grey.

of the smallest element in the domain ($d_{\text{grid}} = (dx_{\text{min}} + dy_{\text{min}} + dz_{\text{min}})/3$) is very close to one in the worst case (7.*d*). The Kolmogorov length scale (calculated as $\eta = \left(\nu^3/\varepsilon\right)^{1/4}$, where $\varepsilon = \nu\langle \frac{\partial u_i'}{\partial x_j}\frac{\partial u_i'}{\partial x_j}\rangle$) is time dependent and decreases during the starting phase, while it increases during the decay phase. Comparing both spectra corresponding to the large resolution ($2048 \times 1024 \times 1024$), see figure 2.3, we find a good agreement in the dissipation range as well as in the inertial sub-range. The spectra of case 7.*b* corresponding to $Re_D = 10\ 000$ has a longer inertial sub-range and there is more energy associated with big scales, as expected. Only a few points are in the energy containing scales and since the data are not time averaged, but for a single realisation, the agreement appears to be satisfactory. All spectra present a small peak for high wave-numbers, which corresponds to the error associated to the interpolation to an equidistant grid to perform the Fourier transformation. In the energy spectrum normalised with the nozzle diameter D (figure 2.4), the maximum turbulent kinetic energy can be seen for all three cases at scales of the same order of magnitude as the nozzle diameter represented by the grey dot-dashed line, where the simulation with the largest Reynolds number has a longer inertial sub-range,

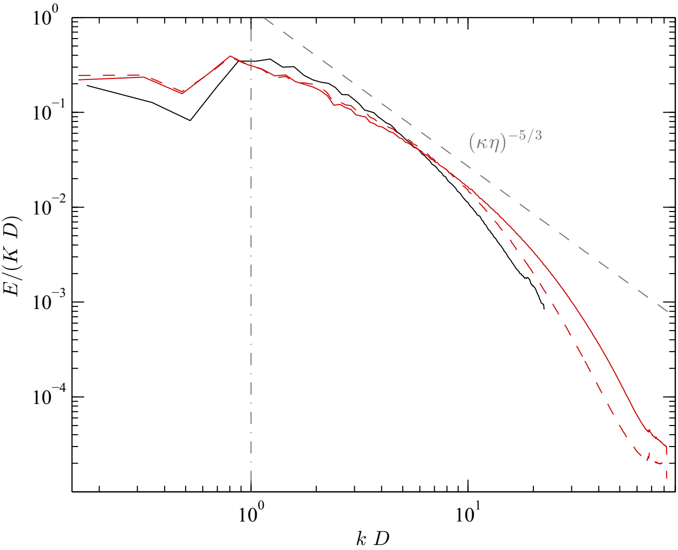

Figure 2.4: Non-dimensional turbulent kinetic energy spectra for the cases 7.a (black) with a $Re_D = 5\ 000$, 7.b (solid red) with a $Re_D = 10\ 000$ and 7.c (dashed red) with a $Re_D = 5\ 000$. The grey dot-dashed line represents the wavenumber associated to the nozzle diameter. As a reference, the $-5/3$ decay line has been plotted in grey.

followed by the dissipation range.

The width of an inviscid shock wave is approximately one order of magnitude larger than the mean free path, Salas and Iollo [1996]. Using non-dimensional analysis, the Knudsen number can be expressed in the form $Kn = \lambda/D = M_j\sqrt{\gamma\pi/2}/Re$ and since the characteristic length in this study (the nozzle diameter, D) is chosen to be unity, the mean free path (λ) –and therefore the thickness of the shock waves (10 λ)– is much smaller than the grid elements ($10\lambda/d_{\text{grid}}$ in tables 2.1 and 2.2). We used the shock capturing filter from Bogey et al. [2009].

The cases with a $Re_D = 5000$ have a $\nu_\infty = 0.04 m^2/s$, while the cases with $Re_D = 10\ 000$ have a $\nu_\infty = 0.02\ m^2/s$.

Table 2.2: Grid spacing considerations for the two-dimensional cases in this study. The characteristic length of the smallest element in the domain is defined as $d_{\mathrm{grid}} = (dx_{\min} + dy_{\min})/2$. $\eta_{\min}$ is the minimum Kolmogorov length scale. $\nu_\infty = \nu(T_\infty)$ is the kinematic viscosity at the temperature of the unbounded chamber in m^2/s. Here is λ exceptionally the free mean path of the fluid. An estimation of the shock wave thickness (as proposed by Salas and Iollo [1996]) compared to the smallest element in the domain is denoted by $10\lambda/d_{\mathrm{grid}}$.

Case	Re_D	$n1 \times n2$	D/d_{grid}	$\eta_{\min}/d_{\mathrm{grid}}$	$10\lambda/d_{\mathrm{grid}}$
14	8 000	3072 × 1536	409.47	5.95	0.49
15	5 000	1536 × 768	204.67	4.67	0.06
16	5 000	3072 × 1536	409.47	10.5	1.47
17	10 000	3072 × 1536	409.47	5.17	0.80
18	5 000	1536 × 768	204.67	1.73	0.80
19	5 000	3072 × 1536	409.47	3.97	1.85
20	5 000	3072 × 1536	409.47	2.70	1.85
21	5 000	3072 × 1536	409.47	2.34	2.93
22	5 000	3072 × 1536	409.47	2.49	3.89
23	2 000	4608 × 2304	307.13	6.82	1.42
24	5 000	4608 × 2304	307.13	6.28	0.568
25	10 000	4608 × 2304	307.13	6.15	0.284

2.3 Parallelization

Considering a grid like the one introduced in the previous section, with more than two billion (2×10^9) grid points, running approximately 10^5 time steps to analyse statistically the flow, the need of millions of CPU hours is obvious. A massive parallelization is necessary for the feasibility of this research project.

With this approach, every CPU solves the Navier-Stokes equations in a part of the domain. The cores need to communicate with each other since their solution depends on the neighbours one. When computing derivatives, the finite difference stencil needs information about the solution in the neighbour points. In this study, the communication is based on a hybrid approach using the Message Passing Interface (MPI) and OpenMP methods. While OpenMP manages the communication of the cores within a processor to avoid bottlenecks, the MPI manages the communication inter-processor.

All simulations were performed in the Leibniz Rechnenzentrum (LRZ), equipped with *Xeon E5-2680 8C* processors at 2.70 GHz and it is currently in position 36 of the most powerful supercomputing centres in the world[1].

---

[1] According to Top500 List in November 2016. http://www.top500.org.

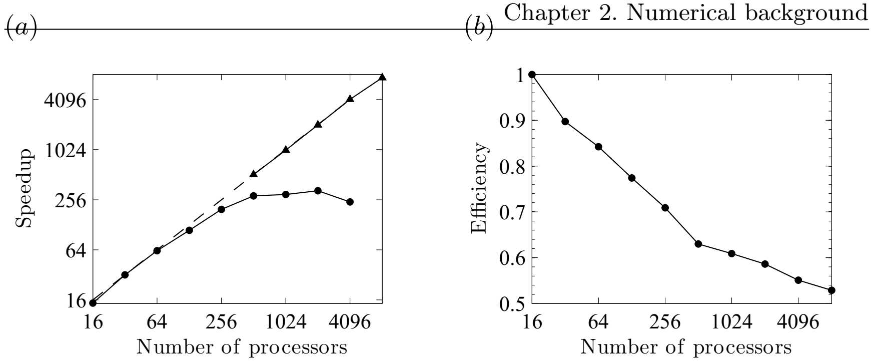

Figure 2.5: (*a*) Scaling plot keeping the grid constant and increasing the paralellisation (strong scaling). A small case ($128 \times 256 \times 32$) normalised to 32 cores is represented by (●). A large case ($1024 \times 512 \times 512$) normalised to 512 cores corresponds to (▲). The ideal speed-up is represented by the dashed line. (*b*) Scaling plot keeping the grid per core constant and increasing the number of blocks (weak scaling). A constant block of ($16 \times 16 \times 16$) grid points per core was analysed.

To the best knowledge of the author, the biggest simulations in this study are the largest simulations of a jet until now.

With a low loading of the cores as (●) in figure 2.5a, the communication time becomes dominant and a larger number of cores does not imply a speedup. The last point of this curve corresponds to a paralellisation with 6 grid points per core in every direction, and the communication time dominates the computing time. For a high loading of the cores, corresponding to (▲) in the same figure, starting with the first point, it corresponds to 80 grid points per core and direction, and the computing time dominates the communication time. Therefore, adding more cores implies an ideal speedup, as long as this condition holds.

We found an optimal load of the cores at 29 grid points per core and direction and because of this, we used typically in this study, for the low-resolution ones we used 1024 cores (which means 32 grid points per core and direction) and for the high-resolution simulations 8192 cores (which means 64 grid points per core and direction). For the high-resolution simulations, we used 64 grid points per core and direction to fit the simulations within a single 'island' in the supercomputing centre, a unit of the supercomputing centre where the CPUs are connected via a high-speed non-blocking network (Infiniband).

2.4 Initial conditions

Concerning the initial conditions, quiescent flow is imposed over the whole computational domain in order to study an impulsively starting jet, setting the pressure to the ambient pressure and the entropy to the ambient entropy.

2.5 Boundary conditions

The truncation of the computational domain includes additional unwanted information in the solution, and to minimise the effect of this additional unwanted information, we impose a known solution at the boundaries (boundary conditions), so that the solution inside the computational domain reaches the known solution at the boundary of the computational domain and its surroundings.

In the four lateral faces of the computational domain, non-reflecting boundary conditions are set in order to be able to study the acoustic phenomena that are present in the starting jet.

At the outlet, a sponge region is set in order to avoid the reflection of the waves that are travelling towards the end of the computational domain.

Since the flow inside the nozzle is not computed in most of the cases, the variation of the inlet condition with the non-dimensional time ($t^* = t/(D_j/U_j)$, where D_j and U_j are the fully expanded diameter and velocity, respectively) is modelled as

$$\left.\frac{p_e(t^*)}{p_\infty}\right|_{y,z=0} = 1 + \frac{p_{0r}/p_\infty}{\mathrm{NPR}} \exp\left(\frac{-t^*}{C}\right) \tanh(Kt^*), \tag{2.10}$$

where NPR is the nozzle pressure ratio, defined as the ratio of reservoir total pressure to nozzle exit pressure p_{0r}/p_e. The one-dimensional isentropic theory predicts an exponential decay of the pressure in the deposit when discharging. We linked the initial state of quiescence with the exponential decay through a hyperbolic tangent. This is similar to the experimental work of Cimarelli et al. [2014], where the pressure time distribution measured at the nozzle exit matches qualitatively with the model used in this study. If the nozzle is not choked ($M_e < 1$), $p_e = p_\infty$ because the nozzle is always adapted in the subsonic regime. However, if a convergent nozzle is choked ($M_e = 1$), $\mathrm{NPR}^* = ((\gamma+1)/2)^{(\gamma/(\gamma-1))}$ [Becker, 1968], and $p_e \neq p_\infty$, because the flow in a convergent nozzle in supersonic regime is never adapted. Equation (2.10) is plotted in figure 2.6*a*. The constant K modifies the hyperbolic tangent term, which is responsible for the impulsive stage, corresponding to the stage (*i*). The larger K, the more impulsive is the first stage. We used $K = 60$ as a trade-off between the stability of the code and high enough gradients in the first stage to give the jet the impulsive character. The same way, the constant C modifies the exponential term, which is responsible for the decay, corresponding to the stage (*ii*). The larger C, the faster is the decay, which also implies a smaller volume

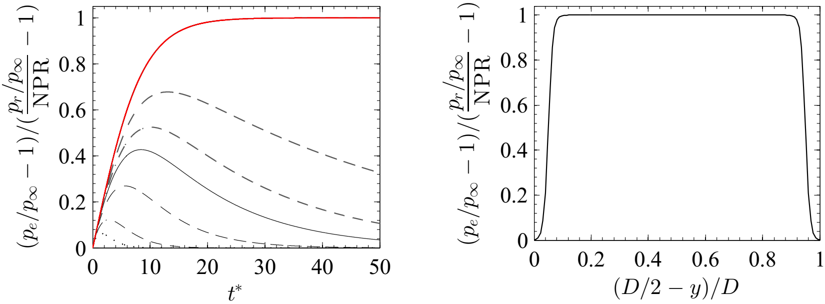

(a) Pressure temporal distribution at the nozzle exit centerline. Lines as in table 2.3.

(b) Pressure distribution at the nozzle exit plane for the case 7.a for $t^* = 50$.

Figure 2.6: Nozzle exit conditions for the starting jet.

of the reservoir.

The spatial pressure distribution imposed at the inlet ($p_e(y,z)/p_\infty$), shown in figure 2.6b, was modelled by,

$$\left.\frac{p_e(y,z)}{p_\infty}\right|_{t_0} = 1 + \left(\frac{p_{0r}/p_\infty}{\mathrm{NPR}} - 1\right) \left\{\frac{1}{2} - \frac{1}{2}\left[\tanh\left(\frac{\sqrt{y^2+z^2} - \frac{1}{2}(D - \delta_{\omega_0})}{l_{\mathrm{mass}}}\right)\right]\right\}, \tag{2.11}$$

with a shear layer thickness of $\delta_{\omega_0} = 0.1D$. The most common spatial distribution of the inlet condition when numerically simulating a jet is a hyperbolic tangent, due to the good control over the gradients of the distribution to generate unstable Kelvin-Helmholtz vortices. We used this distribution as well, adding the unsteady part to take into account the time evolution of the inlet condition. This, together with a relatively large Reynolds number led to a fully turbulent shear layer shortly after the nozzle exit. The parameter $l_{\mathrm{mass}} = \delta_{\omega_0}/(2\pi)$ controls the position of the shear layer in the nozzle, imposing the beginning of the shear layer at the wall and not centred into the wall $M(r/D = 0.5) = 0$.

Figure 2.7 shows the discretisation of the inlet condition at the nozzle exit for simulations with different resolutions. The colour scale represents the relative velocity to the corresponding in the centerline, giving an idea about the two-dimensional profile. By using a resolution of $512 \times 256 \times 256$, we discretised the nozzle exit diameter with 25 grid points, while using a resolution of $1024 \times 512 \times 512$, the nozzle diameter was discretised with 51 grid points. In the largest resolution, $2048 \times 1024 \times 1024$, the nozzle

Table 2.3: Short summary of the cases $1.a$, $2-6$, $7.a-e$ involved in the trailing jet analysis to show the parameters used for the boundary condition. $p_{0r}/p_\infty = 3.60$. The supersonic non-dimensional time interval is represented with $t^*_{M_j>1}$.

Case	C	L/D	$\max(M_j)$	$t^*_{M_j>1}$	legend
$1.a$	1	0.45	0.40	-	··········
2	2	1.17	0.55	-	–·–·–·
3	5	3.80	0.81	-	- - - - -
4	10	8.60	1.01	$4.66-6.92$	———
5	15	13.55	1.11	$3.75-14.16$	--·--·
6	30	28.59	1.25	$3.60-32.75$	– – –
$7.a-e$	10^7	∞	1.49	$3.83-$	———

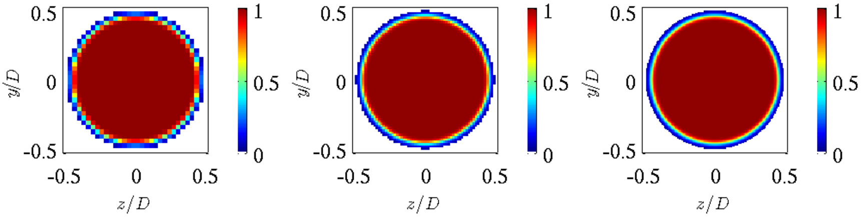

(a) $512\times256\times256$ (b) $1024\times512\times512$ (c) $2048\times1024\times1024$

Figure 2.7: Discretisation of the inlet condition at the nozzle exit for different resolutions. The colour-scale indicates the relative velocity to the corresponding in the centerline of the jet (u/u_c).

diameter was discretised with 103 grid points.

2.6 Porous media / volume penalisation method

In order to create a proper boundary condition, porous media have been commonly used in the literature using the volume penalisation method. In this section, we briefly describe the method used. Porous media was used in this thesis for the generation of a nozzle geometry in case 8 and the analysis of the straight and divergent nozzles in cases $11.a-13.h$.

Two parameters are needed to characterise a porous medium: the porosity ϕ and the permeability $\boldsymbol{K}$. While ϕ describes the volume ratio of void space V_f to the volume of the whole porous material ($\phi = V_f/V$), $\boldsymbol{K}$ stands for the permeability of the material.

A porosity equal to one represents a void space and a porosity of zero a solid body. The permeability of the material $\boldsymbol{K}$ and is a symmetric and positive definite tensor and the entries in this tensor can reach values of zero for a material which is not permeable (solid) and infinity for a material with no influence on the fluid.

To include the effect of a porous medium in the simulation, the equations of continuity, momentum and energy have to be modified. The main idea is based on a relation reported by Darcy [1856] that relates the flow velocities and the pressure gradient with the permeability of the porous medium in a linear way. This relation, called Darcy's law, has been used in a similar simulation in Schulze [2011] and reads:

$$\boldsymbol{v} = -\frac{\boldsymbol{K}}{\mu}\nabla p,$$

with the so called Darcy velocity $\boldsymbol{v} = \phi\boldsymbol{u}$. This additional volume force is added to the momentum equation and acts as a sink term damping all velocities in the porous medium. Moreover, the changes in density have to be implemented as well:

$$\phi = \frac{V_f}{V} = \frac{\rho}{\rho_f}.$$

The modified continuity equation can be expressed as:

$$\frac{\partial\phi\rho}{\partial t} + \frac{\partial\phi\rho u_i}{\partial x_i} = 0, \tag{2.12}$$

where the density of the fluid $\rho_f = \phi\rho$ has been introduced.

Based on the same argumentation line, the modified momentum equation is:

$$\frac{\partial u_i}{\partial t} + u_j\frac{\partial u_i}{\partial x_j} = -\frac{1}{\phi\rho}\frac{\partial p}{\partial x_j} + \frac{1}{\phi\rho}\frac{\partial\tau_{ij}}{\partial x_j} - \frac{\mu}{\rho}\left(K^{-1}\right)_{ij}u_j, \tag{2.13}$$

and the modified energy equation is:

$$C_v\frac{DT}{Dt} + \frac{D}{Dt}\left(\frac{1}{2}u_iu_i\right) = \frac{1}{\phi\rho}\frac{\partial}{\partial x_j}\left(-pu_j + u_i\tau_{ij} + \left(\lambda\frac{\partial T}{\partial x_j}\right)\right). \tag{2.14}$$

The numerical implementation of the equations and the validation of the method are out of the scope of this thesis and can be followed in [Schulze, 2011].

2.7 Sponge region

When a vortex pair reaches the outflow boundary of the computational domain it generates 'reflected waves' when they are truncated by the boundary. Therefore we numerically treat the layer close to the outflow boundary by adding a damping term $\sigma(\boldsymbol{x})$:

$$\frac{\partial\boldsymbol{q}}{\partial t} = \mathrm{NS}(q) - \tau_{sp}\,\sigma(\boldsymbol{x})(\boldsymbol{q} - \boldsymbol{q_0}), \tag{2.15}$$

where $\boldsymbol{q}$ represents the flow state, $\mathrm{NS}(q)$ is the Navier-Stokes operator, $\sigma(\boldsymbol{x})$ is the damping function, $\boldsymbol{q_0}$ represents the reference flow state and τ_{sp} is the amplitude or strength of the sponge layer. This damping term makes the sponge region not physical but allows us to keep physical results in the rest of the domain. The choice of $\sigma(\boldsymbol{x})$, $\boldsymbol{q_0}$ and τ_{sp} has to be done carefully to avoid numerical instabilities when damping too much and acoustic reflections when damping too less. In the compressible starting jet, we chose the reference flow state $\boldsymbol{q_0}$ as quiescence.

The damping function $\sigma(\boldsymbol{x})$ is required to be smooth to dissipate the energy slowly without reflect any information backward to the rest of the domain. The sponge function implemented in this study can be expressed as:

$$\sigma(\boldsymbol{x}) = \frac{1}{2}\left(1 + \operatorname{erf}\left(\frac{2}{L_{X_p}}(x - C_{X_p})\right)\right), \tag{2.16}$$

where $L_{X_p} = 5D$ is the length of the sponge region in x direction starting from $C_{X_p} = 25D$ to have enough points to damp the solution close to the outlet. This function is shown in figure 2.8.

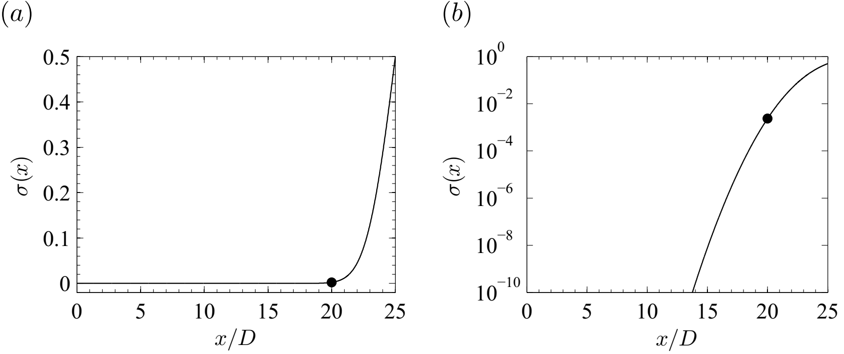

Figure 2.8: Sponge damping function $\sigma(x)$. (*a*) Linear representation. (*b*) Logarithmic representation. The beginning of the sponge layer (●) was set to $x/D = 20$.

2.8 Simulations setup

Table 2.4 shows a general overview of the different set-ups considered in this study. The vortex ring dynamics were analysed with the simulations $1.a-c$. Simulations $2-6$ simulated starting and decaying jets with different reservoir sizes in order to analyse how this affects the trailing jet. The trailing jet for the starting jet without decay was analysed by the cases $7.a-e$. Until this point, we used the basic configuration of a starting

Table 2.4: General set-up of the simulations in this study. Simulations from 1 to 13 are $3D$ and from 14 to 26 are $2D$.

Case	starting jet	decaying jet	porous media	inflow condition	Analysis
$1.a - c$	✓	✓	—	laminar	Vortex Ring
$2 - 6$	✓	✓	—	laminar	Trailing jet
$7.a - e$	✓	—	—	laminar	Trailing jet
8	—	—	straight nozzle	nozzle	Inflow conditions
9	—	—	—	TBL	Inflow conditions
10	—	—	—	laminar	Inflow conditions
$11.a - h$	✓	✓	straight nozzle	nozzle	p_{0r}/p_∞, L/D
$12.a - h$	✓	✓	divergent nozzle	nozzle	p_{0r}/p_∞, L/D
$13.a - h$	✓	✓	divergent nozzle	nozzle	p_{0r}/p_∞, L/D
$14 - 26$	✓	✓	—	laminar	Main parameters

jet as described in the introduction with different values for the governing parameters. Cases $8 - 10$ focused on the effects of the inflow condition by changing the spatial distribution of the inlet condition. The analysis of the effect of the nozzle geometry on the fluid flow and acoustics was done based on cases $11.a - 13.h$; here different geometries were analysed. All cases enumerated until here were simulated in three dimensions. Cases $14 - 26$ were simulated in two dimensions to scan different regions of the parameter space with special importance.

Cases $1.a - c$ focused on the vortex ring dynamics and for this purpose we simulated low incompressible, high compressible and supersonic starting and decaying jets with very short reservoirs, generating a single vortex ring without trailing jet. The values used for the parameters can be seen in table 2.5. We show in section 4.2.3 how the compressibility affects the vortex ring dynamics.

Cases $2-6$ together with $1.a$ and $7.a$, which are the natural continuation of the parameter values, focused on the trailing jet formation and dynamics for different reservoir sizes. The parameters used are summarised in table 2.6. Case $7.a$ was introduced in this analysis to compare as well with the

Table 2.5: Governing parameters of the analysis of the vortex ring dynamics. The temperature ratio $T_{0r}/T_{\infty} = 1$ for all cases. All cases are generated with a convergent nozzle: $A_e/A^* = 1$. The Reynolds number based on the nozzle diameter was set to $Re_D = 5\ 000$ for these cases.

Case	L/D	p_{0r}/p_{∞}
1.a	0.45	3.6
1.b	0.0436	20.63
1.c	0.091	96.36

Table 2.6: Governing parameters in the analysis of the existence of the trailing jet. The temperature ratio $T_{0r}/T_{\infty} = 1$ for these cases. These cases are generated with a convergent nozzle: $A_e/A^* = 1$. The Reynolds number is set to be $Re_D = 5\ 000$ for these cases.

Case	L/D	Re_D	p_{0r}/p_{∞}
1.a	0.45	5 000	3.6
2	1.17	5 000	3.6
3	3.80	5 000	3.6
4	8.6	5 000	3.6
5	13.55	5 000	3.6
6	28.59	5 000	3.6
7.a	∞	5 000	3.6

starting jet without decay.

The trailing jet was analysed for the starting jet without decay for the cases 7.$a - e$ with the parameters shown in table 2.7. The starting jet without decay (from an infinite reservoir) allows to study the properties of the trailing jet assuming a statistically steady system.

Table 2.7: Governing parameters analysis trailing jet for an infinite reservoir. $T_{0r}/T_{\infty} = 1$, $A_e/A^* = 1$, $L/D \to \infty$.

Case	Re_D	p_{0r}/p_{∞}	Resolution
7.a	5 000	3.6	Low
7.b	5 000	3.6	High
7.c	10 000	3.6	High
7.d	15 000	3.6	High
7.e	5 000	4.35	Low

In order to analyse the effect of the inflow conditions in the jet flow and its acoustics, we simulated three different cases 8, 9 and 10 with the parameters summarised in table 2.8. Here we did not take into account the effect of the geometry, but the effect of the turbulence level at the inlet.

Table 2.8: Governing parameters analysis inflow conditions. The temperature ratio $T_{0r}/T_\infty = 1$ for all cases. $A_e/A^* = 1$ for all cases. $L/D \to \infty$, $Re_D = 5000$.

Case	p_{0r}/p_∞	inlet
8	3.786	nozzle
9	4.35	TBL
10	3.956	laminar

We took into account the effects of the geometry in cases $11.a-h$, $12.a-h$ and $13.a-h$ by simulating different nozzle geometries, characterised by A_e/A^*. Table 2.9 shows the parameters used here.

Table 2.9: Governing parameters in the analysis of the geometry, non-dimensional mass supply and pressure ratio. The temperature ratio $T_{0r}/T_\infty = 1$ for all cases. $Re_D = 3\ 000$.

Case	L/D	p_{0r}/p_∞	A_e/A^*
$11.a$	2	3	1
$11.b$	8	3	1
$11.c$	2	4	1
$11.d$	8	4	1
$11.e$	2	50	1
$11.f$	8	50	1
$11.g$	2	80	1
$11.h$	8	80	1
$12.a$	2	3	2.358
$12.b$	8	3	2.358
$12.c$	2	4	2.358
$12.d$	8	4	2.358
$12.e$	2	50	2.358
$12.f$	8	50	2.358
$12.g$	2	80	2.358
$12.h$	8	80	2.358
$13.a$	2	3	4
$13.b$	8	3	4
$13.c$	2	4	4
$13.d$	8	4	4
$13.e$	2	50	4
$13.f$	8	50	4
$13.g$	2	80	4
$13.h$	8	80	4

In order to scan important regions of the parameter space, we performed as well two-dimensional simulations of the cases $14-22$, whose parameters are presented in table 2.10.

Table 2.10: Governing parameters in the analysis of the governing parameters. The temperature ratio $T_{0r}/T_{\infty} = 1$ for all cases. All cases are generated with a convergent nozzle: $A_e/A^* = 1$.

Case	L/D	Re_D	p_{0r}/p_{∞}
14	20	8 000	1.3251
15	∞	5 000	1.007
16	100	5 000	2.46
17	100	10 000	2.84
18	∞	5 000	2.84
19	2	5 000	3.786
20	8	5 000	3.786
21	2	5 000	15
22	0.1345	5 000	50

An important part of the parameter space for numerical simulations is the Reynolds number, so we segregated this cases from the rest of the two-dimensional simulations for a Reynolds number analysis. Table 2.11 indicates the values used for the governing parameters in these simulations.

Table 2.11: Governing parameters in the analysis of the Reynolds number. $T_{0r}/T_{\infty} = 1$, $A_e/A^* = 1$. $p_{0r}/p_{\infty} = 2.46$, $L/D \to \infty$.

Case	Re_D
23	2 000
24	5 000
25	10 000

Part II

Experiments of a compressible starting jet

Chapter 3

Experimental setup

Two different families of experiments have been performed in this work: (*i*) natural experiments in which we measured directly on a volcano and (*ii*) analogic experiments in the laboratory reproducing partially the same physical process of the natural case but with simplified boundary conditions in order to study the effect of a specific parameter. In the course of gas dynamics offered at the department prof. Sesterhenn, together with the technical staff (Christian Westphal) and the research assistant (myself) do once a year an experiment of the jet flow for academic purposes; some of the results obtained there are also present in this work. For the sake of simplicity, we will start describing the analogic experiments in the laboratory.

We performed the measurements in the anechoic chamber facility of the Berlin Institute of Technology (Department of Technical Acoustics). Figure 3.1 shows the general set-up of the anechoic chamber. It has a free volume of 1070 m^3 and a walkable area of 126 m^2. The lower frequency limit is 63 Hz.

In the anechoic chamber facility, we performed acoustic measurements of continuous and starting jets as well as schlieren photography. They are described in more detail in the following sections.

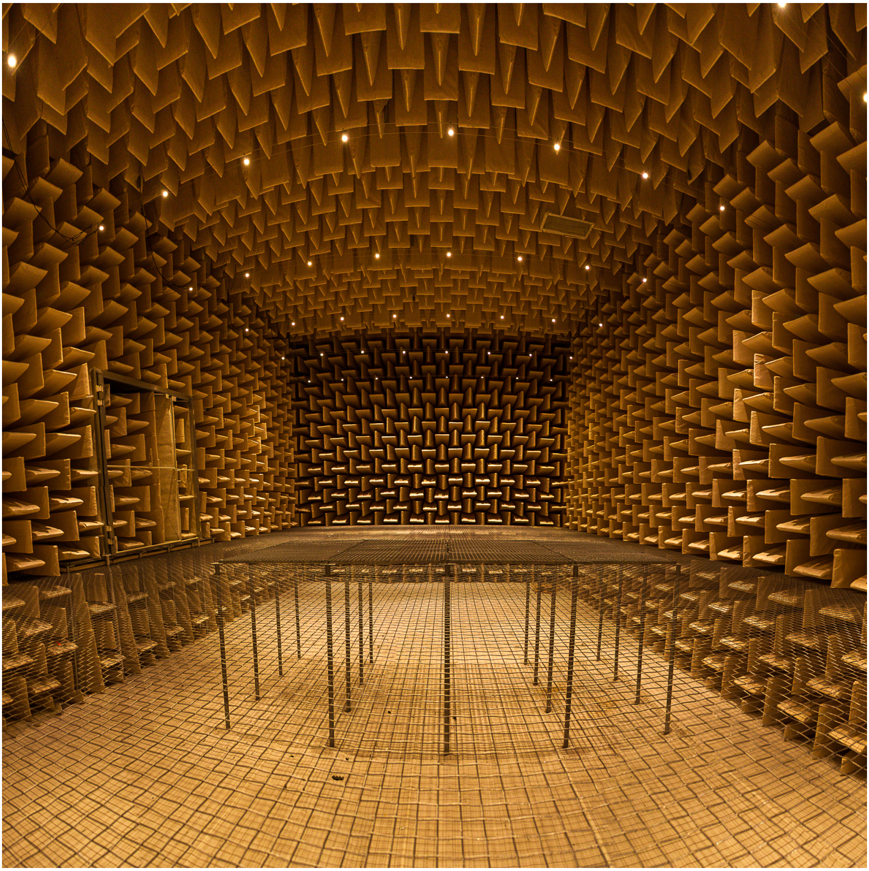

Figure 3.1: General set-up in the anechoic chamber.

3.1 Schlieren photography

Schlieren photography is based on the changes of the refractive index of fluids when changing their thermodynamical state. We use the dependence of the refractive index with the density (see the Snell's law in equation 3.1) by illuminating the object under study with perfect parallel light; this will be refracted in a different way by the regions with different densities. Focusing this light through a lens into a camera we can record the density gradients of the fluid flow.

$$\frac{\sin\theta_1}{\sin\theta_2} = \frac{n_2}{n_1} \tag{3.1}$$

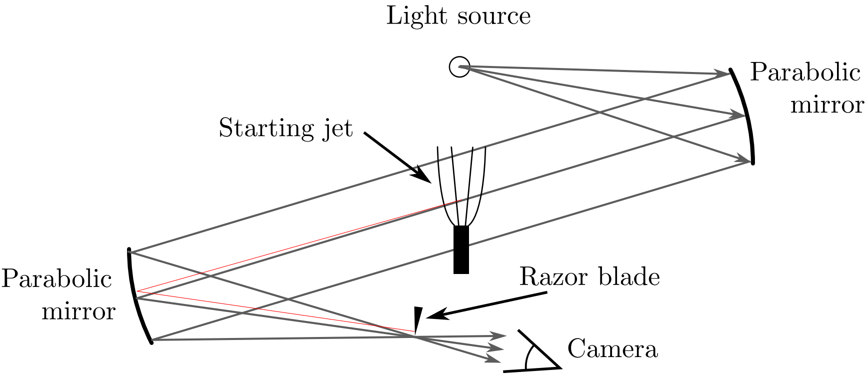

Figure 3.2: Sketch of a classical Z-type schlieren set-up.

Figure 3.2 shows a sketch of a classical Z-type schlieren set-up that we used for our schlieren experiments (figure 3.3*a* shows the set-up used). In order to obtain perfect parallel light we have a point light source (see figure 3.4*a*) located exactly at the focal point of a parabolic mirror; when the diverging light rays from the source are reflected in the parabolic mirror, they are reflected as perfect parallel light rays. These parallel light rays illuminate the starting jet. Here several things happen: some of the light rays are completely blocked because they illuminate the body of the nozzle; some of the rays are undistorted because they do not pass through the starting jet, but beside it; and some of the rays pass through the starting jet and are refracted with different angles due to the spatial distribution of the refractive indices in the flow field. In order to record the information, we collect the light rays through a second parabolic mirror focusing the light into a camera (see figures 3.3*b* and 3.4*b*). This second parabolic mirror will focus all perfect parallel light rays in a single point, but the deflected rays will be focused in a different point out of the camera sensor. This generates a picture at the camera where shadows are shown for the regions where the light was refracted. Typically this has been called shadowgraph photography. In order to block the light rays not focused by the parabolic mirror in the focal point, we placed a razor blade at the focal point. This razor blade makes the difference between shadowgraph and schlieren photography.

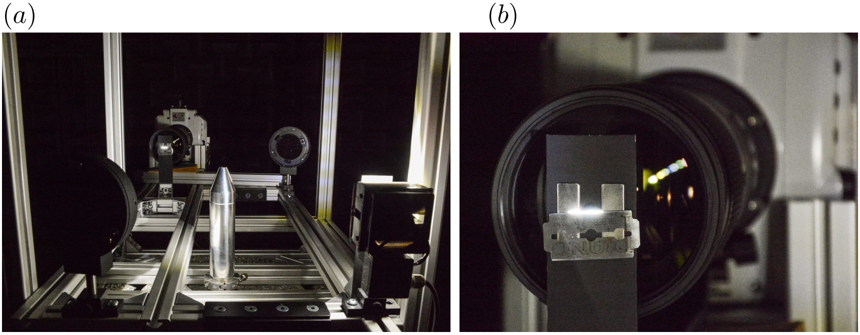

Figure 3.3: (*a*) General set-up for Schlieren photography. On the right side at the front, we can see the light source emitting light to the back, where the first parabolic mirror is located. In the first parabolic mirror, the light rays are parallelised and sent through the jet (in the centre of the image) until the second parabolic mirror (on the front left side of the image). There, the light is focused into the camera (in the rear right side of the image) and just before arriving at the camera a part of the light is blocked with a razor blade. (*b*) Razor blade at the focal point of the second parabolic mirror and the camera. Detail view.

Two different cameras were used in this work: a digital single-lens reflex (DSLR) Nikon D7100 with a video frame rate of 30 frames per second and a minimum exposure time of 125 μs and an ultrahigh-speed camera Phantom v2512, with a video frame rate of 10^6 frames per second and a minimum exposure time of 265 ns. While the DSLR was used to work with long exposures and record the mean value of the flow field, the ultrahigh-speed camera was used to track the supersonic structures in the starting jet.

Together with the cameras, we used mainly two different lenses: (*i*) a Nikon zoom lense 18-105mm f/3.5-5.6 VR and (*ii*) a tele-zoom Nikon AF-S 200-500mm f/5.6E ED VR. We used the zoom lense to visualise a region of about $5-7$ jet diameters, while the tele-zoom was used to focus in a very small region of about $1-2$ jet diameters. Figure 3.5 shows an example of both kinds of schlieren pictures.

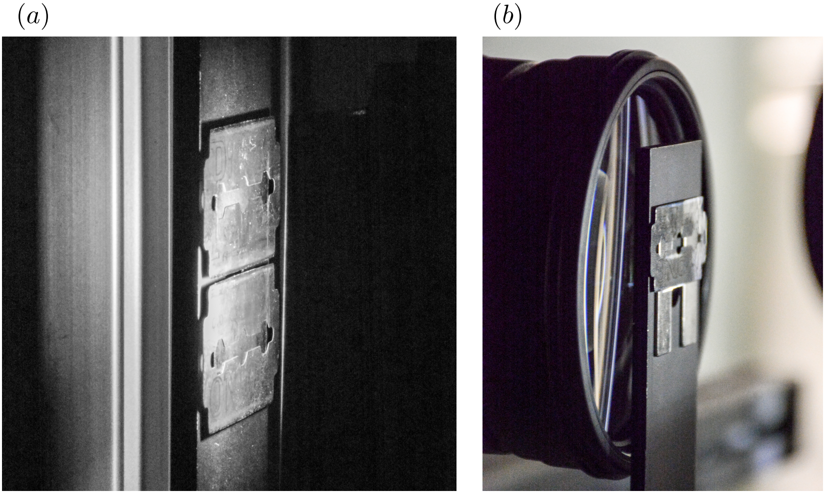

Figure 3.4: (*a*) Two razor blades at the light source to generate a slit source. (*b*) Razor blade at the front of the camera lense.

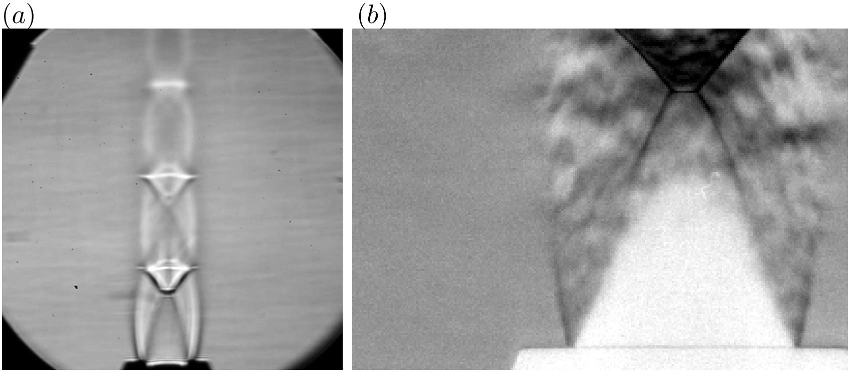

Figure 3.5: Schlieren examples. (*a*) Long exposure schlieren photography. The combination of DSLR with the zoom lense were used. (*b*) High-speed schlieren photography. The high speed camera with the tele-zoom were used.

3.2 Acoustic measurements in the laboratory

We performed acoustic measurements as well in the anechoic chamber of the Berlin Institute of Technology. With up to 16 microphones in different configurations, we measured the jet noise in the near and the far field. Both subsonic and supersonic jets were taken into consideration.

Figure 3.6 shows two different microphone arrangements in the jet near field.

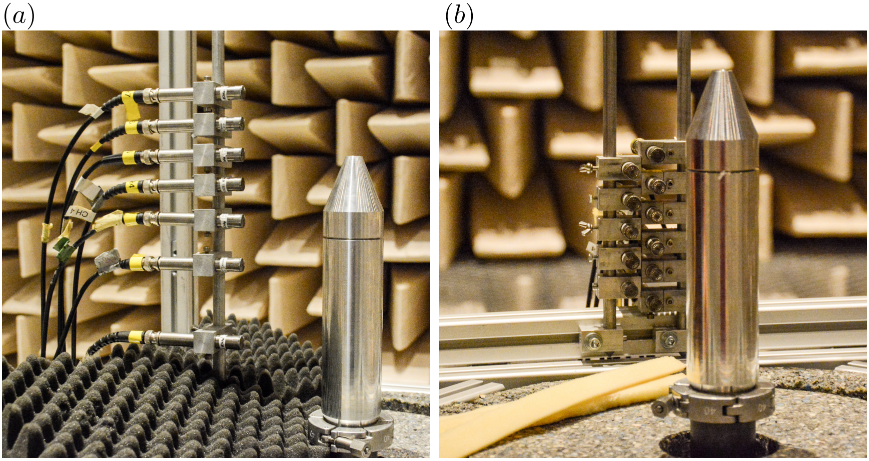

Figure 3.6: (a) Disposition of the microphones to measure the acoustics of the jet and its dependence with the jet angle. (b) Different set-up of the microphones focusing on the supersonic components of the jet noise.

The half-inch microphones used are manufactured by PCB with a frequency range of 3.75 – 20 000 Hz, the specifications of these microphones are included in section E.1. We used also an infrasound microphone manufactured by G.R.A.S. with a frequency range of 0.5 – 20 000 Hz, the specifications of these microphones are included in section E.1. They were controlled by a data acquisition system manufactured by Oros.

The air ejected from the nozzle was stored at 8 bars in a 3 m^3 deposit outside the anechoic chamber. A pressure regulator led us to perform experiments with intermediate pressures. The nozzle, made of aluminium, has an inner exit diameter of 10 mm. This choice was not optimal since the associated frequency of the supersonic jet noise components were partially outside the frequency range of the microphones, but for some set-ups, we were able to measure also the supersonic components.

3.3 Acoustic measurements at real volcanoes

In order to study as well a natural case, we did several expeditions to active volcanoes to analyse the noise radiated during an eruption as a natural example of a compressible starting jet. I was involved in two campaigns: Mount Etna in July 2014 and Stromboli in May 2016.

3.3.1 Mount Etna

A collaboration with the European project 'Mediterranean Supersite Volcanoes' (MED-SUV) gave us the possibility to attend a campaign in July 2014. There, prof. Sesterhenn and myself measured the acoustics of an eruptive fissure at the North-East Crater for several hours during three consecutive days. In total, we measured more than 11 000 events. Figure 3.7 shows the two craters of the eruptive fissure of the North-East Crater during the $15-16/07/2014$ expedition and figure 3.8 shows the deployment of the microphones on that expedition.

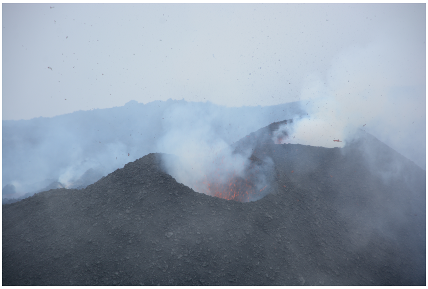

Figure 3.7: Craters of the eruptive fissure of the North-East Crater of mount Etna during the $15-16/07/2014$ expedition.

During this campaign, we deployed three microphones at different circumferential angles. We fixed aluminium rods on the ground and the microphones at the top of the rods. The microphones were connected to the data acquisition boxes with BNC cables.

The microphones were located covering a circumferential angle of about 120° around the craters of the eruptive fissure, although not at the same altitude, which was dependent on the orography of the volcano.

In order to show that even at very large Reynolds numbers is possible to observe a laminar vortex ring we show in figure 3.9 a vortex ring ejected by an eruption at Mount Etna.

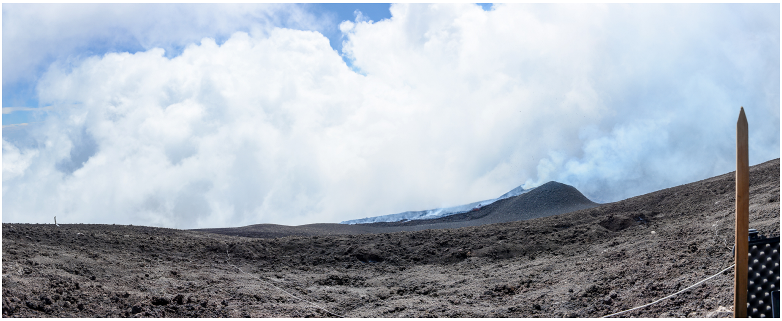

Figure 3.8: Deployment of the microphones around the craters at the field during the Mount Etna expedition.

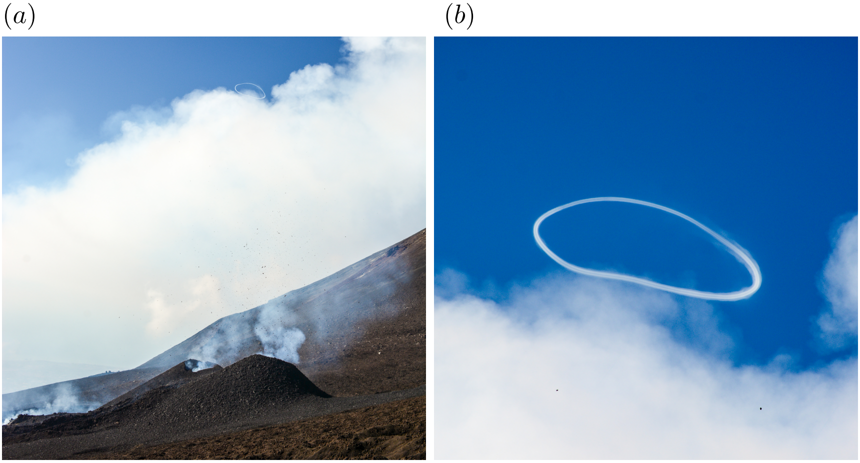

Figure 3.9: (*a*) Image taken at the eruptive fissure in the North-East crater at Mount Etna in 2015. The two craters are visible in the lower part of the image and ejected vortex ring in the upper part of the image. (*b*) Detail view of the vortex ring ejected by the same eruption.

3.3.2 Stromboli

A collaboration with the European project 'Volcanic ash: FiEld, expeRimenTal and numerIcal investiGations of prOcesses during its lifecycle' (VERTIGO) gave us the possibility to assist to the field campaign of May 2016 in Stromboli. Figure 3.10 shows a general overview of the crater configuration at Stromboli on the 31^{th} May 2016.

A group of up to four people (prof. Sesterhenn, Stefano Alois, Steffen Nitsch and myself) were 9 times in the summit of the volcano to perform

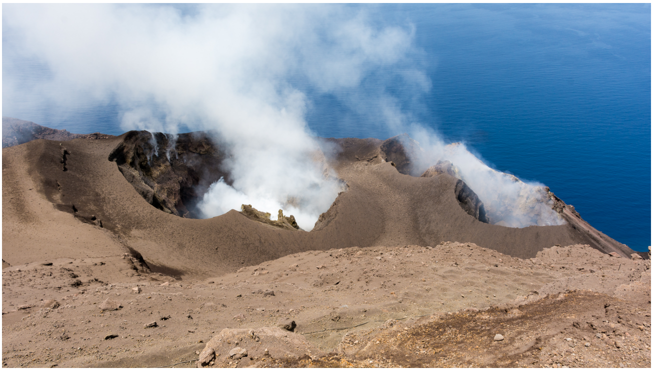

Figure 3.10: Crater configuration at Stromboli on the 31th May 2016.

acoustic measurements of the eruptions. Several hundreds of events were recorded during this campaign. Similar to the campaign at Mount Etna, we fixed aluminium rods on the ground and one microphone per rod, see figure 3.11. During this campaign, we had up to four completely independent stations, perfectly synchronised.

Depending on the day, the weather conditions and the plan of the rest of the campaign, we used only some of the stations, all located at the summit of the volcano, or we used all stations, locating them as well far away from the volcano, close to the sea level.

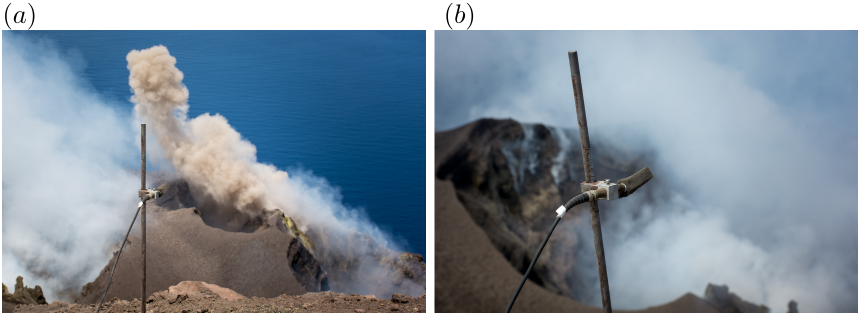

Figure 3.11: Measurements at Stromboli. In both figures the aluminum rod (fixed to the ground) can be seen. Attached to it are the microphones, which are connected to the computer through a BNC cable.

The stations were basically composed of a microphone, a data acquisition system manufactured by Data Translation, a NUC computer and an external power bank. While the data acquisition system, the NUC and the power bank were packed in a Peli case, the microphone was deployed in the field connected to the Peli case through a BNC cable.

The synchronisation of the independent stations took place in a very simple, but efficient way. When the different stations involved were about to be placed far away from each other, we started the measurements at the point when the stations were still together. We connected the microphones for a short period of time and we used an athletics starting flap to generate a sharp noise when holding all microphones at the same distance. The pressure wave should arrive at all microphones with a delay smaller than the sampling rate of the microphones, leading to enough accuracy in our measurements.

Part III

Results of jet simulations and experiments

Chapter 4

Characterisation of the compressible starting jet

In this chapter, we describe how is the evolution of the dynamics of the different features in the compressible starting jet. We proceed chronologically starting with the compression wave, following with the dynamics of the vortex ring and how the compressibility affects its dynamics and closing the chapter with the formation of the trailing jet and its dynamics.

4.1 Compression wave

When impulsively releasing the pressure of the reservoir, a compression wave is formed at the nozzle exit. It travels into the unbounded chamber with a half-spherical shape. For low pressure ratios, this compression wave is a pressure wave, that propagates at $M = 1$. For larger pressure ratios, a blast wave is created, which propagates at $M > 1$. Ishii et al. [1999] found by applying the RANKINE-HUGONIOT relations across a moving shock that the required pressure ratio for a blast wave is $p_{0r}/p_\infty = 41.2$. This is shown in figure 4.1*b*. The blue line represents the Mach number of an isentropic expansion from the reservoir to the region 2 represented in figure 4.1*a*. For a pressure ratio $p_{0r}/p_\infty = 4.1$ the Mach number in the region 2 becomes $M_2 = 1$. This condition remains for pressure ratios up to 41.2, represented by the red line in figure 4.1*b*. From $p_{0r}/p_\infty = 41.2$ on, the Mach number in region 2 becomes $M_2 > 1$ and the waves moves with supersonic speed.

4.2 Vortex ring dynamics

The characterisation of the vortex ring dynamics can be determined by the vortex ring radius and core radius and the axial position and velocity.

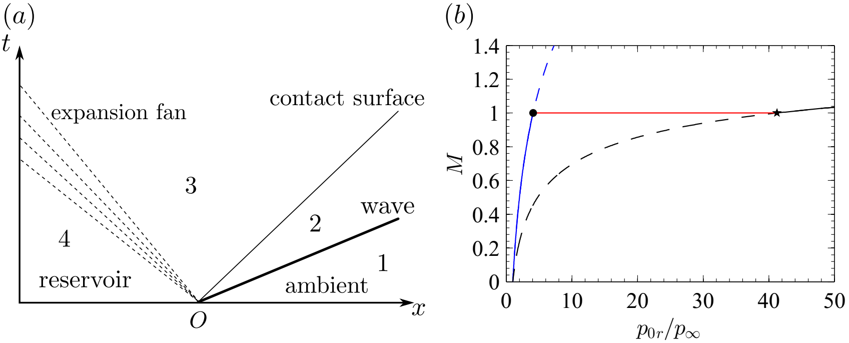

Figure 4.1: (*a*) Characteristic diagram of the classical shock tube problem. Region 1 is the ambient or the low-pressure region; 2 is the region between the first compression wave (it might be a pressure wave or a blast wave depending on the pressure ratio) and the contact surface (the region where the fluid coming from the reservoir and the corresponding to the ambient are in contact assuming no mass diffusivity); 3 denotes the region between the contact surface and the expansion fan and 4 denotes the reservoir region. (*b*) Involved Mach numbers in the region 2 of the shock tube problem. The real path is represented in solid lines; the dashed lines are for reference. The blue lines (dashed and solid) represents the Mach number of an isentropic expansion from the reservoir until the region 2 (represented in *a*). The black lines (dashed and solid) represents the Mach number behind a shock wave through the Rankine-Hugoniot equations until the region 2 (represented in *a*). The real evolution is the combination of the different solid lines, this is, a subsonic flow after the compression wave from $p_{0r}/p_\infty = 1$ to 4.1, sonic flow from $p_{0r}/p_\infty = 4.1$ to 41.2 and supersonic flow from $p_{0r}/p_\infty = 41.2$ on.

We discuss this features in the following sections.

To perform this analysis we used the results of the simulations 1.a, $2-6$ and 7.a, where the only free parameter was L/D, see table 2.6 in the introduction.

4.2.1 Vortex ring radius and core radius

The geometry of the vortex ring is fully defined with two parameters: the vortex ring radius (R_{VR}) and the vortex ring core radius δ_{90} as shown in figure 4.2.

We define the vortex ring radius ($R_{VR}(t^*)/D$) as the distance from the jet axis to the maximum distribution of I_R

$$I_R(R_{VR}, t) = \frac{1}{\overline{U}^2 D} \int_0^\infty u_R^2 dx, \tag{4.1}$$

taken from Pawlak et al. [2007]. The maximum of I_R is associated with the peak of radial flow coincident with the vortex centre. The vortex ring core radius ($\delta_{90}(t^*)/D$) is defined in this study as the radial distance from the vortex ring core for which the vorticity reaches the 10% of the maximum vorticity in the vortex ring.

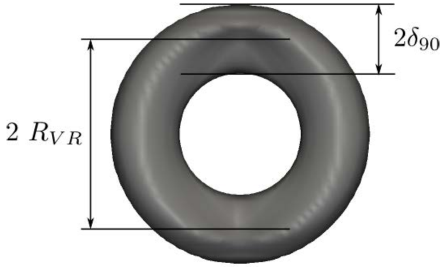

Figure 4.2: Geometrical parameters of the vortex ring: vortex ring radius (R_{VR}) and vortex ring core radius (δ_{90}).

Making the assumption that the impulse (I) of the vortex ring is constant, Maxworthy [1972] stated that $I \sim UR_{VR}^3$ and hence $R_{VR} \sim t^{1/3}$. The impulse of the vortex ring was defined in Maxworthy [1972] as $I = \pi R_{VR}^2 \Gamma$, where Γ is the circulation of the vortex ring.

For a time interval denoted as $(t^*)_{1/3\mathrm{law}}$ in table 4.1, starting at about $t^* = 2$, the vortex ring radius shows a dependence with $R_{VR}(t^*)/D \sim (t^*)^{1/3}$, as shown in figure 4.3.

Table 4.1: Vortex ring non-dimensional radius at the end of the formation stage. The $(t^*)^{1/3}$ law reads $R_{VR}/D = a_{1/3} + b_{1/3}(c_{1/3} + t^*)^{1/3}$, where the coefficients $a_{1/3}, b_{1/3}, c_{1/3}$ are here presented. Time interval for which the $(t^*)^{1/3}$ law is valid for the different cases under investigation.

Case	L/D	$\left(\frac{R_{VR}}{D}\right)_{\max}$	$a_{1/3}$	$b_{1/3}$	$c_{1/3}$	$(t^*)_{1/3\mathrm{law}}$
1.a	0.4473	0.5415	0.4578	0.0583	-1.8563	$[2-6]$
2	1.1730	0.6427	0.4837	0.0731	-2.5026	$[2-13.5]$
3	3.8029	0.8147	0.4380	0.1393	-2.3148	$[2.1-21.4]$
4	8.6047	0.8496	0.3413	0.2108	-1.9296	$[1.8-17.5]$
5	13.5487	0.8847	0.2813	0.2465	-1.5861	$[1.8-16.3]$
6	28.5899	0.9201	0.1519	0.3112	-0.7541	$[1.8-15.5]$
7.a	$\rightarrow \infty$	1.0280	0.0329	0.3684	-0.0435	$[1.8-16.3]$

Vortex rings generated with larger L/D grew faster and during a longer period of time than vortex rings generated with lower L/D. Figure 4.4a

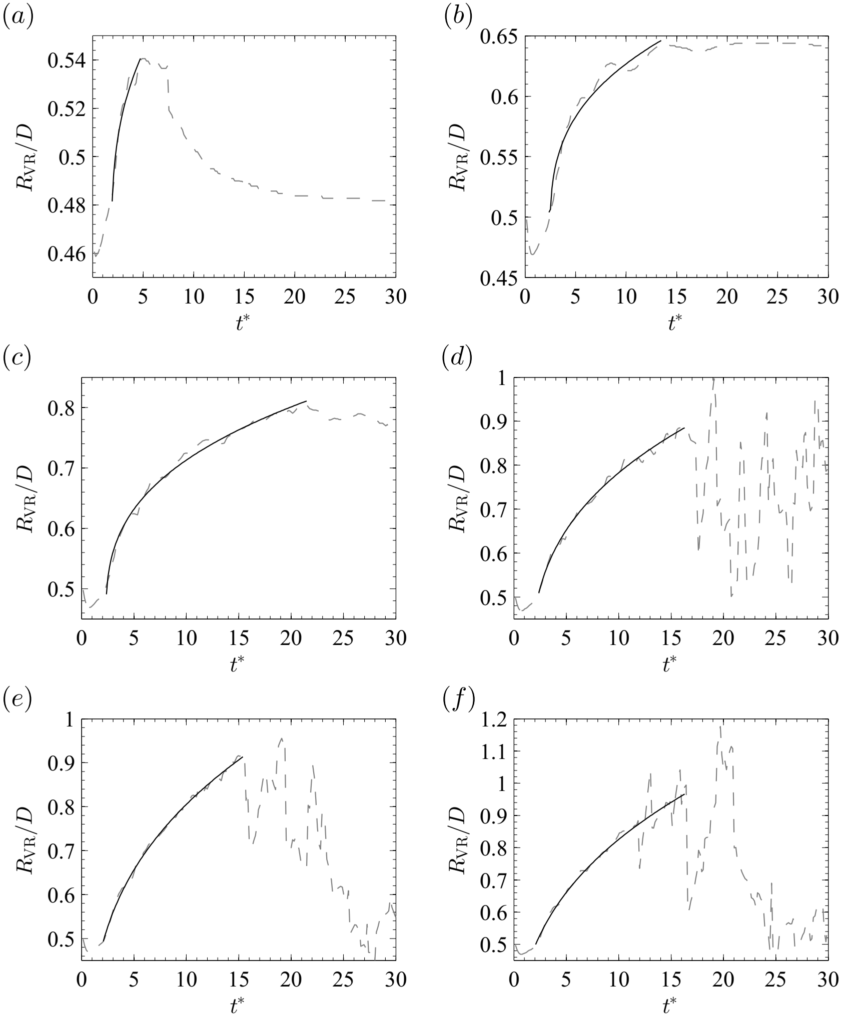

Figure 4.3: Evolution of the vortex ring non-dimensional radius. The dashed line corresponds to the instantaneous value, while the solid black line corresponds to the proportionality law given by the equation $R_{VR}/D = a_{1/3} + b_{1/3}(c_{1/3} + t^*)^{1/3}$. The parameters $a_{1/3}$, $b_{1/3}$ and $c_{1/3}$ are in table 4.1. (*a*) Case 1.*a*. $L/D = 0.4473$. (*b*) Case 2. $L/D = 1.1730$. (*c*) Case 3. $L/D = 3.8029$. (*d*) Case 5. $L/D = 13.5487$. (*e*) Case 6. $L/D = 28.5899$. (*f*) Case 7.*a*. $L/D \to \infty$.

compares the $R_{VR}(t^*)/D = a_{1/3}+b_{1/3}(c_{1/3}+t^*)^{1/3}$ trend lines for the cases in this study.

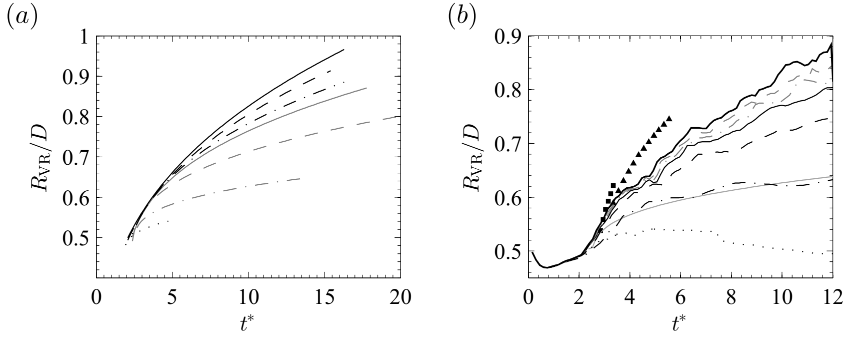

Figure 4.4: (*a*) $R_{VR}/D = a_{1/3} + b_{1/3}(c_{1/3} + t^*)^{1/3}$ trend lines that follow the different cases of this study. See legend in table 2.3. $a_{1/3}$, $b_{1/3}$ and $c_{1/3}$ are the ones in the captions of figure 4.3. (*b*) Comparison with the literature of the vortex ring radius' proportionality with $(t^*)^{1/3}$. See legend in table 2.3. ● Gao and Yu [2010], ■ Didden [1979], ▲ Liess [1978]. The data from Liess [1978] were shifted in time because of a presumed different time origin definition.

Although this proportionality is only found in the work of Maxworthy [1972], the behaviour of the vortex ring radius growth agrees with the compared previous works, see figure 4.4*b*. The time origin does not agree with all the previous works, presumably due to a different time origin definition based on the formation of the vortex ring and not on the beginning of the fluid flow.

During the formation of the vortex ring, its core radius shrank impulsively (the same way that the fluid was injected), but during the decay stage, the vortex ring core radius grows with a monotonously decreasing growth rate, figure 4.5*a*. In the very beginning, the vortex was not completely formed, and therefore very difficult to track. Because of this, the initial evolution of the vortex ring core radius is irregular.

To directly compare the growth of the vortex ring radius and the core radius, figure 4.5*b* shows the vorticity profile along the radial direction during the decay stage of the vortex ring.

4.2.2 Axial location and propagation velocity

We define the axial position of the vortex ring as the distance in the axial direction between the nozzle and the maximum of I_x

$$I_x(x,t) = \frac{1}{\overline{U}^2 D^2} \int_0^{nR} u^2 R dR, \tag{4.2}$$

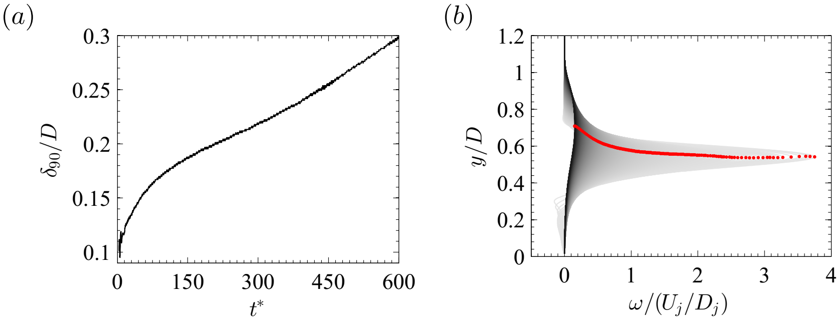

Figure 4.5: (a)Time evolution of δ_{90}/D. (b) Evolution of the vorticity profile along the radial direction. Light grey indicates former times, while dark grey indicates later times. ● maximum of every vorticity profile.

Pawlak et al. [2007]. I_x is proportional to the flux of axial momentum exiting throughout a disk of arbitrary radius (nR), perpendicular to the axial direction.

The axial location of the vortex ring was proportional to $x_{\mathrm{VR}}/D \sim (t^*)^{1/2}$, as proposed by Witze [1980] and shown in figure 4.6. The proportionality constants obtained by least squares in the linear range are in the captions and also summarised in table 4.2.

Table 4.2: The proportionality law reads $x_{VR}/D = a_{1/2}(t^*)^{1/2} + b_{1/2}$. The $a_{1/2}$ and $b_{1/2}$ coefficients are presented here, as well as the dimensionless time for what the proportionality starts.

Case	L/D	$a_{1/2}$	$b_{1/2}$	$(t^*)_{1/2\mathrm{law}}$
1	0.4473	0.8726	−4.0366	92.3310
2	1.1730	1.6633	−6.6136	53.1470
3	3.8029	2.8379	−10.0457	31.9937
4	8.6047	3.9509	−9.0353	12.5919
5	13.5487	3.1999	−9.3714	17.4783
6	28.5899	3.2337	−9.1065	14.9599
7.a	$\to \infty$	3.6724	−10.8790	15.9968

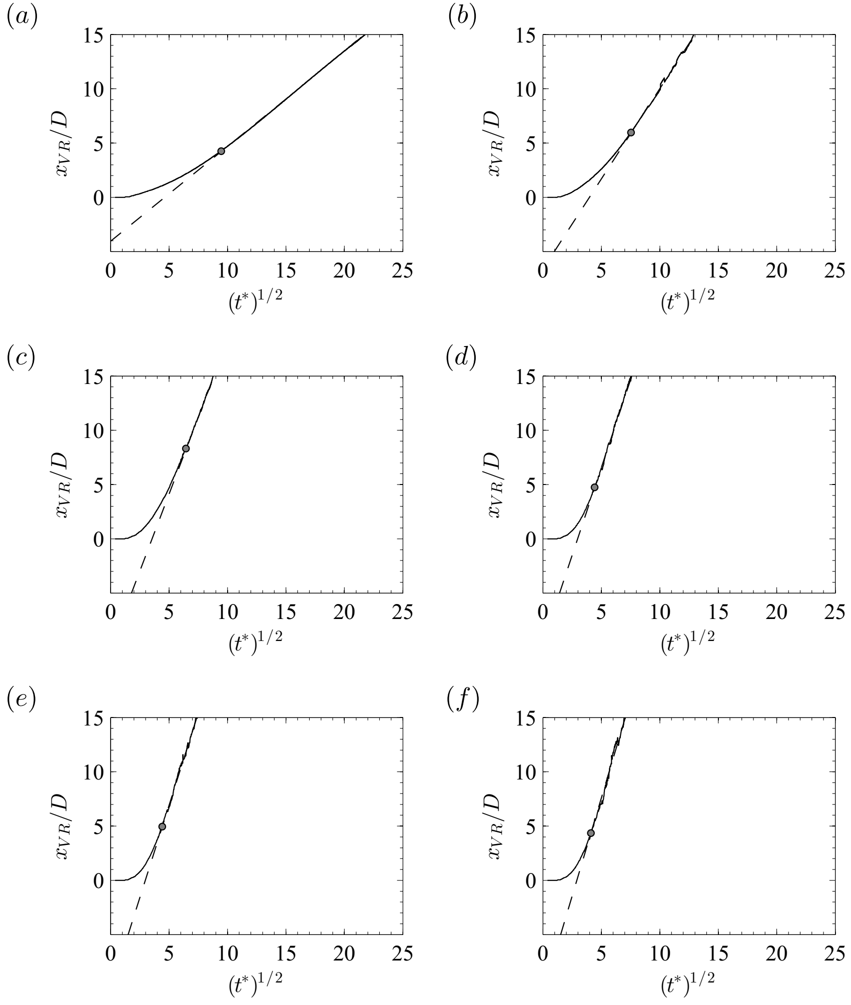

Figure 4.6: Evolution of the non-dimensional x-location of the vortex ring with $(t^*)^{1/2}$. The solid black lines are the instantaneous values from the simulations, while the dashed black lines correspond to the proportionality law given by $x_{VR}/D = a_{1/2}(t^*)^{1/2} + b_{1/2}$. The beginning of the proportionality is indicated with ●. (*a*) Case 1.*a*. $L/D = 0.45$. (*b*) Case 2. $L/D = 1.17$. (*c*) Case 3. $L/D = 3.80$. (*d*) Case 5. $L/D = 13.55$. (*e*) Case 6. $L/D = 28.59$. (*f*) Case 7.*a*. $L/D \to \infty$.

Another proportionality laws were found in the literature, like the results from Didden [1979] ($x_{\mathrm{VR}} \sim (t^*)^{3/2}$), which are not in contradiction with the results of this study because this study focuses on a later time interval, denoted as $(t^*)^{1/2}_{\mathrm{start}}$ in table 4.2. To the best knowledge of the authors, there is no mention in the literature about the time for which the $(t^*)^{1/2}$ proportionality starts. We define the beginning of the proportionality in this study as the non-dimensional time for which the $x-$location of the vortex ring and the $(t^*)^{1/2}$ proportionality differ in a 5%. We found that for larger values of C, this proportionality law starts earlier than for the cases with small C, see figure 4.6.

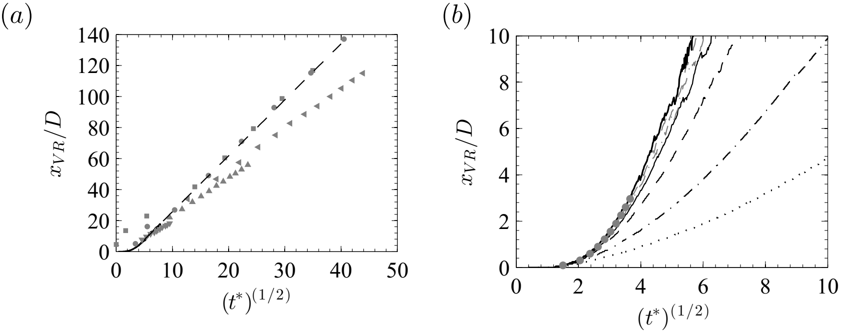

Figure 4.7: Evolution of the axial location of the vortex ring with the square root of the non-dimensional time. Comparison with experimental data. (*a*) Witze [1983] ● $Re \approx 1800$, ■ $Re \approx 4100$; Johari et al. [1997] ▼ $Re = 5000$, ▲ $Re = 15000$ and ◀ $Re = 20000$. The solid black line corresponds to case 7.*a* $Re = 5000$ and the dashed black line is its linear extrapolation. (*b*) ● Gao and Yu [2010] (shifted in time because of a presumed different time origin definition); see the legend in table 2.3.

When comparing with the literature, figures 4.7*a* and 4.7*b*, our data agreed well with the previous work except for the time origin, this is the reason why some data have been shifted in time. One exception of good agreement are the data from Witze [1983] for $Re \approx 4100$ in figure 4.7*a*; the vortex ring cannot be at a position of $x_{\mathrm{VR}}/D \approx 4.6$ at a time $\sqrt{t^*} \approx 0.008$, because it means that the vortex ring has travelled $4.6D$ in the time that the injected gas has reached only $0.008^2\ D$, and this would mean that the vortex ring moves with a velocity more than 70 000 times larger than the characteristic velocity with which the time was non-dimensionalised, and therefore the three first points of this data series (■) are not considered in the comparison. The rest of the data compared with agreed successfully with our data.

We now focus on the vortex ring propagation velocity. Based on the

Biot-Savart law for the velocity induced near a vortex, the Kelvin formula for the propagation velocity of a circular vortex ring of small cross section in a perfect fluid is

$$U = \frac{\Gamma}{4\pi R_{VR}} \log\left(\frac{8R_{VR}}{\delta_{90}} - 0.25\right), \tag{4.3}$$

taken from [Saffman, 1971].

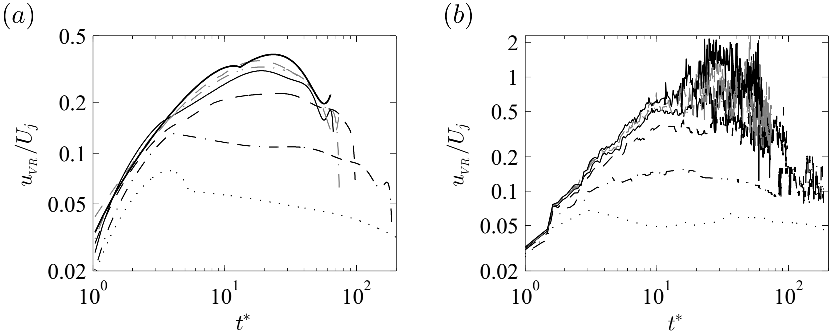

Figure 4.8: Vortex ring propagation velocity over the non-dimensional time for the different cases under study. See the legend in table 2.3. (*a*) Velocity derived from the tracking in the simulations. (*b*) Velocity feeding the model of Kelvin, equation (4.3) with the data $\Gamma(t^*)$, $R_{VR}(t^*)/D$ and $\delta_{90}(t^*)/D$ from the simulations.

Figure 4.8 shows a comparison between the vortex ring propagation velocity obtained deriving the vortex ring axial position with the time and the velocity obtained following Kelvin's formula (equation (4.3)) with the current values of $\Gamma(t^*)$, $R_{VR}(t^*)/D$ and $\delta_{90}(t^*)/D$ from the results of this study. The results are shown in figure 4.9 separated for the different cases. Generally, the results agree well, especially the laminar cases ($C = 1, 2$). For the cases with large values of C, the rising phase agrees well until the vortex rings become turbulent because they are very difficult to track and the assumptions made for the Kelvin model do not longer apply.

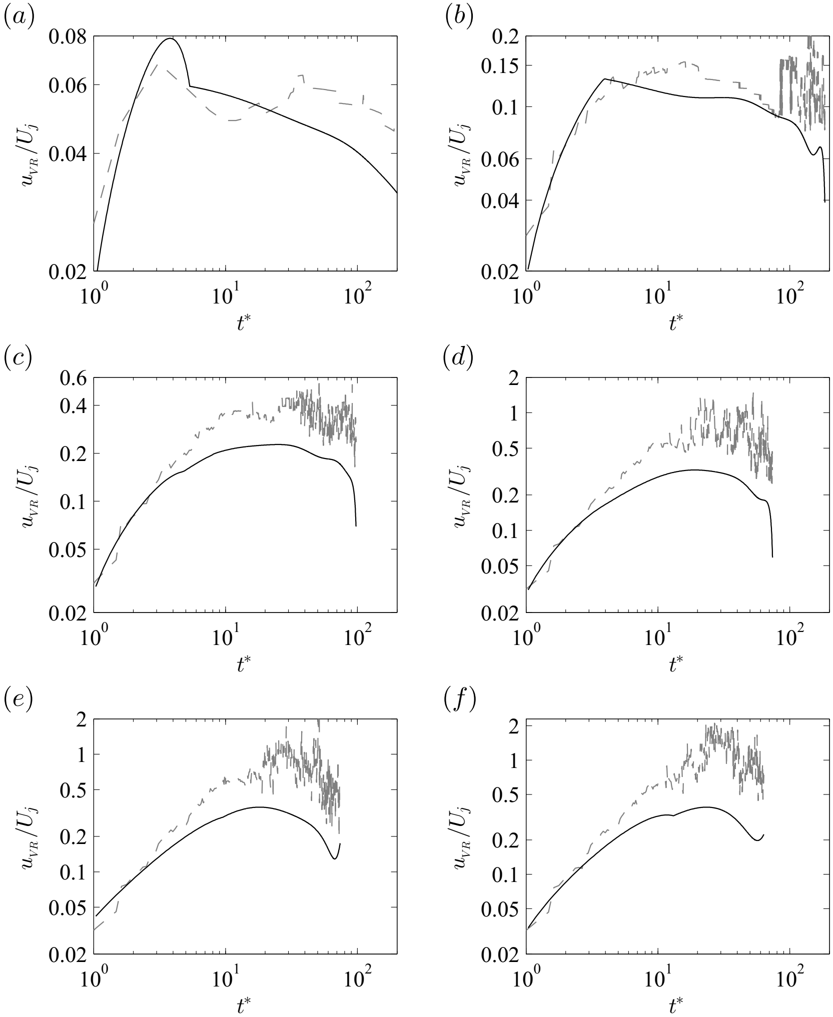

Figure 4.9: Vortex ring propagation velocity over the non-dimensional time for the different cases under study. The dashed grey line corresponds to the estimated velocity feeding Kelvin's formula (4.3) with the instantaneous value of $\Gamma(t^*)$, $R(t^*)/D$ and $\delta_{90}(t^*)/D$ from the simulations and the solid black line corresponds to the velocity directly derived from the tracking of the vortex ring in the simulations. (*a*) Case 1.*a*. (*b*) Case 2. (*c*) Case 3. (*d*) Case 5. (*e*) Case 6. (*f*) Case 7.*a*.

4.2.3 Effects of compressibility

Moore [1985] found that the propagation velocity of the vortex ring decreases due to compressibility effects, and it is given by:

$$U = \frac{\Gamma}{4\pi R_{VR}} \left[\log\left(\frac{8R_{VR}}{\delta_{90}}\right) - \frac{1}{4} - \frac{5}{12} M_\Gamma^2 + O(M_\Gamma^4) \right], \qquad (4.4)$$

where $M_\Gamma = \Gamma/(2\pi\delta_{90}c_\infty)$ is the Mach number based on the vortex circulation. This is mainly due to the reduction of the density in the core of the vortex ring, due to the pressure distribution. The contribution of compressibility is of the form:

$$\int_0^\infty \left(\frac{\rho(r)}{\rho(\infty)} - 1 \right) r dr$$

and it becomes negative because of the effect of compressibility.

We simulated a starting jet with a single vortex ring and without trailing jet in order to analyse the vortex ring. Three different configurations were studied (see figure 4.10$a - b$): a low compressible case (1.a), a high compressible case (1.b) and a supersonic case (1.c). The parameters of these simulations are summarised in table 4.3.

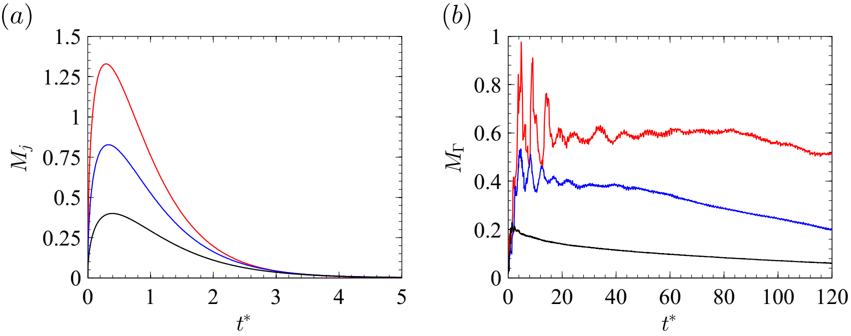

Figure 4.10: Evolution of the fully expanded Mach number (a) and the Mach number defined from the vortex ring circulation (M_Γ) (b) for the cases 1.a (black), 1.b (blue) and 1.c (red).

In order to estimate the propagation velocity of the vortex ring using Moore's formula, we computed the Mach number M_Γ, which are also summarised in table 4.3. The low compressible case (case 1.a) has a typical Mach number based on the circulation of $M_\Gamma = 0.1$, while for the compressible cases (high compressible 1.b and supersonic 1.c) we have $M_\Gamma \sim 0.4$ and

Table 4.3: Main parameters of the simulations focusing on the analysis of the vortex ring.

Case	L/D	p_{0r}/p_∞	$\max(M_j)$	M_Γ
1.a	0.45	3.6	0.4	0.1
1.b	0.0436	20.63	0.8267	0.4
1.c	0.091	96.36	1.329	0.6

0.6, respectively. As the theory predicts, the propagation velocity of cases 1.b and 1.c are lower than the corresponding of the case 1.a, as it can be inferred from the slope of the curves of figure 4.11a. The propagation velocity of the case 1.c is slightly lower than that of the case 1.b, although the Mach number M_Γ is substantially larger.

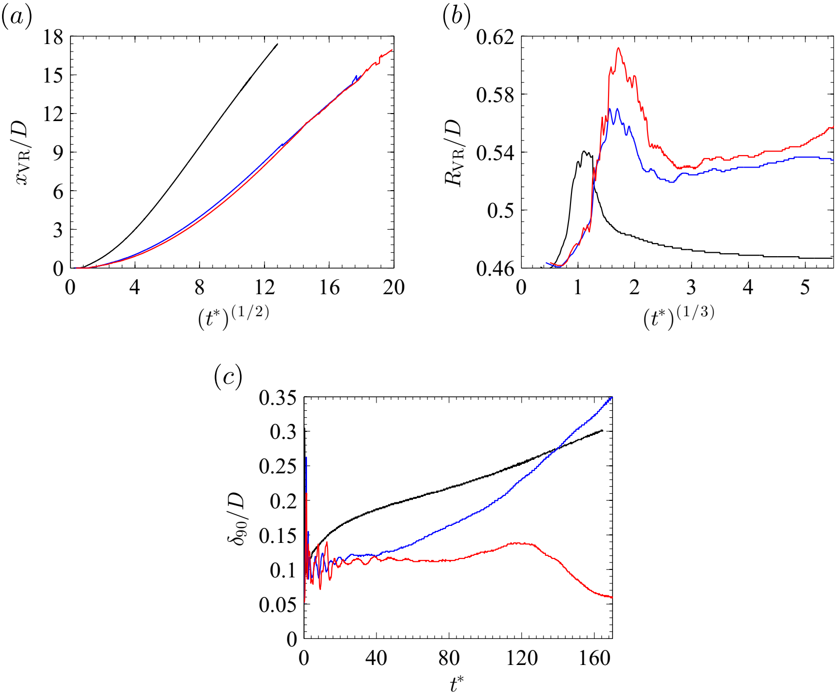

Figure 4.11: Evolution of the axial position (a), the vortex ring radius (b) and the vortex ring core radius (c) of the vortex ring for cases 1.a (black), 1.b (blue) and 1.c (red). The axial position has been plotted over $(t^*)^{(1/2)}$ to show its proportionality through the straight segments. The dimensionless radius has been plotted over $(t^*)^{1/3}$ to show its proportionality through the straight segments.

Figure 4.11*b* shows the evolution of the non-dimensional vortex ring radius R_{VR}/D with $(t^*)^{(1/3)}$. In the low compressible case, the vortex ring grows until a maximum $R_{\mathrm{VR}}/D \approx 0.54$ and then monotonically decreases. However, for both compressible cases, after the maximum non-dimensional radius, it does not decrease monotonically, but it has a local minimum and then grows slightly. The maximum is reached earlier for the low compressible case, followed by the high compressible and last the supersonic case.

Also related to the geometry of the vortex ring, the dimensionless core radius δ_{90}/D is shown for the three cases in figure 4.11*c*. Although the vortex rings were generated by the same nozzle diameter, there are substantial differences between the three cases.

4.3 Trailing jet formation and dynamics

The existence of a trailing jet after the vortex ring depends mainly on L/D as reported by Gharib et al. [1998], who termed *formation number* the limiting value of the non-dimensional mass supply that leads to a trailing jet $(L/D)_{\mathrm{lim}}$. Only the starting jets with a larger non-dimensional mass supply than the formation number $L/D > (L/D)_{\mathrm{lim}}$ lead to a trailing jet.

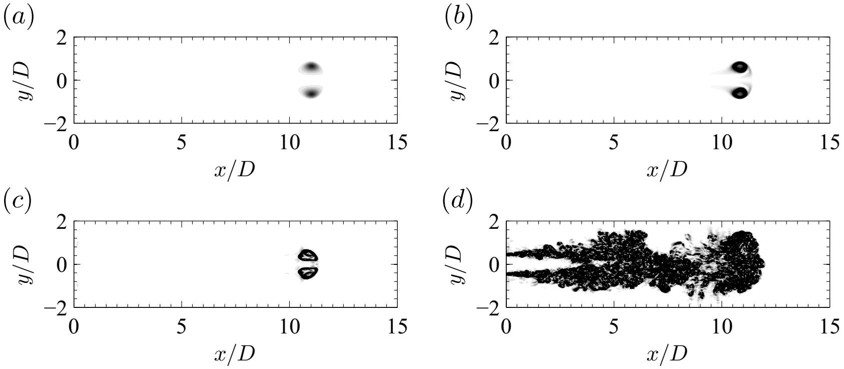

Figure 4.12: Vorticity contour when the vortex ring is at $x/D \sim 11$. $L/D = 0.45$, 0.0436 and 0.091 do not show any trailing jet but $L/D = 13.55$. The vorticity range is the same in all figures $[0, 200]\,\mathrm{s}^{-1}$. (*a*) Case 1.*a*. (*b*) Case 1.*b*. (*c*) Case 1.*c*. (*d*) Case 5.

The concept of the formation number also applies for compressible and supersonic flows. Figure 4.12 shows the vorticity contour for a low compressible (*a*), a high compressible (*b*) and a supersonic case (*c*) when the vortex ring reaches $x_{\mathrm{VR}}/D \sim 11$. All three cases have a lower non-dimensional mass supply than the formation number and therefore none of them has a trailing jet. The pressure ratio in all three cases is very different as summarised in table 4.3, showing in this way that the pressure ratio does not affect the existence of the trailing jet formation. Figure 4.10*a* shows the evolution of the fully expanded Mach number and figure 4.10*b* shows the evolution of the Mach number defined from the vortex ring circulation for the three cases for comparison. As an example of a supersonic starting jet that leads to a trailing jet we show the case 5 ($L/D = 13.5487$) in figure 4.12*d*.

Presumably, the limiting value of the non-dimensional mass supply that leads to a trailing jet in compressible started jets is the same than for the incompressible ones, but this is an open question that should be answered with experimental works rather than numerical ones due to the high computational costs to carry out such a parametric study.

Oscillations of the shock waves in the trailing jet have been reported in the literature for continuous jets [Panda, 1998]. These oscillations are visible for a starting jet without decay in figure 4.13*a*. The shock waves oscillate with respect to a fixed point. The larger the distance of the shock wave to the nozzle, the larger the amplitude of the oscillations. Figure 4.13*b* shows the oscillations of the shock waves for a case with decay. The shock waves further away from the nozzle oscillate with a larger amplitude than those close to the nozzle. This shock waves do not oscillate with respect to a fixed point; due to the decay stage, they move towards the nozzle exit and they oscillate additionally with respect to this movement.

In this chapter we analysed the dynamics of the three main features of the compressible starting jet: the compression wave propagates at the speed of sound for pressure ratios lower than 41.2, being a pressure wave; for larger pressure ratios the compression wave behave as a blast wave, propagating faster than the speed of sound.

We used the definition of the vortex ring radius based on the work of Pawlak et al. [2007]; we confirmed that for a time interval starting at about $t^* = 2$, the vortex ring radius shows a dependence with $R_{VR}/D \sim (t^*)^{1/3}$. We defined the core radius of the vortex ring as the radial distance from the vortex ring core for which the vorticity reaches 10% of the maximum vorticity in the vortex ring. Concerning the axial propagation of the vortex ring we confirmed the proportionality $x_{VR}/D \sim (t^*)^{1/2}$ as proposed by Witze [1980] and we reported the non-dimensional time for which this proportionality start. We also confirmed the effects of compressibility predicted by Moore [1985], reducing the axial propagation velocity of the vortex ring for higher compressible vortex rings.

Concerning the existence of the trailing jet, we believe that the limiting value of the non-dimensional mass supply that leads to a trailing jet in compressible started jets is very similar to the value in the incompressible

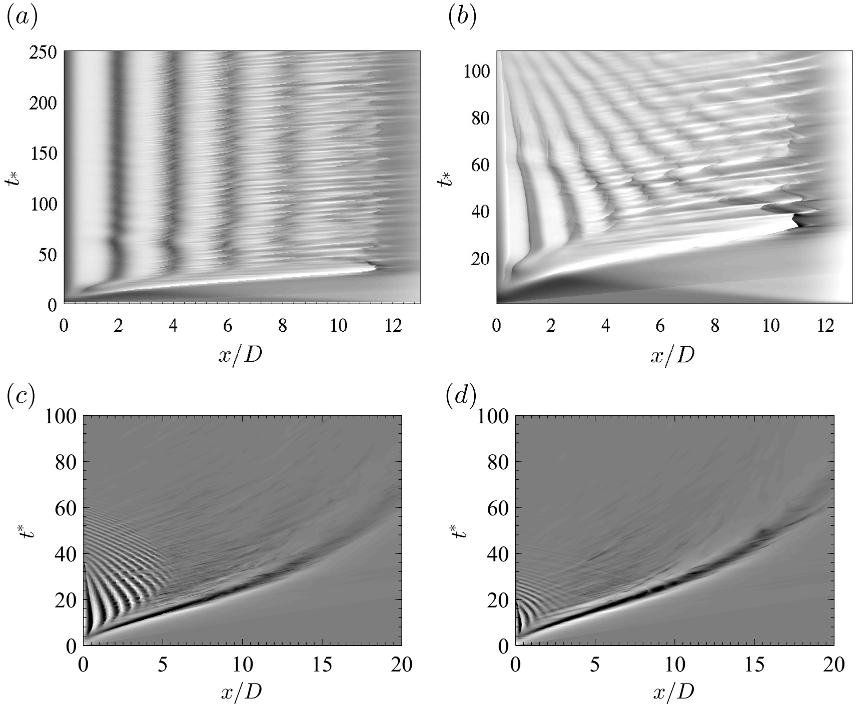

Figure 4.13: Characteristic ($x/D - t^*$) diagram of the pressure perturbations showing the dynamics of the shock waves. (*a*) Case 17. $p' \in \pm 40\ 000$ Pa. (*b*) Case 18. $p' \in \pm 40\ 000$ Pa. (*c*) Case 5. $p' \in \pm 25\ 000$ Pa. (*d*) Case 6. $p' \in \pm 37\ 000$Pa.

case. All simulations in this study regardless of their compressibility agreed with the criteria of the incompressible case.

We confirmed the oscillation of the shock waves of the trailing jet as reported by Panda [1998]. In the cases with decay, we showed how the shock waves move towards the nozzle exit and oscillate additionally with respect to this movement.

Chapter 5

Effects of the inflow condition

A part of the work corresponding to this section was presented in the ERCOFTAC Workshop 9th Direct and Large-Eddy Simulation (DLES9), [**J.J. Peña Fernández** et al., 2013].

This section assesses the influence of the inflow condition on the flow field and the emanated noise in the supersonic jet, comparing the jet flow for three different configurations:

- **Laminar** hyperbolic tangent velocity profile.
- Laminar hyperbolic tangent mean velocity profile perturbed synthetically with a tripped boundary layer (**TBL**) as in Bogey et al. [2011, 2012].
- Laminar compressible Blasius velocity profile with a **nozzle** using the volume penalisation method.

5.1 Laminar inflow

The inflow was modelled imposing a hyperbolic tangent profile corresponding to equation (2.10) and figure 2.6*b*. This is the classical inflow condition in the jet literature when not simulating the nozzle, see Freund et al. [2000] and Bogey et al. [2003]. The main advantage of this method is a very good control over the velocity gradients in the shear layer to produce a turbulent flow few diameters away from the inlet when used in combination with a Reynolds number in the range 5 000 – 10 000, as in this study.

5.2 Tripped boundary layer synthetic turbulence

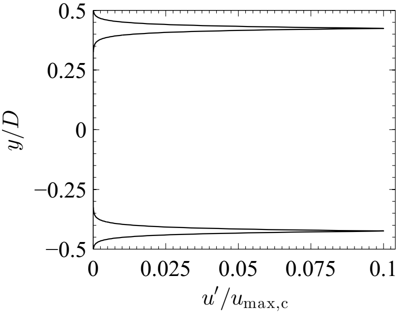

Figure 5.1: Velocity perturbations imposed at the inflow for the TBL case.

The hyperbolic tangent laminar base flow was distorted by superposing a typical turbulence profile from a shear layer as in Bogey et al. [2011, 2012]. In this case, we generate a synthetic turbulent inflow that leads to a fully turbulent flow few diameters away from the inlet. The perturbations have a peak of turbulence intensity of 10%. Figure 5.1 shows the spatial distribution of the velocity perturbations.

5.3 Nozzle flow

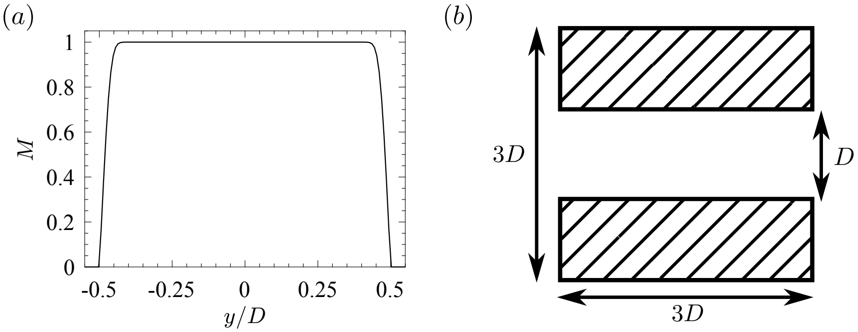

Figure 5.2: (*a*) Compressible Blasius Mach number inlet profile. (*b*) Sketch of the straight nozzle used in case 8.

A compressible Blasius boundary layer profile (figure 5.2*a*) was imposed in combination with a straight nozzle. The nozzle was implemented with the volume penalisation method as in section 2.6. A sketch of this nozzle is shown in figure 5.2*b*.

In the inner side of the nozzle, a turbulent boundary layer is generated due to the non-slip condition. This boundary layer flow generates some instabilities, leading to a flow at the nozzle exit with an intermediate level of turbulence, see Schulze [2011].

5.4 Effects on the flow field

Figure 5.3 shows the instantaneous Mach number contours for the laminar, TBL and nozzle cases, respectively. This figure draws a general picture of the three cases.

In the laminar case (figure 5.3*a*), 6 shock cells are easy to identify from the inflow until approximately $x/D = 8$. Downwards, the turbulence growing in the shear layer destroys the shock cell structure and the jet becomes subsonic and fully turbulent.

In the TBL case (figure 5.3*b*), the flow field is very similar to the previous case; the shock cells can be as well identified and then the jet becomes turbulent and subsonic. When looking in detail, we can see some small perturbations in the jet core as opposed to the previous case.

In the nozzle case (figure 5.3*c*), the flow field after the nozzle is also similar to both previous cases, but in which a faster growing of the shear layer can be identified. The jet core is shorter, the shock cells are slightly smaller and the jet becomes turbulent and subsonic for approximately $x/D = 10$.

We are especially interested in how different inlet conditions modify the shear layer and the shock cell structure of the jet. Figure 5.4 shows the instantaneous and r.m.s. entropy contours for the laminar, TBL and nozzle cases, respectively, giving an idea of how this mixing process takes place.

In the laminar case (figure 5.4*a*), the jet core can be identified as a dark region after the nozzle exit. From approximately $x/D = 8$ on, the combination of entrainment and turbulence enhance the mixing process and the shock cell structure disappears.

In the TBL case (figure 5.4*b*), from the nozzle exit, the synthetic turbulence imposed at the inlet can be clearly identified as dark and light spots all through the jet core. This does not modify massively the supersonic structure of the jet, which can be still identified until $x/D \sim 8$.

In the nozzle case (figure 5.4*c*), some perturbations can be seen inside the nozzle close to the wall. After the nozzle exit, the structure is very similar to that of the laminar case, with a clear jet core, which vanishes after $x/D = 10$ due to entrainment and turbulent mixing.

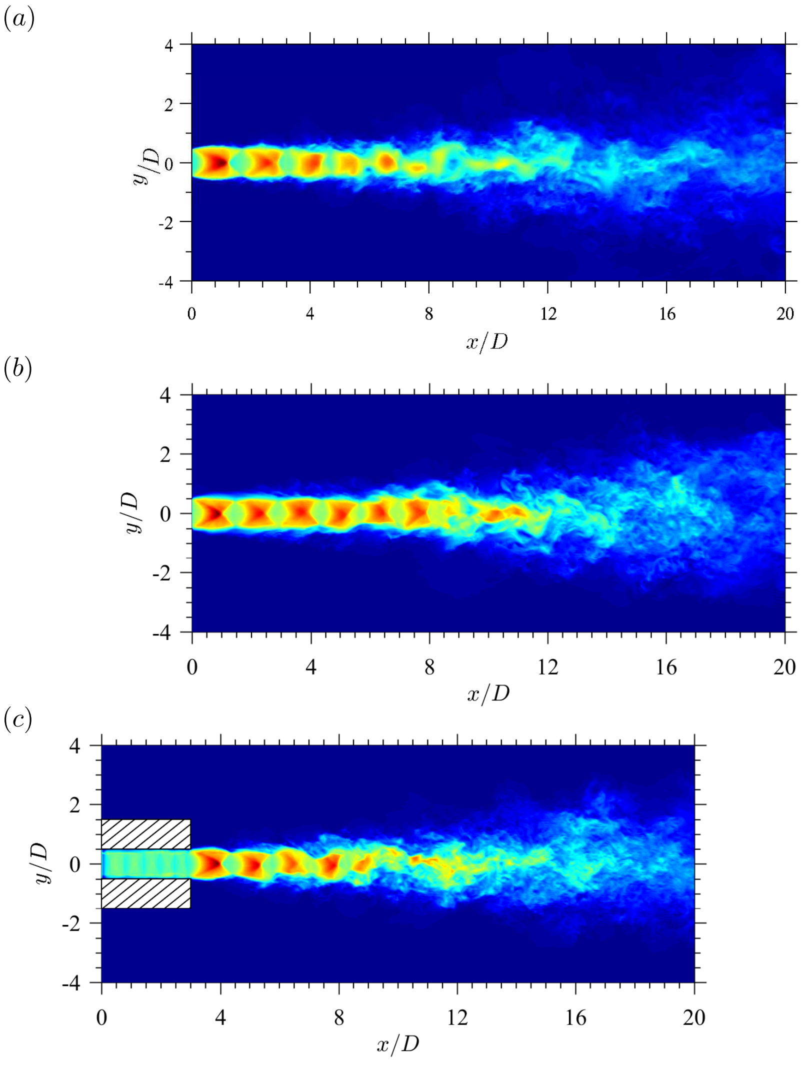

Figure 5.3: Instantaneous Mach number contours. (*a*) Laminar inflow (case 10). $M \in [0, 2.64]$. (*b*) TBL inflow (case 9). $M \in [0, 2.3]$. (*c*) nozzle inflow (case 8). $M \in [0, 2.45]$.

We focus now on the jet axis. Figure 5.5*a* shows the mean Mach number along with the jet axis, where the length of the shock cell region is clearly visible where the Mach number oscillates due to the shock waves. After this region, there is subsonic turbulent flow and the Mach number decreases

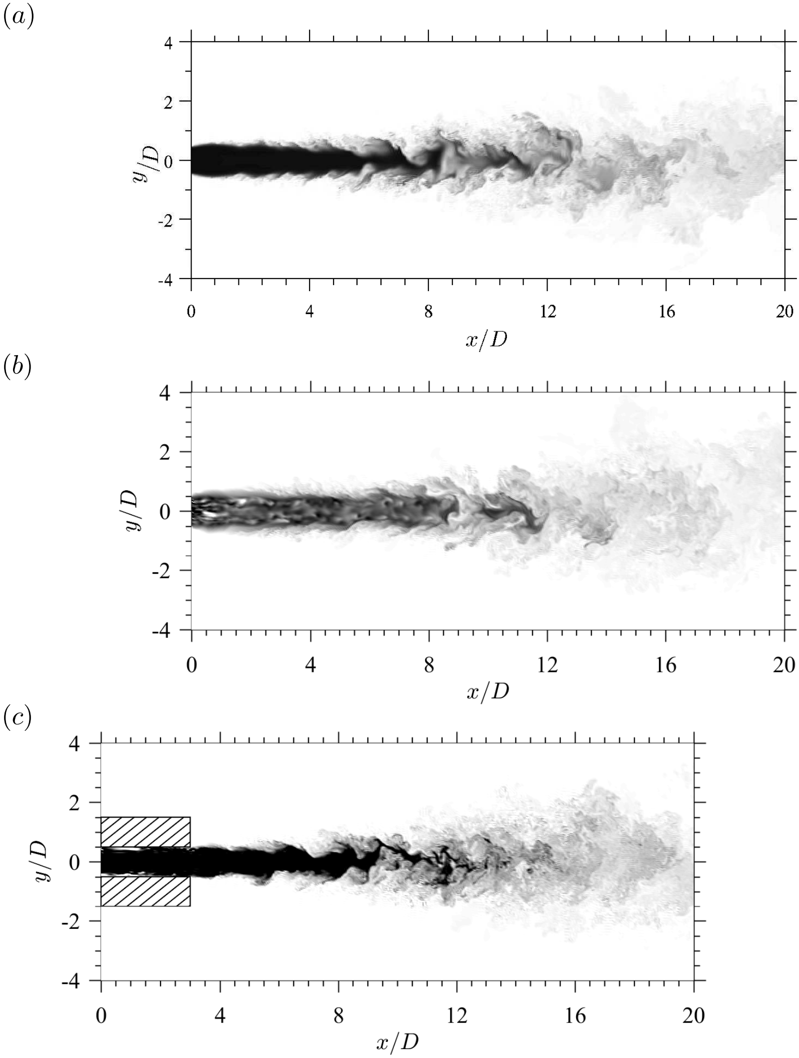

Figure 5.4: Instantaneous entropy contours. (*a*) Laminar inflow (case 10); $s \in [7885, 8110]\ m^2K^{-1}s^{-2}$. (*b*) TBL inflow (case 9); $s \in [7885, 8110]\ m^2K^{-1}s^{-2}$. (*c*) nozzle inflow (case 8); $s \in [8110, 8458]\ m^2K^{-1}s^{-2}$.

monotonically. In this figure is also clear that the shock cells in the nozzle case are slightly smaller than in the laminar case.

The r.m.s. entropy perturbations along the jet axis are represented in figure 5.5*b*. They show how in the laminar and nozzle cases, the entropy does not change in the first few diameters. This region corresponds to the potential core. The end of the potential core can be defined as the point in which the perturbations growing in the shear layer reach the centerline. This happens at $x/D \sim 4$ for the nozzle case, while for the laminar case it takes place at $x/D \sim 5.6$. The growth of the shear layer in the nozzle case is very similar as in the laminar case, but the nozzle case shows a shorter potential core than the laminar case as expected due to the turbulence generated in the nozzle.

The perturbations synthetically introduced in the TBL case decay for the first diameter, then it reaches a local minimum for around $x/D = 5$ and then it shows the same behaviour as the other two cases, with a local maximum for around $x/D \sim 10$.

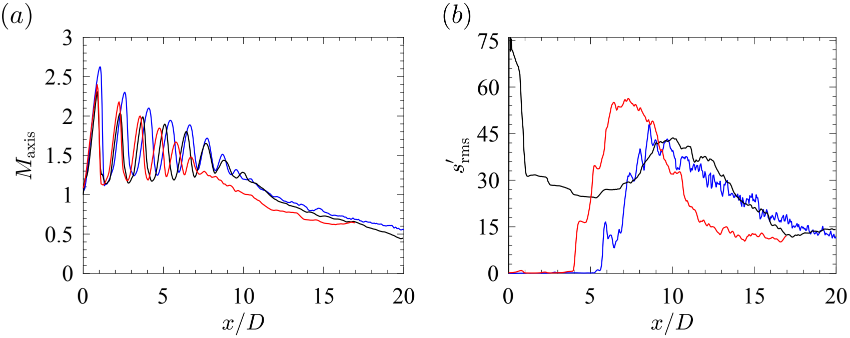

Figure 5.5: Distributions of mean Mach number (a) and r.m.s. values of the entropy perturbations (b) along the jet axis. The blue line represents the laminar inflow, the black line corresponds to the TBL case and the red line to the nozzle one.

In this section we summarised the flow field changes produced by the nozzle or TBL inlet conditions. As a general trend, for these turbulence intensities, the supersonic shock structure remains although the presence of strong perturbations. Looking at the r.m.s. values of the entropy along the jet axis, we see how the perturbations decay from the inlet until $x/D \sim 5$, where the perturbations from the shear layer start to play a role.

5.5 Effects on the radiated acoustics

Since all three cases have the same configuration (continuous supersonic jet), we expect the same general behaviour with slightly changes in the position and the contribution of the noise sources depending on the interaction of the turbulence with the quasi-periodic supersonic shock-cell structure.

For all three cases, the typical supersonic noise components were observed: turbulent mixing noise (TMN) and broadband shock noise (BBSN).

Figure 5.6 shows the sound pressure level spectra measured at a radial distance of $5D$ and an angle of 90°. Concerning the broadband shock noise, all three spectra agree in the largest part of the frequency interval. The Strouhal number for the maximum amplitude of broadband shock noise is slightly lower than those of the TBL and laminar cases. The development of the flow inside the nozzle, specially the boundary layer and the weak shocks inside the nozzle flow are possibly the reason for this different behaviour.

A much more evident difference concerns the turbulent mixing noise. The frequency content associated purely to turbulent mixing noise is much quieter in the case of laminar inlet than the cases TBL and nozzle. As expected, the TBL case has the loudest level over the whole frequency interval associated to turbulent mixing noise. The addition of synthetic turbulence to the inlet modify the turbulent mixing noise component over its whole frequency range.

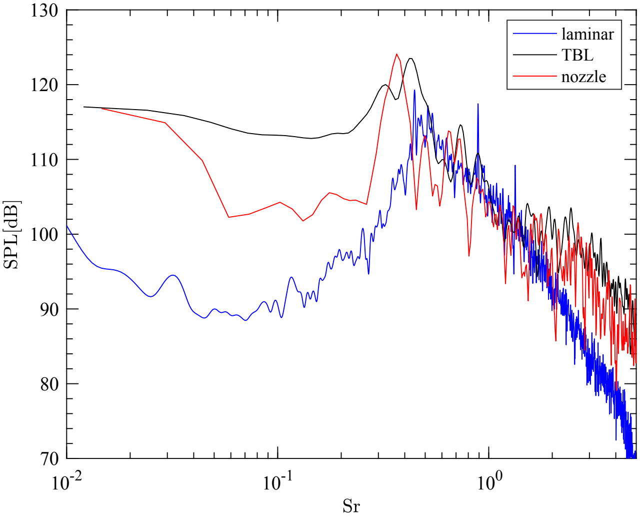

Figure 5.6: Sound pressure level spectra at 90°. The laminar case is represented in blue, the Tripped boundary layer in black and the nozzle case in red. The non-dimensional time interval analysed is $t^* \in [30, 150]$.

The sound pressure spectra give us many information about the individual noise components, but there is no time localisation of the components. For this purpose we performed a wavelet analysis: taking as the basis the complex Morlet wavelet we transformed the same time series to analyse them in the time-frequency domain.

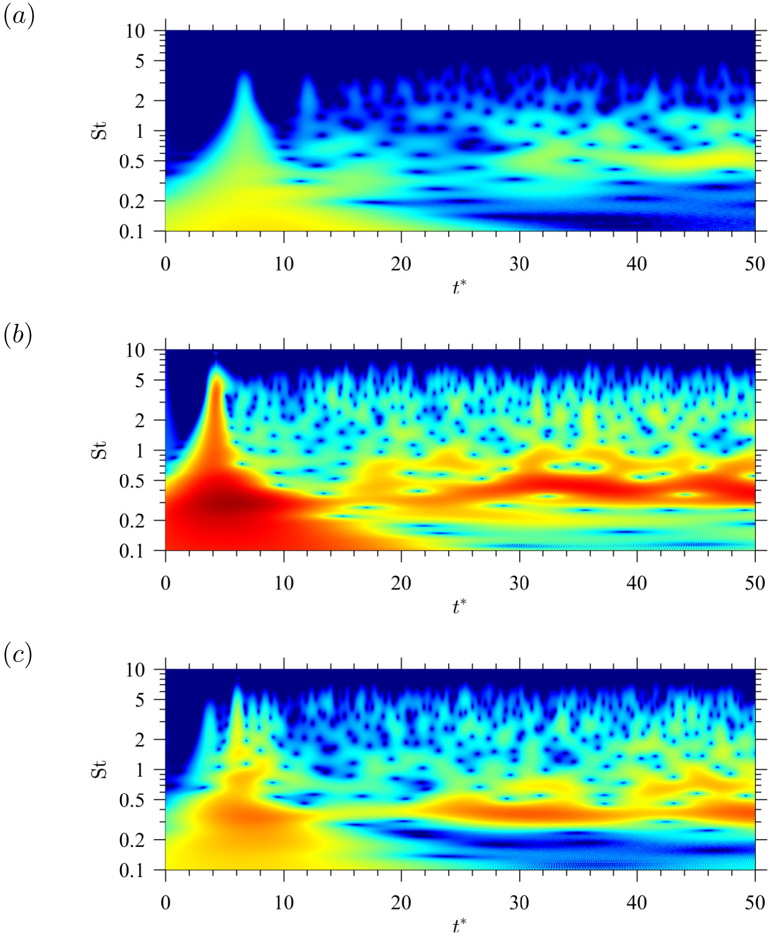

Figure 5.7: Continuous wavelet transformation coefficients in logarithmic colour scale for a signal measured at 90°. (*a*) Laminar inlet. (*b*) TBL inlet. (*c*) Nozzle inlet.

Figure 5.7 shows the wavelet coefficients of the three cases for a signal measured at 90°. In all three cases we can see the trace of the first compression wave at the beginning of the process. After this, the typical noise sources of the supersonic continuous jet are present in all three cases, but with some differences.

For the case with a laminar inflow, figure 5.7*a*, the sound pressure level does not reach the maximum of the scale. All components can be identified, but specially the turbulent mixing noise has a very low amplitude.

The case with the TBL inlet, figure 5.7*b*, has generally larger amplitudes than the previous case. The first compression wave has a larger amplitude than in the previous case, but more important is the dominant component of the broadband shock noise for $St \sim 3$: the Strouhal number is not constant with time, but it oscillates with time; this explains the double peak in figure 5.6. The high-frequency component reaches a higher Strouhal number than in the previous case. In the turbulent mixing noise frequency range, much larger amplitudes than in the previous case are found.

The case with a nozzle inlet, figure 5.7*c*, shows an intermediate behaviour. The amplitudes are between the two previous cases, with a higher level of turbulent mixing noise than the laminar case, but not as high as the TBL case. We can see the effects on the jet turbulent mixing noise when generating an intermediate level of turbulence at the inlet.

In this section we have seen how by increasing the turbulence intensity at the inlet, we increase the amplitude of the turbulent mixing noise component. A side effect is the modification of the broadband shock noise due to a different interaction between the shear layer and the shock waves, which results in a modification of the broadband shock noise, as can be seen in figure 5.6 with a double maximum for the broadband shock noise for the TBL case.

5.6 Effect of the nozzle geometry on the starting jet

The laminar inflow of the previous section was used in combination with a straight nozzle and two divergent nozzles modelled according to the volume penalisation method described in section 2.6. All three nozzles have a length of one diameter (D). The straight nozzle corresponds to the cases $11.a-h$, it is defined by ($A_e/A^* = 1$) and it is shown in figure 5.8*a*. The slightly divergent nozzle is defined by ($A_e/A^* = 2.36$), it corresponds to cases $12.a-h$ and it is shown in figure 5.8*b*. The divergent nozzle is defined by ($A_e/A^* = 4$), it corresponds to cases $13.a-h$ and it is shown in figure 5.8*c*.

Table 5.1 summarises the design parameters of the nozzles used in cases $11-13$. Assuming one-dimensional isentropic flow, the exit to critical area ratio defines the three points that define the working regimes of the nozzle. This is explained in detail in Appendix A for the interested reader. The maximum exit Mach number when working isentropically in the subsonic regime is denoted by M_e^- and it defines the boundary between subsonic

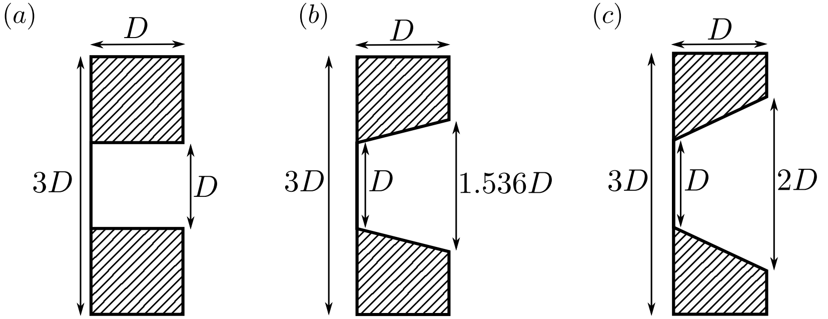

Figure 5.8: (a) Straight nozzle used in cases $11.a-h$, $A_e/A^*=1$. (b) Slightly divergent nozzle used in cases $12.a-h$, $A_e/A^*=2.36$. (c) Divergent nozzle used in cases $13.a-h$, $A_e/A^*=4$. The shaded area represents the wall of the nozzles.

flow in the whole nozzle and locally supersonic flow (just after the critical area). The same way, the exit Mach number when working isentropically in the supersonic regime is indicated with M_e^+; for lower Mach numbers the flow is overexpanded and for larger values, the flow is under-expanded. For this conditions, the flow is said to be *adapted*. Additionally, the exit Mach number when a normal shock wave is located exactly at the nozzle exit is denoted by M_2^+ and this conditions sets the boundary between the exit subsonic flow and the over-expanded flow.

Table 5.1: Nozzle design parameters for the cases $11.a-13.h$. The exit to critical area ratio is denoted by (A_e/A^*), the nozzle subsonic and supersonic design Mach number are indicated by M_e^- and M_e^+, respectively and the required pressure ratio to work under the subsonic and supersonic design conditions by (p_{0r}/p_e^-) and (p_{0r}/p_e^+), respectively. More information in appendix A.

Case	$\frac{A_e}{A^*}$	M_e^-	$\left(\frac{p_{0r}}{p_e^-}\right)$	M_e^+	$\left(\frac{p_{0r}}{p_e^+}\right)$	M_2^+	$\left(\frac{p_{0r}}{p_2^+}\right)$
11	1	1	1.893	1	1.893	1	1.893
12	2.36	0.255	1.046	2.38	14.1617	0.53	2.2
13	4	0.15	1.015	2.94	33.5717	0.48	3.38

All these limiting points collapse for the straight-convergent nozzle, this is, for $A_e/A^*=1$. Therefore, the straight nozzle of case 11 has a design exit Mach number of 1 when working with a pressure ratio of $(p_{0r}/p_\infty)_d = 1.893$ and it leads to sonic isentropic flow. For lower pressure ratios the nozzle has isentropic subsonic flow and for larger pressure ratios the nozzle works isentropically until its exit plane, leading to a supersonic expansion just after. This leads to a shock-cell structure as already seen.

For case 12 a divergent nozzle with $A_e/A^*=2.36$ was used. The maximum exit Mach number within the isentropic subsonic flow is $M_e^- = 0.255$, reaching this condition with a pressure ratio of $(p_{0r}/p_e^-) = 1.046$. This nozzle, when working with a pressure ratio between the previous one and $(p_{0r}/p_2^+) = 2.2$, will contain normal shock waves in the divergent part of the nozzle (stronger shock waves and located closer to the exit as the pressure ratio increases), increasing the Mach number until $M_2^+ = 0.53$ for the last condition. From this point on, the exit flow is supersonic overexpanded until the nozzle works at the isentropic supersonic conditions, this is, for a pressure ratio of $(p_{0r}/p_e^+) = 14.162$, leading to a Mach number of $M_e^+ = 2.38$. For larger pressure ratios, the configuration is the same, but the flow after the exit plane is underexpanded and must through a supersonic expansion (Prandtl-Meyer) further expanded.

For case 13 a divergent nozzle with $A_e/A^* = 4$ was used. When working within the isentropic subsonic regime, the maximum exit Mach number is $M_e^- = 0.15$ when applying a pressure ratio of $(p_{0r}/p_e^-) = 1.015$. This nozzle will contain normal shocks inside it when working with pressure ratios between the previous one and $(p_{0r}/p_2^+) = 3.38$, but the exit will remain subsonic. For larger pressure ratios the nozzle will be over-expanded until the supersonic isentropic flow, given by $(p_{0r}/p_e^+) = 33.5717$. For larger pressure ratios, the nozzle will be under-expanded and a supersonic expansion will take place in the vicinity of the nozzle exit.

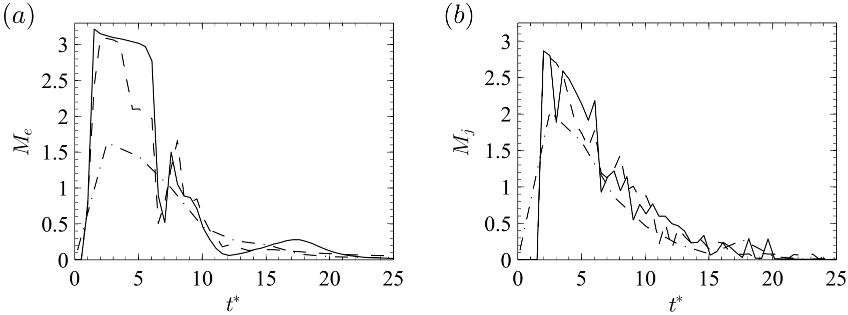

Figure 5.9: Temporal evolution of the exit (left) and fully expanded (right) Mach number. $(a-b)$ Effect of the geometry. $p_{0r}/p_\infty = 50$, $L/D = 2$. Dot-dashed: straight nozzle ($A/A^* = 1$), dashed: $A/A^* = 2.36$, solid: $A/A^* = 4$.

Figures 5.9$a-b$ show the effect of the nozzle geometry on the exit and fully expanded Mach number. Operating with a pressure ratio of $p_{0r}/p_\infty = 50$ and a non-dimensional mass supply of $L/D = 2$ we see the changes when having a straight nozzle ($A/A^* = 1$) or a divergent one $A/A^* = 2.36$ and $A/A^* = 4$. For an early time (serve as an example $t^* \sim 3$), the pressure ratio is still large (close to the original value of $p_{0r}/p_\infty = 50$) and therefore both convergent-divergent nozzles deliver supersonic flow, while the straight nozzle delivers sonic flow. For a later time ($t^* \sim 7$), both convergent-divergent nozzles deliver subsonic flow, because they operate already in the over-pressured regime, while the straight nozzle still operates in the under-pressured regime, being its exit Mach number still sonic. For later times, as a result of the pressure decay, the shock-cell spacing becomes shorter and all shocks travel towards the nozzle exit. Some of the shocks enter the nozzle exit. This process leads to the exit Mach number perturbation of figure 5.9*a* for $t^* \sim 8$.

The fully expanded Mach number, represented in figure 5.9*b*, does not depend on the geometry, and should have therefore the same value for all three geometries. Apart from the first stage, where the Flow is evolving inside the nozzle and therefore we cannot define the fully expanded conditions, we can see that all three cases have very similar values from $t^* \sim 6$ on.

In this section we have seen that the exit to critical area ratio is of crucial importance and it defines the working regimes of the nozzle. This, in combination with the operating conditions of the nozzle define the behaviour of the flow at the nozzle exit and its vicinity. When operating a nozzle in the under-expanded regime, no changes can be observed at the nozzle exit Mach number, but when the nozzle operates in the over-expanded regime, the exit Mach number reduces drastically (even reaching the subsonic flow). For a specific operating conditions, two nozzles with different geometries can operate one of them in the under-expanded regime and the other in the over-expanded, being the exit flow at the former supersonic, while the latter has subsonic flow at its exit. Therefore we can deduce from this section, that the exit to critical area ratio (mainly) and the operating conditions (at some extent) have a great effect on the nozzle exit flow.

Chapter 6

Pinch-off definition

A part of this chapter has been taken from [**J.J. Peña Fernández** and Sesterhenn, 2017a].

Pinch-off is ideally defined as the separation of the vortex ring from the rest of the fluid flow by a region of zero vorticity. In turbulent flows, due to vorticity diffusion, there is, in fact, no region with zero vorticity. In this chapter, we discuss the relationship between the vorticity field and the pinch-off.

6.1 Pinch-off vorticity threshold ($\omega_{\mathbf{po}}/\omega_{\mathbf{vortex}}$)

We define the pinch-off as the separation of the vortex ring from the rest of the fluid flow by a vorticity threshold of $\omega_{\text{po}}/\omega_{\text{vortex}}$. The vorticity in the vortex ring core is denoted by ω_{vortex}. Choosing a value for this threshold close to unity, we would estimate the pinch-off to occur during the formation of the vortex ring and choosing a value of exactly zero, we would imply that the vortex ring would be surrounded by a large region of almost zero vorticity, being the estimated pinch-off not representative in any of the two cases. Moreover, the region of low vorticity has a flat distribution and the pinch-off definition is very sensitive to $\omega_{\text{po}}/\omega_{\text{vortex}}$.

To choose the proper pinch-off vorticity threshold, we focus now on the limiting vorticity value that separates the vortex ring from the nozzle exit (or the trailing jet) and we call it *separation vorticity* (ω_s). In other words, vortex ring and nozzle exit (or trailing jet) are separated by a region of vorticity with a value of at least ω_s. A lower value than ω_s defines only one region and cannot distinguish both regions, see figure 6.1.

The relative separation vorticity ($\omega_s/\omega_{\text{vortex}}$) decreases with time, see figure 6.2. The pinch-off takes place when this value reaches the pinch-off

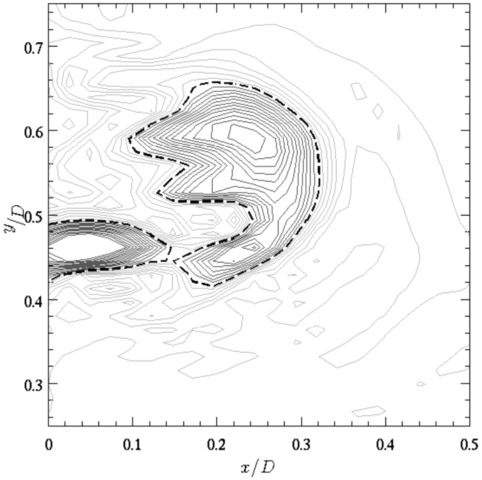

Figure 6.1: Sketch of the pinch-off vorticity threshold method. The black dashed line corresponds to the separation vorticity (ω_s). Higher values of vorticity define two separated regions, while lower values define only one region. Case 7.a is represented.

vorticity threshold ($\omega_{\text{po}}/\omega_{\text{vortex}}$). We defined $\omega_{\text{po}}/\omega_{\text{vortex}} = 0.1$.

The relative separation vorticity shows a local minimum for all cases for $t^* \approx 3.4$, as shown in figure 6.2. This is followed by different local maxima, which are due to vortices from the shear layer (compact regions with large vorticity values) that are taken in by the vortex ring. These vortices from the shear layer 're-join' the vortex ring with the trailing jet and separate them again when they are convected from the shear layer to the vortex ring. This process might be repeated for the few first Kelvin-Helmholtz vortices. This non-monotonic behaviour of the separation vorticity makes the definition of the pinch-off difficult. As an example, assuming $\omega_{\text{po}}/\omega_{\text{vortex}} = 0.1$, the pinch-off would take place multiple times (for $t^* = 5.2$ and 6.5) for the case 1 ($L/D = 0.45$). The pinch-off would take place as well in a 'multiple-way' for the rest of the cases in this study because the vorticity packages have even stronger peaks.

We therefore define the pinch-off as **the first time** that the vortex ring separates from the rest of the fluid flow taking as the pinch-off vorticity threshold $\omega_{\text{po}}/\omega_{\text{vortex}} = 0.1$.

For Reynolds numbers in the range 5 000 − 10 000, the pinch off takes place in a 'multiple-way', because there are more Kelvin-Helmholtz vortices in the shear layer that are taken in by the vortex ring, leading to the peaks

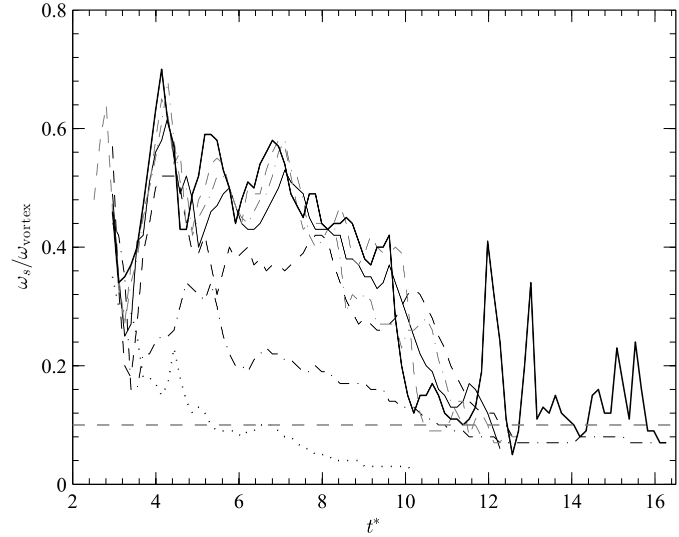

Figure 6.2: Time evolution of the separation vorticity. See legend in table 2.3. The *pinch-off vorticity threshold* ($\omega_s/\omega_{\mathrm{vortex}} = \omega_{\mathrm{po}}/\omega_{\mathrm{vortex}} = 0.1$) is denoted by the horizontal dashed grey line.

in the separation vorticity in figure 6.2. For Reynolds numbers below 3 000, the pinch-off takes place in a single way; the shear layer is stable and the separation vorticity decreases monotonically until the pinch-off vorticity threshold. There exist a critical Reynolds number that defines the boundary between the two types of pinch-off as discussed in 1.3. This is an open question that should be addressed by future research.

The separation vorticity presents a local minimum for all cases for $t^* \approx 3.4$. This minimum can be interpreted as an interruption in the vortex ring generation, which introduces strong perturbations in the vortex ring that can lead to instabilities that grow and make the vortex ring transition to turbulent.

6.2 Circulation divergence law

By computing the circulation (Γ) in a semi-plane that contains the jet axis (hereafter called *sagittal* semi-plane, shown as the light grey region in figure 6.3) and in the intersection of this semi-plane with the vortex ring (dark grey region in figure 6.3), we show that despite injecting more vorticity through the nozzle, from a certain point on, the vortex ring did

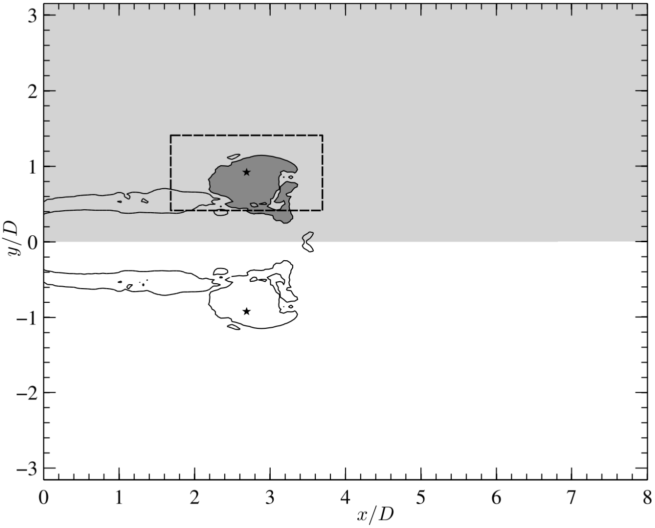

Figure 6.3: Sketch of the different methods used to compute the circulation. The light grey shaded area, defined here as the sagittal semi-plane, is a general semi-plane that contains the jet axis. The black star is the location of the vortex ring following the method proposed by Pawlak et al. [2007]. The dark grey area corresponds to the vortex ring area identified by the flood-fill method centred in the vortex ring location and using as a boundary the contour line $\omega = 0.1\omega_{\text{vortex}}$ (plotted here as a solid black line). For the cases with turbulent vortex ring the most stable method to compute the circulation of the vortex ring is a window of $2D \times 1D$ (plotted as a dashed black line) defined centred in the vortex ring location.

not absorb any vorticity more, see figure 6.4.

For the cases with small L/D (cases 1 and 2), the entire circulation contained in the sagittal semi-plane was concentrated in the vortex ring and no trailing jet was formed, figure 6.4*a*. The vortex ring absorbed the whole vorticity injected through the nozzle. We call this situation a ***non-saturated vortex ring***. A trailing jet was not formed in cases 1 and 2. The small difference between the circulation contained in the vortex ring and in the sagittal plane in figure 6.4*a* is due to the entrainment of fluid, generating a region of positive and negative vorticity close to the lip of the nozzle that decays at a different rate with time, see figures 6.5 and 6.6. This phenomenon takes place in the rest of the cases, but the amount of circulation generated due to the entrainment is neglectable compared to the one in the vortex ring.

For the cases with large L/D (cases 3, 4, 5, 6 and 7), the qualitative

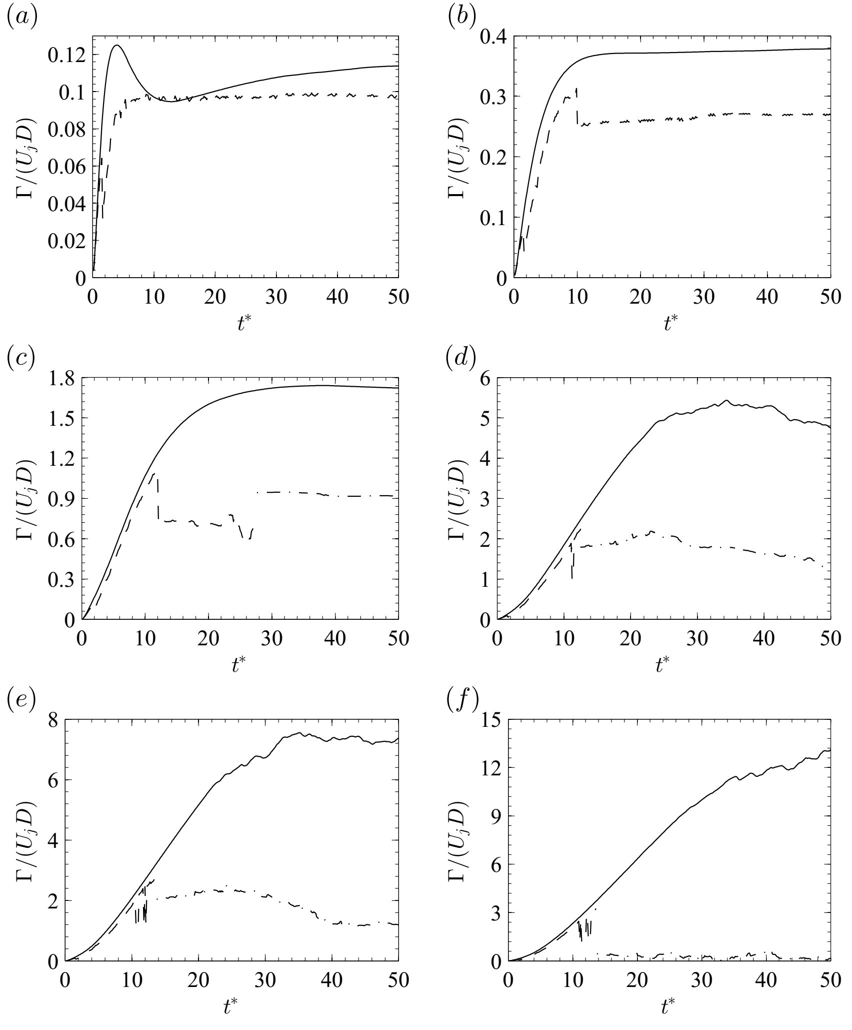

Figure 6.4: Evolution of the circulation contained in the fluid flow for the starting jet. The solid black line corresponds to the circulation contained in the $x-y$ sagittal semi plane. The circulation contained in the intersection of this semi-plane with the vortex ring obtained by the *flood fill* method is represented by the dashed grey line, while the dot-dashed black line corresponds to the *window* method. (*a*) Case 1.*a*. $L/D = 0.45$. (*b*) Case 2. $L/D = 1.17$. (*c*) Case 3. $L/D = 3.80$. (*d*) Case 5. $L/D = 13.55$. (*e*) Case 6. $L/D = 28.59$. (*f*) Case 7.*a*. $L/D \to \infty$.

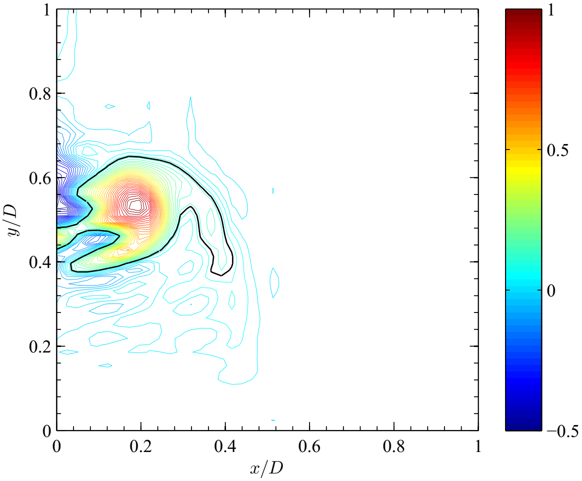

Figure 6.5: Relative vorticity to the maximum vorticity in the vortex ring core ($\omega/\omega_{\mathrm{vortex}}$) for the case 1.$a$ with $L/D = 0.4473$ and for $t^* \approx 4$. The vorticity generated at the inlet condition due to the entrainment affects the circulation calculated by integrating over the whole semi-plane.

behaviour was completely different. After some time, during the injection of the vorticity, the circulation contained in the vortex ring did not follow that contained in the sagittal semi-plane and the vortex ring did not absorb any additional vorticity, as seen in figures 6.4c, 6.4d, 6.4e and 6.4f. We call this situation a ***saturated vortex ring***. The ejected circulation not belonging to the vortex ring formed the trailing jet.

When integrating the vorticity in the intersection of the sagittal plane and the vortex ring, the identification of the integration domain was done by the *flood fill* method, see figure 6.3. While the vortex ring is laminar or remains in low levels of turbulence, the vortex is very clear and both the identification and the integration of the vorticity are straightforward, see figure 6.7a. When the vortex ring becomes turbulent, the region of high vorticity is not a simply connected space and changes drastically with time, which makes the integration much more difficult, see figure 6.7b. This is the reason of the non-uniform behaviour of the vortex ring circulation (dashed line) in figure 6.4. When the vortex ring became turbulent and the circulation obtained was not representative, we integrated the vorticity following the most widespread method used in the literature: integrating the vorticity within a $2D \times 1D$ window, see figure 6.4. The transversal size of the window of $1D$ was chosen not to cross the jet axis when the leading

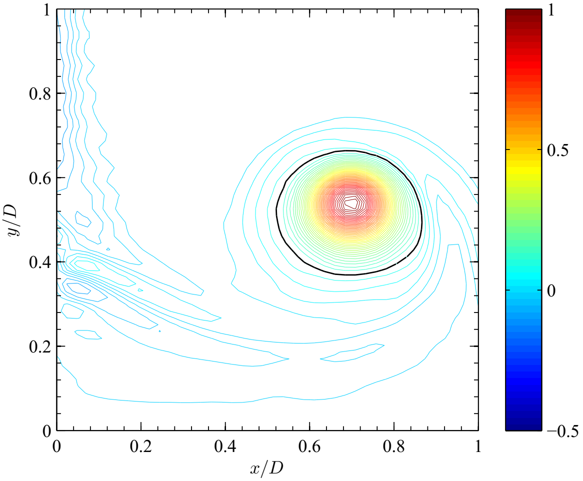

Figure 6.6: Relative vorticity to the maximum vorticity in the vortex ring core ($\omega/\omega_{\text{vortex}}$) for the case 1.$a$ with $L/D = 0.4473$ and for $t^* \approx 12.5$. After some time the effects of the entrainment disappear and the vorticity calculated by integrating over the whole semi-plane converges to the value obtained by integrating only over the vortex ring.

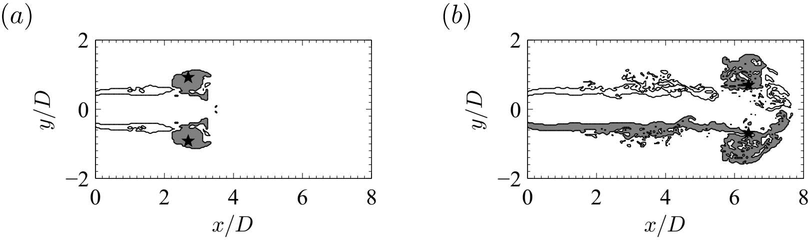

Figure 6.7: Vorticity contour for two different stages of the case 7.c. The solid black line corresponds to $\omega_{\text{po}}/\omega_{\text{vortex}} = 0.1$. The dark grey region is the vortex ring as identified by the flood fill method. The vortex ring (following Pawlak et al. [2007]) is denoted by (★). (a) Successful identification of the vortex ring. The integration of the vorticity within the dark grey domain leads to a proper circulation contained in the vortex ring. $t^* = 12.5$. (b) Unsuccessful identification of the vortex ring. The integration of the vorticity does not give us a proper circulation value because the upper half of the vortex has already been detached from the trailing jet but the lower half is still attached. Furthermore, due to turbulence, the vortex ring is not a simply connected space. $t^* = 22$.

vortex ring is generated, located at $r/D = 0.5$.

We can relate this to the pinch-off process: when the circulation in the vortex ring does not follow the one contained in the sagittal semi-plane, two different regions with relatively high vorticity were created. The divergence of these both curves determines the physical separation of the vortex ring. This divergence can be seen in the different cases in figure 6.4 as well as in figure 6.8. In order to predict the pinch-off, a relationship between the dimensionless time (t^*) and the Reynolds number for which the pinch-off takes place $(\Gamma/(U_j D))_{\text{pinch-off}}$ was established, equation (6.1). Since all pinch-off points are over a straight line in figure 6.8, an empirical linear relationship was indicated as

$$\left(\frac{\Gamma}{U_j D}\right)_{\text{pinch-off}} = 5.0071 - 0.3467(t^*). \tag{6.1}$$

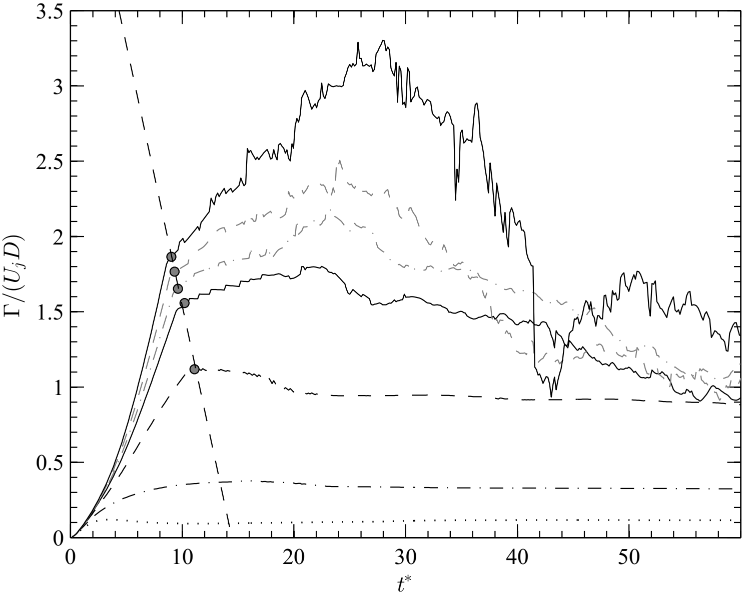

Figure 6.8: Vortex ring circulation over the non-dimensional time. The pinch-off is shown by the points (●) in which the circulation of the sagittal semi-plane and in the vortex ring diverged. A linear regression (- - - - - - -) has been taken into consideration as the relationship that predicts the pinch-off. Lines as in table 2.3.

6.3 Kelvin-Benjamin variational principle

In the case of constant hydrodynamic impulse, the Kelvin-Benjamin variational principle states that a steady distribution of vorticity (relative to a moving reference frame) is the state that maximises the total kinetic energy on an iso-vortical sheet.

The non-dimensional kinetic energy is defined as $\alpha = E/\left(I^{1/2}\Gamma^{3/2}\right)$ where E is the kinetic energy, I is the impulse and Γ is the circulation.

The dimensionless kinetic energy of the starting jet decreases with the time. In the case of the steady vortex ring, a constant dimensionless kinetic energy is expected ($\alpha_{\text{vortex}} = 0.33$) as generally accepted, Gharib et al. [1998]. For the non-dimensional time for which the dimensionless kinetic energy of the starting jet reaches the constant limiting value for the steady vortex ring, the pinch-off takes place and the vortex ring separates from the rest of the flow, see figure 6.9.

The limiting value $\alpha_{\text{vortex}} = 0.33$ is usually derived from the slug model, which limits its generality to impulsively started jets with a constant inlet velocity time distribution and moderate Reynolds numbers, Gao and Yu [2010]. The cases with low C ($C = 1, 2$) pinched off for α larger than the limiting value of 0.33 because the pinch off took place in these cases with the lip of the nozzle and not with the trailing jet, and therefore they are not saturated, but the vortex rings pinching off from a trailing jet agreed very well with the pinch-off at $\alpha_{\text{vortex}} = 0.33$. The pinch-off dimensionless kinetic energy for the different cases in this study is summarised in table 6.1.

Table 6.1: Dimensionless time for which the pinch-off takes place and dimensionless kinetic energy for the different cases under study.

Case	$(t^*)_{\text{pinch-off}}$	$\alpha_{\text{pinch-off}}$
1.a	6.20	0.97
2	10.06	0.69
3	12.13	0.45
4	12.13	0.40
5	13.60	0.34
6	13.60	0.32
7.a	11.83	0.37

In this chapter we defined the pinch-off in a quantitative way using a vorticity threshold as a criterion. The pinch-off takes place when both regions (trailing jet and vortex ring) are separated for the first time through a region with a vorticity lower than the specified threshold: $\omega_{po}/\omega_{vortex} = 0.1$.

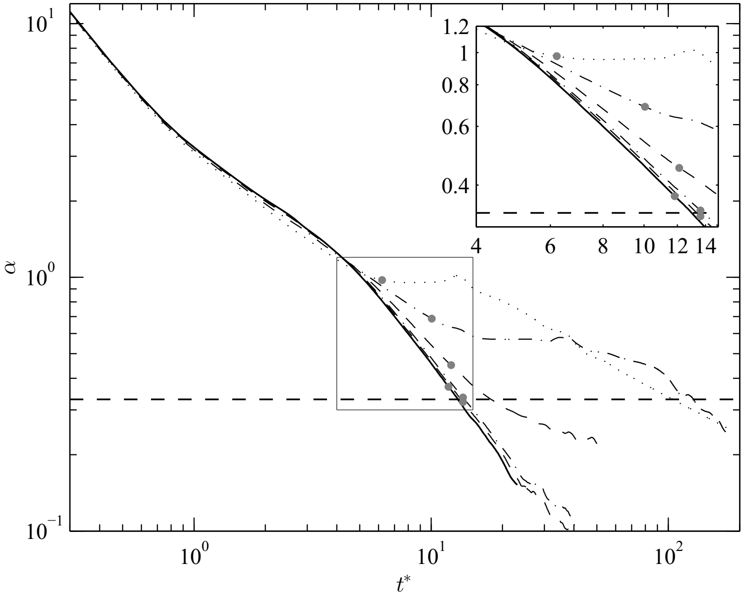

Figure 6.9: Time evolution of the dimensionless kinetic energy for all cases under study. See the legend in table 2.3. The pinch-off is represented by ●. The horizontal dashed black line corresponds to the dimensionless kinetic energy of the steady vortex ($\alpha = 0.33$).

Through the circulation divergence law we showed that despite injecting more vorticity through the nozzle, from a certain point on, the vortex ring did not absorb any vorticity more. We called this the saturation of the vortex ring. We related this to the pinch-off process: when the circulation in the vortex ring did not follow the one contained in the sagittal semi-plane, two different regions of relatively high vorticity were created and this corresponds to the pinch-off. Since all pinch-off points are over a straight line in figure 6.8 we developed an empirical linear relationship to predict the pinch-off.

We applied the Kelvin-Benjamin variational principle to predict the pinch-off and we confirmed the value of the non-dimensional kinetic energy of $\alpha = 0.33$ for the starting jet without decay, but we found that the pinch-off takes place for a higher value of *alpha* for the cases in which the vortex ring was not saturated (a trailing jet was not formed).

Chapter 7

Interaction between the vortex ring and the trailing jet

Part of this chapter has been taken from [**J.J. Peña Fernández** and Sesterhenn, 2017a]. Its fluid dynamics part was presented at the European Turbulence Conference 15 [**J.J. Peña Fernández** and Sesterhenn, 2015c] and the acoustic part was presented at the DAGA 2015, [**J.J. Peña Fernández** and Sesterhenn, 2015a].

In both the starting and continuous stage of the jet there is an interaction between the vortices and the shock waves of the trailing jet, but both of these interactions take place in a slightly different way. In the starting stage, the vortex ring interacts with the shock waves and the vortices of the shear layer, while in the continuous stage, the shock waves interact with the vortices of the shear layer, but not with the vortex ring. Both interactions generate two of the three loudest noise source of the compressible starting jet.

7.1 Shock–shear layer–vortex interaction

When the impulsively started jet is only few nozzle diameters long, the first shock wave extends until the vortex ring core, see figure 7.1*a*. The vortices from the shear layer are convected to reach the shock wave, corresponding to the figure 7.1*b*. In this point takes place the ***shock–shear layer–vortex*** interaction and the shock wave bends due to the vorticity of the shear layer.

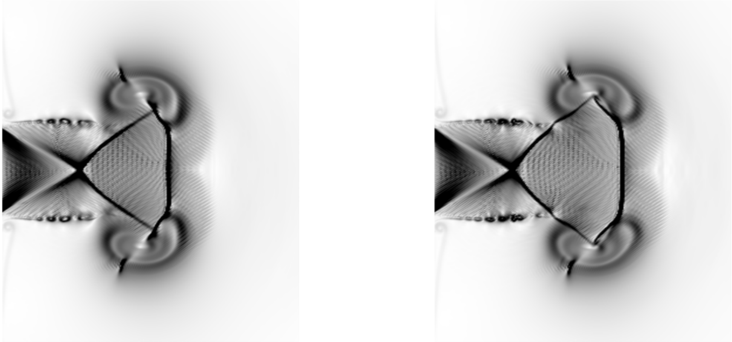

(*a*) Straight shock (*b*) Curved shock

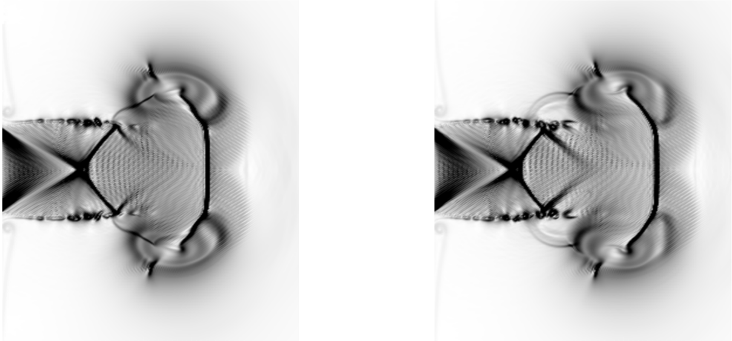

(*c*) Curved and reflected shock (*d*) Radiated shock

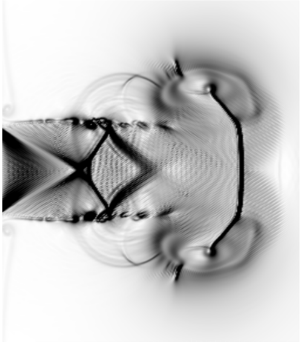

(*e*) Open shock

Figure 7.1: Stages of the shock cell structure during its interaction with the vortex ring. The numerical schlieren $|\nabla\rho|$ is plotted in the range $[0, 2]$. Case 7.*c* is represented for (*a*) $t^* = 5.1$, (*b*) $t^* = 5.6$, (*c*) $t^* = 5.9$, (*d*) $t^* = 6.3$ and (*e*) $t^* = 6.8$.

When the first vortices of the shear layer pass through the shock wave, the velocity gradients of the shear layer bend the affected segment of the shock wave more and more, and the shock wave starts to be reflected in the shear layer, as shown in figure 7.1*c*.

For later times, the segment of the shock wave between the shear layer and the vortex ring is radiated as a strong acoustic wave into the surroundings, figures 7.1*d* and 7.1*e*.

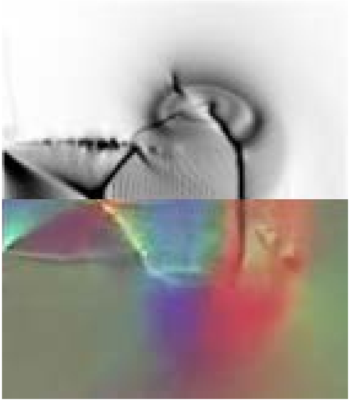

Figure 7.2: Lower half: time-resolved colour schlieren image from Kleine et al. [2010]. Upper half: numerical schlieren corresponding to case 7.*c*.

Figure 7.2 compares visually an experimental schlieren image from Kleine et al. [2010], with a numerical image from case 7.*b*. The different structures and the *shock–shear layer–vortex* interaction can be identified at first sight in both images. The agreement is reasonable. The segment of the shock wave extended from the shear layer to the vortex ring is bent in the same way in both cases just before the sound radiation. Due to the resolution of the experimental image, the details of the leading vortex ring cannot be compared. There is also a region ahead of the vortex ring in which the experiment shows some vorticity content not reproduced in the numerical simulation. The rest of the visible structures are identical.

Figure 7.3 shows the evolution of the flow field during the process. The interaction has already taken place in the shear layer and starts being propagated in the surroundings, figure 7.3*a*. At the same time, the front pressure wave arrives at the numerical probe (★) at $5D$. Figure 7.3*b* shows the entrance of the effects of the interaction in the region where the pressure perturbations are plotted. The front pressure wave has already reached the numerical probe. Further in the process, the front pressure wave exits the computational domain and the sound radiated by the interaction reaches $3.5D$, figure 7.3*c*. In this plot is clear that before the *shock-shear layer-*

vortex interaction there is no noise, as opposed to after it. This interaction states the start of the broadband shock associated noise in the starting jet. Figure 7.3*d* shows the arrival of the sound radiated by the interaction to the numerical probe. The flow develops further until the sound exits the computational domain, figure 7.3*e*. Still, the broadband shock noise is propagated until the numerical probe, figure 7.3*f*.

The time series recorded by the numerical probe (denoted with ★ in figure 7.3) during the interaction is plotted in figure 7.4*a*. The identification of the arrival of the front pressure wave is straightforward and the dashed line indicates the arrival time of the effects of the interaction.

In order to show that this interaction generated a noise at least as loud as the loudest noise sources of the continuous jet for the same parameters, we placed a numerical probe at $5D$ from the jet axis. Pressure fluctuations of approximately 600 Pa were recorded, figure 7.4*a*. Taking the wavelet transformation (complex Morlet wavelet) of the recorded signal we analysed its frequency content as a function of time, see figure 7.4*c*. The correspondence between the peak of the front pressure wave with the maxima of the coefficients for $t^* \approx 6.67$ is straightforward and the peak corresponding to the interaction is also easy to identify. The dashed line in figures 7.4*a* and 7.4*c* represents the time in which the noise generated by the interaction arrives at the numerical probe. The spectrum obtained through the wavelet transformation for the time of the interaction is presented in figures 7.4*d* and 7.4*b* (red), showing a maximum of 118[dB]. The same jet during the continuous stage generates an SPL spectrum shown in figure 7.4*b*, showing values around 100[dB] for the TMN or the BBSN. The noise produced during the starting of the jet by the interaction of the vortex ring with the trailing jet generates at least similar sound pressure amplitudes in the far field to the TMN and BBSN during the continuous stage for the same parameters. The continuous case is the worst scenario to compare: for starting jets with a finite mass supply, the sound radiated by the shock-shear layer-vortex interaction is almost as loud as for the infinite reservoir (due to the small decrease in the Mach number), while the TMN and BBSN are significantly reduced. If no trailing jet is formed, neither the shock-shear layer vortex interaction takes place, nor TMN and BBSN are radiated.

The directivity of this wave has the same pattern as the broadband shock noise, as expected due to the similarities in the generation process.

Since this interaction takes place between the first Kelvin-Helmholtz vortex and the first shock, no acoustic associated to supersonic flow (BBSN and screech) can be radiated before this interaction. This interaction is the onset of the acoustics associated with supersonic flow.

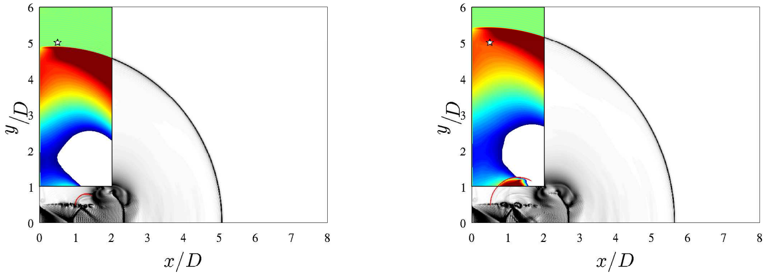

(*a*) Radiation after the interaction. Front pressure wave arrives at the numerical probe.

(*b*) Entrance of the effects of the interaction in the sub-domain of interest.

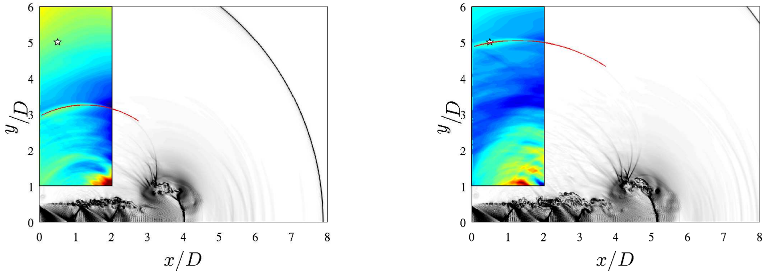

(*c*) Before the interaction there is no noise, whereas after the interaction starts the broadband shock noise.

(*d*) Sound radiated by the interaction arrives at the numerical probe.

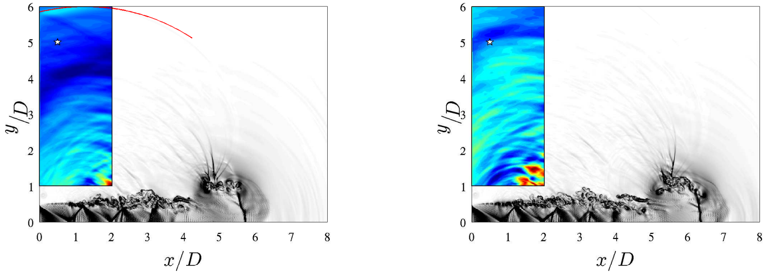

(*e*) The sound radiated by the interaction exits the computational domain.

(*f*) Broadband shock noise arrives to the numerical probe after the interaction.

Figure 7.3: Sketch showing the acoustic radiated by the interaction and measured by the microphone at $r/D = 5$. Numerical Schlieren in black and white contours in the range $[0, 2]$. $(p - p_\infty)/p_\infty$ plotted in blue-to-red colour scale in the range $[\pm 0.024]$. The red line represents the acoustic wave resulting due to the *shock-shear layer-vortex* interaction. Results from case 7.*c*.

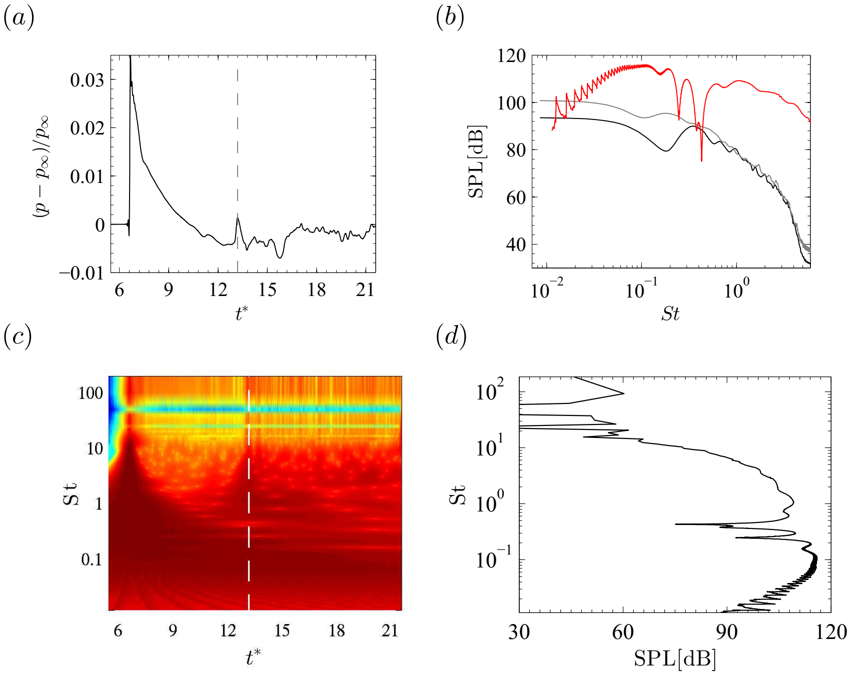

Figure 7.4: The noise produced by the interaction between the vortex ring and the trailing jet is at least as loud as the loudest noise source in the continuous jet in terms of sound pressure level. (*a*) Pressure history measured at $r/D = 5$. The interaction is marked with a grey dashed line. (*b*) Comparison between the SPL spectrum for the shock-shear layer-vortex interaction and for the continuous jet (case 7.*a*), all normalised at $100D$ assuming a radial decay. The shock-shear layer-vortex interaction is represented by the solid red line. Case 7.*a*: probe located at $\theta = 90°$ represented by the solid black line and the probe located at $\theta = 165°$ by the solid grey line. (*c*) Wavelet coefficients of the pressure time signal recorded (shown in (*a*)). (*d*) Sound pressure level spectrum for the time of the interaction based on the wavelet analysis.

As shown in figure 7.5, the result of manually tracking the interaction wave, the interaction wave starts with a subsonic velocity, but after $t^* \approx 1$ the velocity of the wave is approximately the speed of sound in the unbounded chamber where the wave propagates.

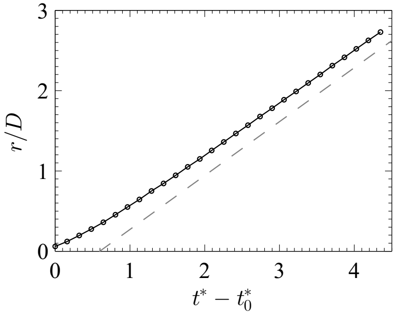

Figure 7.5: Evolution of the position of the interaction wave non-dimensional radius (r/D). As a comparison, the speed of sound has been plotted as a reference with the grey dashed line. t^*_0 is an arbitrary start time from which the manual tracking was carried out, shortly after the time for which the interaction takes place so that we can identify the wave.

7.2 Shock–shear layer interaction

The same interaction, but in a slightly different way takes place when the vortices of the shear layer pass by every shock wave. This is the ***shock–shear layer interaction***.

In a laminar supersonic jet, the surface in which the shock waves are reflected is smooth and steady. However, if the jet is turbulent, this surface is only statistically steady and it has many vortices. Furthermore, the vortices of the shear layer have a high vorticity, comparable or even larger than the maximum vorticity in the vortex ring, that can affect locally the behaviour of the shock wave while being reflected.

When the shock wave is reflected in a very irregular and time changing surface, the region of the shock wave close to the shear layer is bent due to the high vorticity of the shear layer, and this irregular and time depending interaction makes the waves not only to reflect but to refract, due to the changing angle to the surface, which causes the wave to be radiated in an unsteady fashion as strong acoustic waves into the surroundings.

Figure 7.6*a* shows the consequences of the interaction between the shear layer and the shock-cell structure: concentric acoustic waves coming from the intersection of the shock wave with the shear layer, which is one of the strongest acoustic sources in the supersonic starting jet. This interaction is not restricted to the first shock cell. Figure 7.6*b* shows the effect of the two first shock-cells.

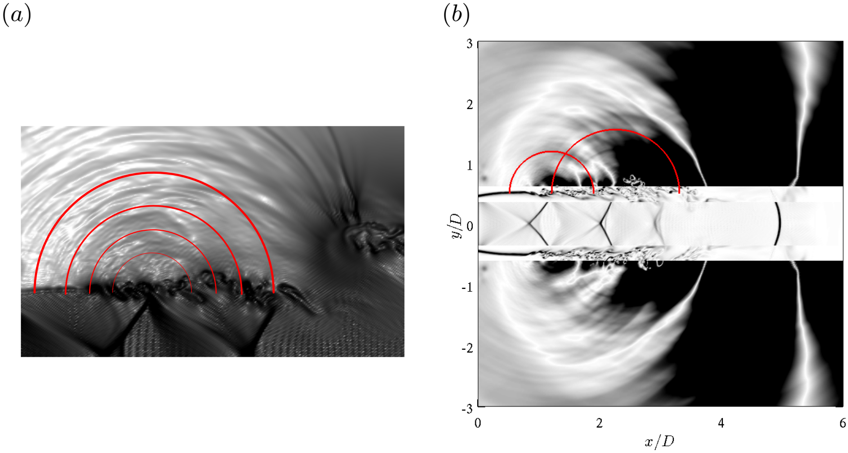

Figure 7.6: The acoustic waves radiated when a vortex passes by a shock wave. (*a*) Density gradients plotted in a logarithmic black and white colour scale showing the direction of radiation of the acoustic waves generated by the interaction of the shear layer and the shock-cell structure. Detailed view. (*b*) Pressure perturbations are plotted in the outer region of the domain. $0 < |p - p_\infty|/p_\infty < 0.03$. In the shear layer region, the vorticity is plotted in order to identify the Kelvin-Helmholtz instabilities. $0 < \omega/\omega_{\text{vortex}} < 2$. In the core of the jet, density gradients are plotted in order to identify the position of the shock waves. $0 < |\nabla\rho| < 20$.

As result from this interaction, strong acoustic waves are radiated every time that a vortex from the shear layer interacts with one of the shock waves present in the flow field. This noise source is also known as broadband shock noise (BBSN).

7.3 Effect of shock-waves dynamics on BBSN

Oscillations of the shock waves in the trailing jet have been reported in the literature for continuous jets, Panda [1998]. The geometry of the shock-cell system is given by p_{0r}/p_∞. In such an unsteady problem, the pressure ratio changes drastically with time, and therefore also the geometry of the shock-cell system.

Due to the impulsive start, p_{0r}/p_∞ changes from zero to the maximum value much faster than the convection velocity of the flow perturbations. The shock-cell pattern is created almost with its final geometry. The last part of the rising stage is no longer impulsively and due to the small and slow increase in p_{0r}/p_∞ the location of the shock waves changes slightly to the final location, see figure 7.7.

During the pressure decay, the lower values of p_{0r}/p_∞ cause the shock waves travel backwards until the lip of the nozzle, figure 7.7*c*. Since the interaction between the shock waves and the vortices of the shear layer play a very important role in the jet noise, the dynamics of the shock waves can be expected to alter the jet noise.

The temporal evolution of the pressure perturbations along the jet axis is shown in figure 7.7 for four representative cases under study. All these cases have in common $Re_D = 5\ 000$, $p_{0r}/p_\infty = 3.6$ and $T_{0r}/T_\infty = 1$; they only differ in the value of L/D. Case 3 has a value of $L/D = 3.80$, case 5 $L/D = 13.55$, case 6 $L/D = 28.59$ and case 7.*a* $L/D \to \infty$. For $t^* = 0$ the whole jet axis is at rest. The oblique line starting in the origin and growing to the right-hand side of the plot is the trace of the vortex ring. After the vortex ring, and close to the lip of the nozzle, the shock waves are created only in the cases 5, 6 and 7.*a*. The shock waves are very easy to identify because of the "zebra" pattern in which a combination of a white and a black stripe corresponds to one shock wave, due to the positive and negative pressure relative to the ambient pressure $(p - p_\infty)$. In these $x/D - t^*$ diagrams, the velocities can be very easily computed by calculating the inverse of the slope of the traces. In figure 7.7*a*, the trace of the first pressure wave can be identified as an oblique line starting from the origin with a flatter slope than the vortex ring, having a reference of the speed of sound at the temperature in the unbounded chamber.

Comparing the slope of the traces of the last shock waves during the decay in figure 7.7*c* with the slope of the first pressure wave in figure 7.7*a*, we can infer that the last shocks are moving with a Mach number close to unity.

The BBSN is generated by the coherent scattering of the large turbulent structures as they pass through the quasi-periodic shock-cells, Tam and Tanna [1982]. Due to the induced velocity of the shock waves during the decay stage, it is expected to have a Doppler effect in the shock associated noise. Moreover, the shock-spacing is expected to be reduced, which leads to a shift in frequencies, including the BBSN peak frequency.

In this chapter we focused on the interaction between the different elements of the jet flow in both the continuous and the starting jet. We identified the *shock–shear layer–vortex* interaction, which takes place in the starting stage and the *shock–shear layer* interaction, which takes place in the stage where the jet can be considered as continuous. Both interactions generate two of the three loudest noise sources of the compressible starting jet. Moreover, we found that during the decay stage, with decreasing pressure at the nozzle exit, the shock-cell spacing becomes shorter and the associated frequency of the radiated broadband shock noise becomes higher. In addition to that, the shock waves travel towards the nozzle exit at a Mach number close to one and it is expected to have a Doppler effect in the shock associated noise.

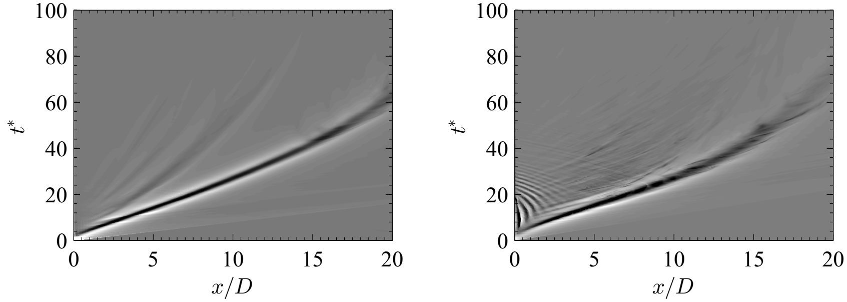

(a) Case 3. $p' \in \pm 10000$ Pa (b) Case 5. $p' \in \pm 25000$ Pa

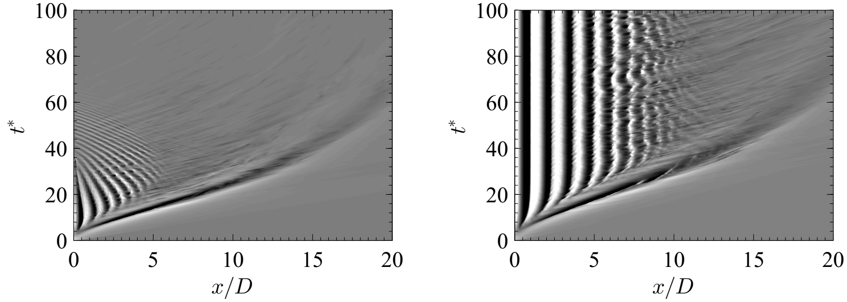

(c) Case 6. $p' \in \pm 37000$ Pa (d) Case 7.a. $p' \in \pm 50000$ Pa

Figure 7.7: Characteristic diagrams showing the development of the first acoustic wave, vortex ring and shock waves for different inlet conditions. Shown is the pressure perturbation (p') history along the jet axis over time.

Chapter 8

Acoustics of the starting jet

This chapter focuses on the acoustics of the compressible starting jet. The three classical noise components (see figure 8.1): turbulent mixing noise, broadband shock noise and screech are already well known in the community, but they are not the only noise sources in the starting jet. The noise due to the compression wave and the vortex ring are also described and analysed in the following sections.

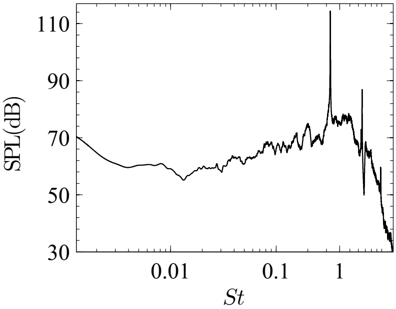

Figure 8.1: Typical sound pressure level spectra for a continuous supersonic jet. Experimental data were measured with the following set-up: $p_{0r}/p_{\infty} = 2.75$, $T_{0r}/T_{\infty} = 1$, $Re_D \approx 2.88 \times 10^5$, $L/D \rightarrow \infty$.

8.1 Compression wave

This compression wave is generated as a result of the sudden expansion of an impulsively started jet. The wave travels at the speed of sound or faster depending on the pressure ratio as explained in section 1.3.3. For the set of parameters used in this study, we analysed only pressure waves travelling at the speed of sound.

By placing a numerical probe in the jet axis at a distance of $5D$ from the nozzle we assessed the pressure profile through the front compression waves for the different values of L/D. The pressure wave was similar for the different cases, figure 8.2*a*. By scaling the time axis with the normalisation factor $(t^*)^{(L/D)^{0.0061}}$ and the pressure axis with $\frac{p-p_\infty}{p_\infty}(t^*)^{(L/D)^{-0.1186}}$, the different profiles collapsed into a single one, figure 8.2*b*.

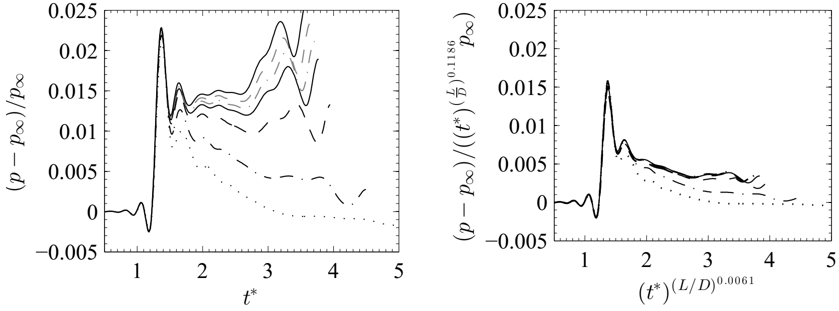

(*a*) Original axis (*b*) Similarity axis

Figure 8.2: Pressure profile through the first wave for the cases with different L/D values in the original (*a*) and similarity axis (*b*). See legend in table 2.3. The time axis origin has been displaced (t_0^*) to show a convenient dimensionless time range.

Before the pressure wave met the numerical probe (for $t^* \sim 1$), we recorded small but increasing fluctuations. The amplitude of this rising fluctuations was not affected by L/D. After the small pressure fluctuations, the strong pressure wave passed by the numerical probe. The amplitude of the strong pressure wave did not depend on the value of L/D. The signal after the pressure wave did not decay to the surroundings pressure, which means that the pressure wave did not travel alone. These perturbations were presumably originated by the shear layer vortices that were leapfrogged by the main vortex ring. During the decay after the strong pressure wave the qualitative behaviour between the curves with different L/D was different, the cases with smaller L/D tended to decay faster than the cases with larger L/D, because the vortex ring travels slower in the cases with lower L/D.

The cases with large L/D were successfully collapsed into a single curve. The cases with $L/D = 0.4473$ and 1.1730 were the most difficult to scale, due to the low Mach number relative to the others. In these two cases there was no trailing jet and therefore there was no signal of the leapfrogged vortices from the shear layer.

8.2 Vortex ring

Here we have to distinguish between laminar and turbulent vortex rings:

Laminar vortex ring: The generated laminar vortex rings did not radiate any acoustic during the whole simulation.

Turbulent vortex ring: Ran and Colonius [2009] measured the acoustic field around a circle $x/R = 16.1$ and they found that the sound pressure level of the vortex ring peaks when the instabilities become non-linear and the vortex ring starts to breakdown. The pressure signals have a distinct frequency at this stage. As the vortex ring transitions and vorticity begins to decay, both the amplitude and the frequency of the pressure distribution decrease as well.

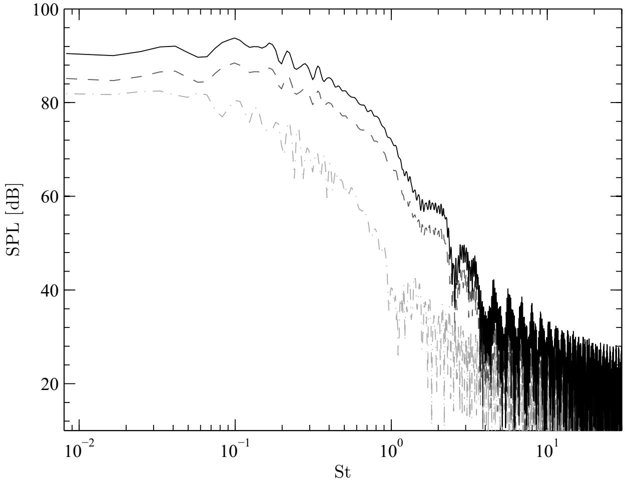

Figure 8.3: SPL spectrum of the acoustic radiated by the vortex ring in a reference frame moving with the vortex ring. The dot-dashed light grey line corresponds to the acoustic radiated at $\theta = 90°$ with respect to the jet axis, the dashed grey line corresponds to $\theta = 135°$ and the solid black line to $\theta = 157.5°$. This results correspond to case 1.*a*.

We measured the noise radiated by a turbulent vortex ring at different angles with respect to the jet axis and the sound pressure level spectrum is shown in figure 8.3. The noise is rather low-frequent ($St \sim 0.1 - 1$) with a steep decay for high frequencies.

8.3 Turbulent mixing noise

The turbulent mixing noise (TMN) is the component of jet noise in which the turbulence of the jet is involved. This is the dominant noise component in the downstream direction of the jet. Both the large coherent structures and the fine scale turbulence contribute to the turbulent mixing noise. The terms 'fine scale' and 'large coherent structures' turbulence noise are very imprecise and are not well defined in the literature.

- Large turbulence noise. Discussed in detail in [Tam and Burton, 1994]. Mach waves are generated when the large turbulence structures propagate downstream at a supersonic speed relative to the ambient condition. This is the dominant part of the turbulent mixing noise for supersonic jets, especially for high supersonic. In supersonic jets, it is also called *Mach wave radiation*. See figure 8.4.

- Fine-scale turbulence noise. Although it is clear that turbulence would lead to flow unsteadiness and hence sound generation, yet the exact process by which fine-scale turbulence produces noise remains not well understood. This part is responsible for the background noise. This part dominates the turbulent mixing noise for subsonic jets.

Turbulent mixing noise appears in both the subsonic and supersonic continuous jet cases. Since the interaction of turbulence takes place in both regimes, both subsonic and supersonic jets radiate turbulent mixing noise, being the dominant component not the same in both cases.

The typical radiation diagram of the turbulent mixing noise has a broad peak at Strouhal numbers of the order 10^{-1}. In the upstream direction, the fine scale turbulence noise dominates the spectrum and therefore it is broader than in the downstream direction, where the large turbulence noise dominates.

TMN can be measured in subsonic jets at all angles. The large-scale turbulent noise is dominant in the forward arc, while the fine-scale turbulent noise in the rear one. For supersonic jets, the supersonic jet noise components are dominant in the rear arc, so that the fine-scale turbulent noise is more difficult to measure, but in the forward arc, the large-scale turbulent noise is still dominant.

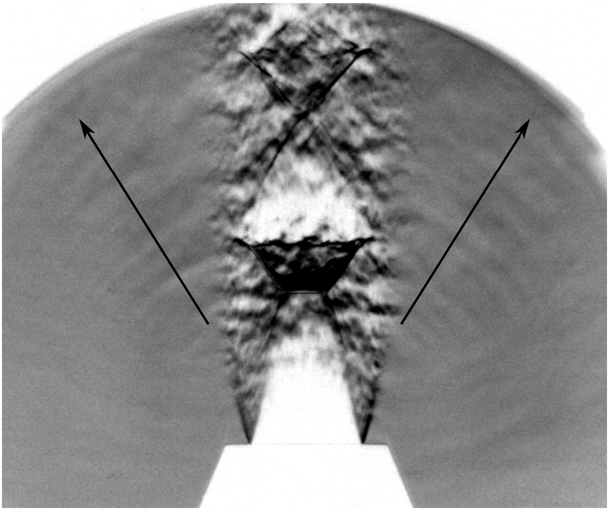

Figure 8.4: Large scale turbulence noise waves visible in a schlieren picture of an under-expanded jet. $p_{0r}/p_{\infty} = 4.1$, $Re_D \approx 2.88 \times 10^5$, $T_{0r}/T_{\infty} = 1$, $L/D \to \infty$.

8.4 Broadband shock noise

Broadband shock noise appears only in imperfectly expanded supersonic jets. A quasi-periodic shock cell structure is built because of the mismatch of the static pressures inside and outside the jet. The broadband shock associated noise (BBSN) is generated by the interaction between the turbulence structures of the shear layer and the shock waves of the shock cell structure. On the one hand, the shock waves are quasi stationary in a continuous jet and they do not translate. On the other hand, the turbulent structures of the shear layer are convected downstream with the jet flow. When the turbulent scales pass through the position where the shock wave is located, a high amplitude perturbation is generated and radiated into the surroundings.

An alternative point of view of the BBSN generation mechanism is through the $M = 1$ line in the shear layer. As shown in figure 8.5 represented in red, the $M = 1$ line is located in the shear layer in a supersonic jet. With the evolution of the Kelvin-Helmholtz vortices, the $M = 1$ line bends because of the vorticity contained in the vortices. When the vortices of the shear layer are convected along the boundary of the jet core and they travel through the location of a shock wave, the $M = 1$ line encloses a small supersonic region in the subsonic ambient. This perturbation settled in the subsonic part of the fluid flow is propagated into the surroundings producing the BBSN.

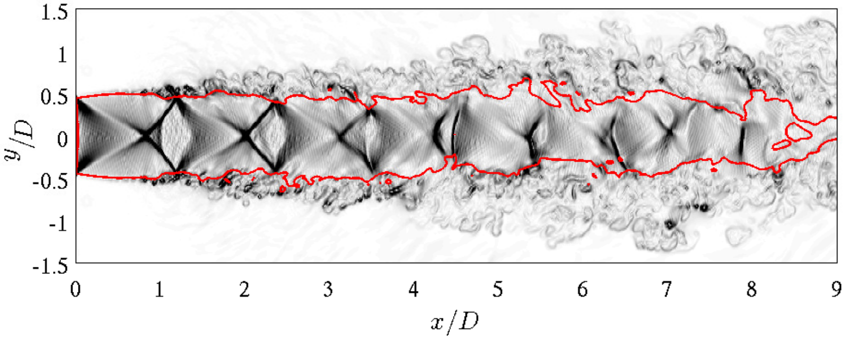

Figure 8.5: Numerical schlieren $|\nabla\rho| \in [0, 4]$ represented in black and white (white for low values and black for large values) over a plane containing the jet axis. The $M = 1$ contour line is represented in red. Case 7.c is shown.

The large range of scales of the turbulence and the randomness of the interaction between shear layer vortex and shock waves gives the BBSN its broadband property.

The shock cell spacing is the appropriate length scale that determines the broadband noise peak, as reported by Norum and Seiner [1982]:

$$\frac{L_s}{D} = 1.1\sqrt{M_j^2 - 1}.$$

The amplitude of the BBSN in the noise spectrum rises rapidly with the Strouhal number to a well-defined peak and then decreases exponentially at higher Strouhal numbers. The Strouhal number of this peak shows a Doppler shift with the direction of radiation and therefore the peak Strouhal number is referenced at 90°.

The directivity is found to be pointed in the upstream direction, with omnidirectionality being only approached at high-pressure ratios. The relative importance of shock noise with respect to jet mixing noise is found to be maximum near the pressure ratios at which a Mach disk begins to form in the jet [Seiner and Yu, 1984]. The relative importance of shock noise in comparison with jet noise for a convergent nozzle generally increases with increasing pressure ratio and increasing angle from the downstream jet axis [Tanna, 1977].

8.5 Screech

Screech tones are the least understood component of supersonic jet noise. It is generated through a feedback loop: the instabilities from the shear layer are detached into acoustic waves; they travel in all directions, but especially upstream outside the jet to the nozzle lip; there, they trigger new instabilities that are convected downstream in the shear layer to the place they are detached, closing the loop with a specific frequency. The screech tone shows a mode switching feature with the fully expanded jet Mach number. From the three components of the feedback loop (shock waves, acoustic waves and instabilities in the shear layer of the jet), the mode shape and tone intensity are characterised by the properties of the jet instabilities. They are the energy source of the feedback loop.

The screech frequency can be predicted with certain accuracy (see equation (8.1)), but the amplitude of the screech tones varies largely without changing the governing parameters. Norum [1983] reported an increase in the screech tone amplitude of $10dB$ when a thin lip nozzle was replaced by one with a thicker lip. Moreover, Seiner et al. [1986] reported a rotation of almost 90° in the flapping plane when the same experiment was repeated a month later at the same facility by the same investigators. Further work is needed to fully understand the noise generation mechanisms and the sensitivity of this feedback loop.

Both the intensity and the frequency of screech tones generally decreases with an increase in the jet temperature:

$$\frac{f_s D_j}{u_j} = \frac{0.67}{\sqrt{M_j^2 - 1}} \left(1 + \frac{0.7 M_j}{\sqrt{1 + \frac{\gamma - 1}{2} M_j^2}} \left(\frac{T_{0r}}{T_\infty} \right)^{-\frac{1}{2}} \right)^{-1} \tag{8.1}$$

Note here the assumption that the convective Mach number is 0.7 times the fully expanded Mach number. There is not unanimity about the convective Mach number in the literature, but this formulation delivers good enough results for the purposes of this thesis.

The fundamental screech tone radiates primarily in the upstream direction. The principal direction of radiation of the first harmonic is 90°. The tone directivity is not affected by the temperature.

8.6 Directivity of the noise radiated

The directivity of the different jet noise components is well known in the community for the case of the continuous jet, see figure 8.6. The TMN is radiated mainly in the downstream direction while the BBSN is radiated mainly in the transverse-upstream direction. In the case of the existence of

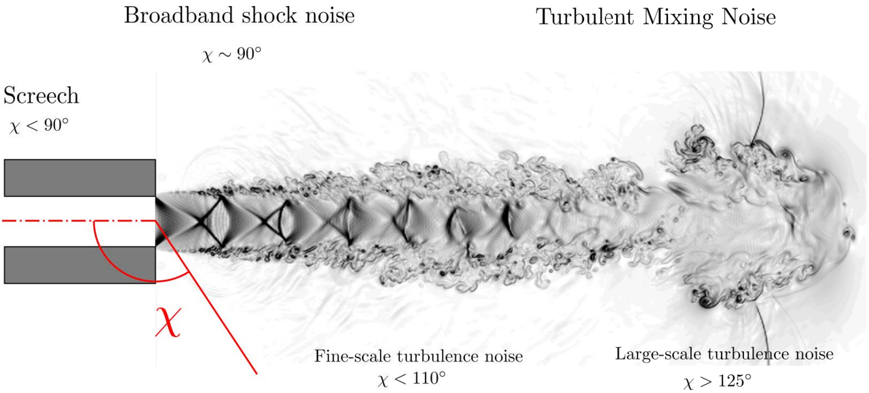

Figure 8.6: Directivities of the different components of the jet noise.

screech tones, they are also radiated in the transverse-upstream direction.

We present here the different noise sources of the starting jet with their directivity in order to analyse the angular dependence of the SPL spectra for the starting jet.

The front pressure wave is radiated in all directions as a spherical wave, starting at the lip of the nozzle and propagating with the speed of sound. The spectrum of the first pressure wave would be flat, analogous to a Gauss pulse.

The noise produced by the vortex ring is mainly radiated downstream, see figure 8.3. The spectrum corresponding to the point downstream has a larger amplitude for the complete range of frequencies than for the point upstream.

In the starting jets with a trailing jet, TMN is radiated in the downstream direction. BBSN is only radiated when shocks are present in the flow field, this is, in the time interval when the trailing jet is supersonic. In this case, the BBSN is radiated, as in the continuous jet, in the transverse-upstream direction. The noise radiated by the shock-shear layer-vortex interaction is also radiated in the transverse-upstream direction.

We analysed the SPL spectrum in two directions ($\theta = 165°$ and $90°$) in order to identify the acoustic footprint of the different physical phenomena. Figure 8.7a shows the stream-wise acoustic radiation of the vortex ring in the case 1.a, and the turbulent mixing noise in the cases 5 and 7.a. Except for the low Strouhal numbers, where there is less information, the spectra are qualitatively similar. Figure 8.7b shows the acoustic radiation in the transverse direction ($\theta = 90°$). Case 1.a is qualitatively very different from both cases 5 and 7.a. From the curve of case 7.a, we identified the frequency range which corresponds to the BBSN, and we identified as well that the curve corresponding to case 5 has the highest frequencies of the BBSN, but not the lowest. The supersonic time interval in case 5 was not long enough to radiate the lowest frequencies of the BBSN.

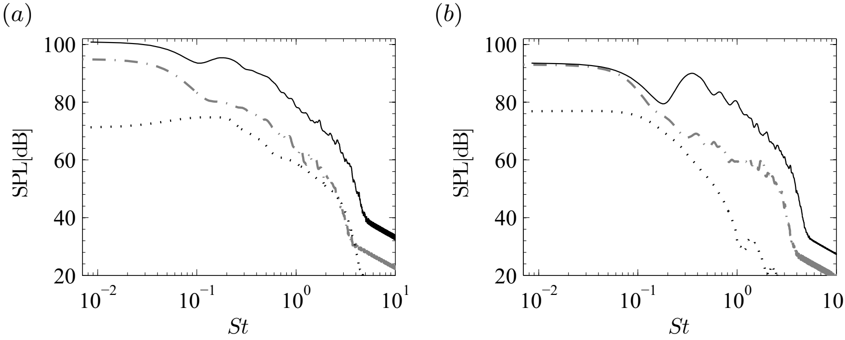

Figure 8.7: SPL spectra radiated (*a*) downstream ($\theta = 165°$) and (*b*) in the transverse direction ($\theta = 90°$). Only cases 1.*a*, 5 and 7.*a* are represented.

We present here experimental results that agree and complement the previous results. Figure 8.8 shows the sound pressure level spectrum of four experimental continuous jets measured at two different angles: $\theta = 90°$ and 160°. All these experiments were performed in the anechoic chamber at the Berlin Institute of Technology (see section 3.2).

The first jet (figure 8.8*a*) was generated with a pressure ratio of $p_{0r}/p_\infty = 1.8$ therefore it is transonic ($M_j = 0.9562$). We see in the spectrum at 160° (in red) the turbulent mixing noise due to large turbulent structures with a maximum at approximately $St = 0.1$ and in the spectrum at 90° (black) a broader maximum in which the highest frequencies are not visible because of the cut-off frequency of the used microphones (20 000 Hz). The supersonic jet noise components are not dominant in this case.

The second jet (figure 8.8*b*) was generated with a pressure ratio of $p_{0r}/p_\infty = 2.6$, which leads to $M_j = 1.2528$. The fundamental screech tone dominates the spectrum with a sharp peak at approximately $St = 0.36$. For lower Strouhal numbers in the spectrum at 160°, the large turbulent scales noise is shown. In the spectrum measured at 90° we also see the screech tone for the same Strouhal number. For lower Strouhal numbers, the fine-scale turbulence noise component of the turbulent mixing noise is present, but for higher Strouhal numbers the broadband shock noise is not visible; it is expected for higher Strouhal numbers than the microphones were able to measure.

The third jet (figure 8.8*c*) was generated with a pressure ratio of $p_{0r}/p_\infty = 3.5$, which leads to $M_j = 1.4669$. The fundamental screech tone dominates the spectrum with a sharp peak at approximately $St = 0.28$. Concerning

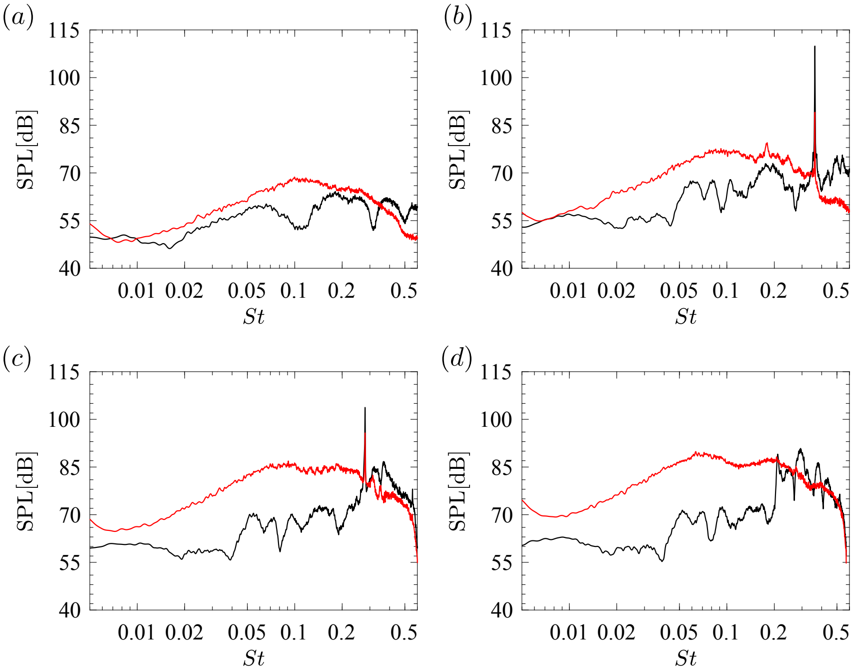

Figure 8.8: (*a*) $p_{0r}/p_\infty = 1.8$. (*b*) $p_{0r}/p_\infty = 2.6$. (*c*) $p_{0r}/p_\infty = 3.5$. (*d*) $p_{0r}/p_\infty = 4.1$. The noise spectrum is represented at $\theta = 90°$ (black) and at $\theta = 160°$ (red). Experimental data obtained in the laboratory.

the spectrum at 160°, there is a frequency shift in the different noise components due to the different pressure ratio and the amplitude of the large turbulent scales noise has increased up to 10dB. In the spectrum at 90°, the part of the BBSN with the lowest Strouhal numbers was measured by the microphones and is visible. This shows how dominant is the BBSN against the fine-scale turbulent noise for this configuration.

The fourth jet (figure 8.8*d*) was generated with a pressure ratio of $p_{0r}/p_\infty = 4.1$, which leads to $M_j = 1.5756$. By some reason, the amplitude of the screech tone has been reduced noticeably, although it is visible in the spectrum at 90° at approximately $St = 0.21$. The spectrum at 160° does not show major differences with respect to the previous case. The spectrum at 90° shows for this configuration the Strouhal number for which the BBSN has the maximum amplitude, showing as in the previous case how BBSN dominates over fine-scale turbulent noise for this configuration.

8.7 Frequency-time domain (wavelet) analysis

Part of the work corresponding to this section was presented in the 20th International Congress on Sound and Vibration (ICSV20), [**J.J. Peña Fernández** and Sesterhenn, 2013b].

In this section, we report on the frequency–time localisation of the noise sources in the continuous and starting–decaying jet. Cases 1.a, 3, 4, 5 and 7.a have been analysed in which the non-dimensional mass supply was changed, having the case 1.a the lowest value and the case 7.a the largest.

With numerical probes, we recorded the acoustics at three different angles: (i) 0°, at the jet axis at a distance of $x/D = 7$. (ii) 45°, at a distance of $7D$ from the nozzle exit centre and 45° with respect to the jet axis. (iii) 90°, at the sideline and at a distance of $7D$ with respect to the jet axis.

These signals have been transformed into the Fourier space and represented as the sound pressure level spectra, which is the classical result shown in the jet noise literature. This shows the frequency content of the acoustic signal but there is no time localisation, and therefore we performed as well a wavelet analysis of the radiated acoustics to have a better knowledge about the time dependency.

Starting with the starting continuous jet (case 7.a) and decreasing the non-dimensional mass supply value we show the obtained results.

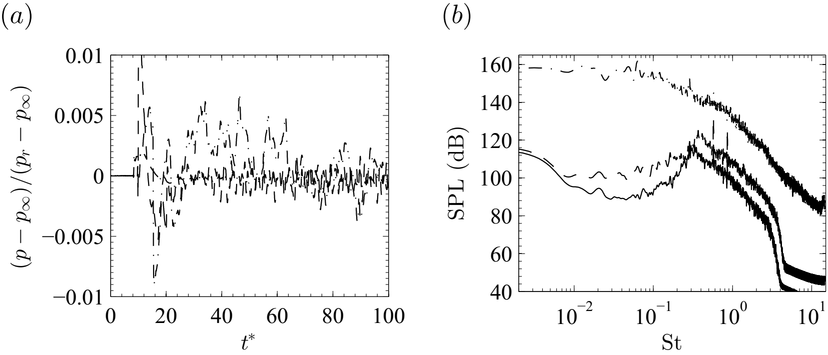

Figure 8.9: (a) Time series and (b) sound pressure level spectrum of case 7.a. The signal was recorded at 0° (dot-dashed), 45° (dashed) and 90° (solid).In (a) the curve of 0° (dot-dashed) is scaled by a factor of 0.04 to better visualization.

Figure 8.9a shows the pressure history measured at the three stations for the case 7.a. The quiescence conditions can be seen in all three curves until $t^* \sim 7$. The first large peak is the trace of the compression wave, and it is followed by also very large oscillations in the probe at 0° and smaller oscillations for the other two probes. The signal does not decay, since we regard the case with an infinite reservoir. Figure 8.9*b* shows the associated sound pressure level spectra. At the jet axis, we measured only TMN with very large amplitudes. In both probes at 45° and 90° we can identify TMN in the low-frequency range, while the BBSN is clear in the range $Sr \sim 0.3 - 4$. Two sharp peaks are visible for $Sr \sim 0.5$ and 1, which correspond to the screech tone and one harmonic.

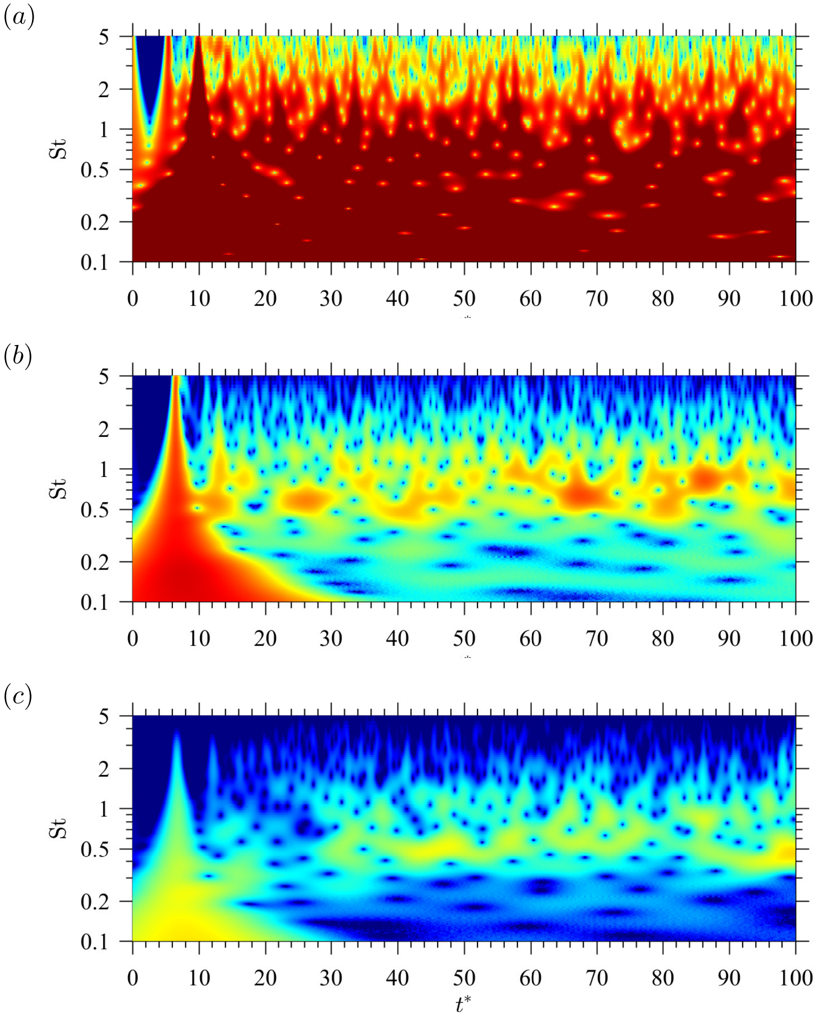

Figure 8.10: Continuous wavelet transformation coefficients in logarithmic colour scale for case 7.*a*. The colour-scale is in the range [60, 130] [dB]. (*a*) Microphone located at 0°. (*b*) Signal at 45°. (*c*) Signal at 90°.

Figure 8.10 shows the wavelet coefficients of the transformed signal measured at the three stations. At 0° the low frequent TMN dominates after the first compression wave as previously stated. Here we can observe how irregular with time is the behaviour in the high frequencies. At 45°, the first compression wave can be seen followed mainly by BBSN in the range $Sr \sim 0.2 - 1$. At 90° the amplitudes are lower than at 45°, but the distribution does not differ much from the previous plot.

In the following, we present the same results for the cases with a finite reservoir, where the jets decay with time until quiescence conditions.

Figure 8.11*a* presents the pressure time series of case 5. After the large oscillation due to the first compression wave, there are oscillations of lower amplitude generated by the trailing jet and at some point the oscillations decay. In figure 8.11*b* is the sound pressure level represented. At 0° only TMN can be identified, while at 45° and 90° also BBSN can be seen, at least its largest frequencies. In these plots, no screech tones were observed.

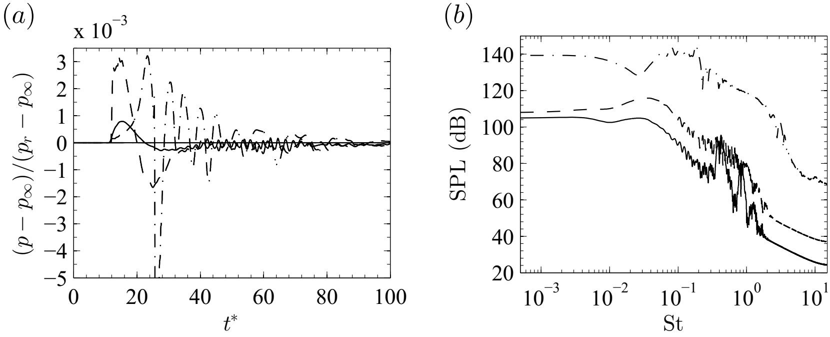

Figure 8.11: (*a*) Time series and (*b*) sound pressure level of case 5. The signal was recorded at 0° (dot-dashed), 45° (dashed) and 90° (solid). In (*a*) the curve of 0° (dot-dashed) is scaled by a factor of 0.04 to better visualization.

Figure 8.12 shows the wavelet coefficients of the transformed signal of case 5. At 0°, we can recognise the first compression wave followed by TMN, where the amplitude at low frequencies starts to decay. At 45°, after the compression wave, there is a time span until $t^* \sim 90$, where also BBSN is present and then the jet decays presumably in the subsonic regime and the amplitudes decay as well. At 0° this time interval is even more clear in which the BBSN is emitted, namely between $t^* \sim 30 - 90$.

We present now the results of case 4 in figure 8.13 for a smaller non-dimensional mass supply. The pressure time series are qualitatively very similar to the previous case with the only exception to decay faster. After the first compression wave, we see for 0° large perturbations due to pressure

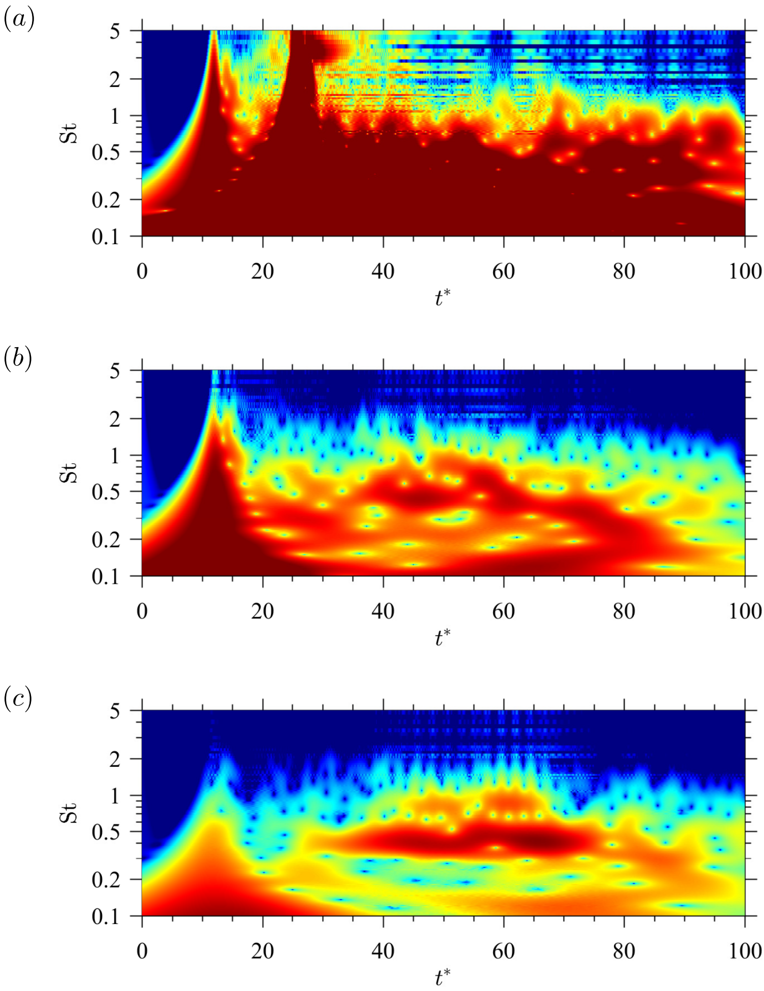

Figure 8.12: Continuous wavelet transformation coefficients in logarithmic colour scale for case 5. The colour-scale is in the range [60, 130] [dB]. (*a*) Microphone located at 0°. (*b*) Signal at 45°. (*c*) Signal at 90°.

changes at the vortex ring centre. For 45° and 90°, we can see mainly the compression wave. In the sound pressure level spectra, we observe for the three directions the first compression wave and TMN. Also few of the largest BBSN frequencies are present in the 90° curve (approximately at $Sr \sim 0.5$).

Figure 8.14*a* shows after the first compression wave lower frequent con-

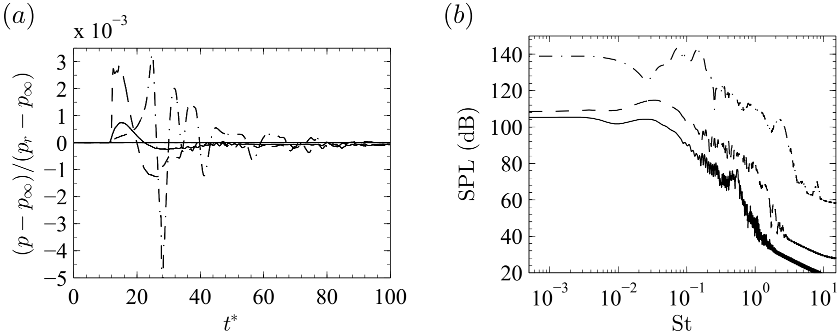

Figure 8.13: (*a*) Time series and (*b*) sound pressure level spectrum of case 4. The signal was recorded at 0° (dot-dashed), 45° (dashed) and 90° (solid). In (*a*) the curve of 0° (dot-dashed) is scaled by a factor of 0.04 to better visualization.

tent with time until $t^* \sim 50$ and then there is a change and higher frequencies are also excited until $t^* \sim 90$. After the first compression wave there is some TMN and BBSN, but then the jet decays and these components are no longer present. At $t^* \sim 70-80$, the noise from the vortex ring breakdown is radiated and therefore present in this plot. At 45° and 90°, the three components are even clearer: the first compression wave for early times, for $t^* \sim 30-60$ we can observe TMN and BBSN and the vortex breakdown for $t^* \sim 80$.

With lower values of the non-dimensional mass supply, we present here the results of case 3. Figure 8.15*a* decays faster than in the previous case, as expected. For 0° both the first compression wave and the trace of the vortex ring are visible, while for 45° and 90° only the first pressure wave is observable. When looking at the sound pressure level spectra, we can observe the typical spectra associated with the first compression wave and for 90° the pressure perturbations associated to the vortex ring. At 90° there might be some content associated to TMN at $Sr \sim 0.8$.

Figure 8.16 shows the wavelet coefficients of the transformed signal. At 0°, after the compression wave, we observe low frequent content associated with the pressure oscillations of the vortex ring. For later times we observe low-frequency content of much smaller amplitude which origin is the induced flow after the vortex ring. At 45° and 90°, we can only see the first compression wave and the perturbations due to the vortex ring.

Note here that the perturbations of the vortex ring arrive at the microphone located at 90° later than at the 45° one due to their location: all microphones are located at the same distance from the nozzle exit centre line, but not from the point in which the vortex ring radiates its noise.

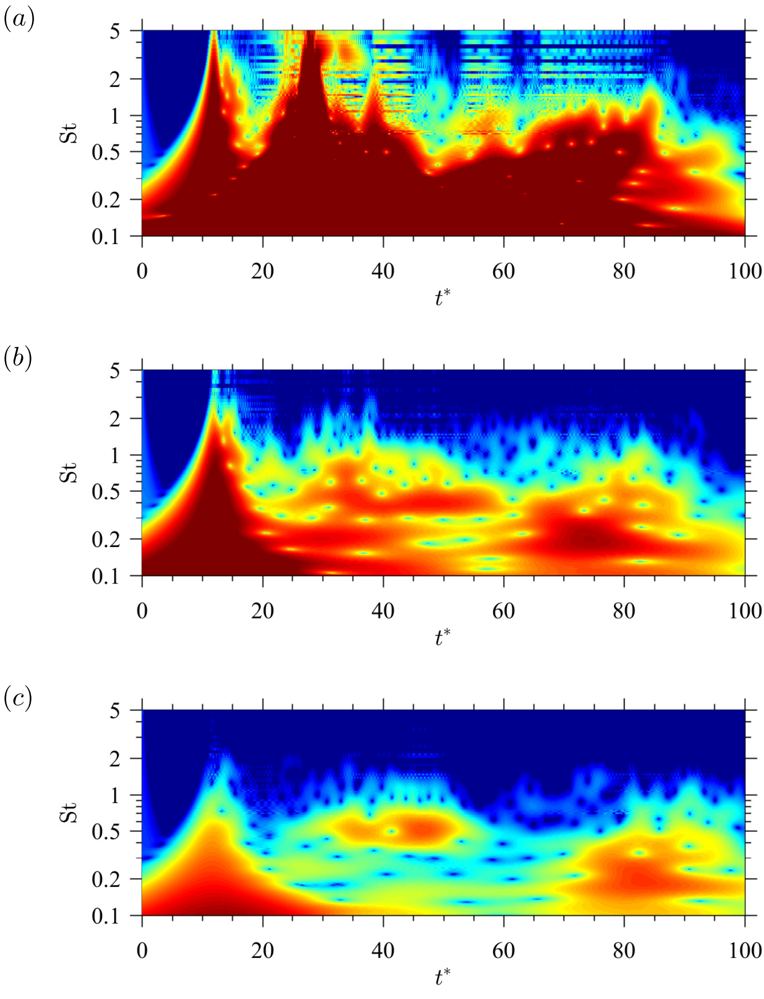

Figure 8.14: Continuous wavelet transformation coefficients in logarithmic colour scale for case 4. The colour-scale is in the range $[60, 130]$ [dB]. (a) Microphone located at 0°. (b) Signal at 45°. (c) Signal at 90°.

For the case with the lowest non-dimensional mass supply in this analysis (case 1.a), we can observe in figure 8.17a mainly the compression wave arriving at the three probes simultaneously. A relatively weak vortex ring arrives at the microphone located at 0°. Figure 8.17b shows the associated sound pressure level spectra, where only the compression wave can be

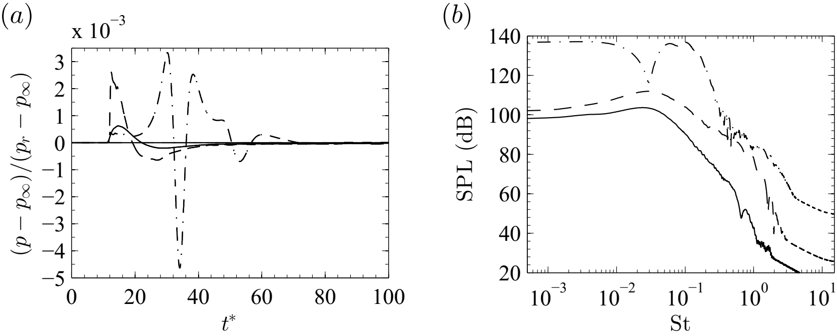

Figure 8.15: (*a*) Time series and (*b*) sound pressure level spectrum of case 3. The signal was recorded at 0° (dot-dashed), 45° (dashed) and 90° (solid). In (*a*) the curve of 0° (dot-dashed) is scaled by a factor of 0.1 to better visualization.

identified.

Figure 8.18 shows the wavelet coefficients of the transformed signal of case 1.*a*. It is very similar for the three angles, showing mainly the first compression wave and some trace of the vortex ring for slightly later times.

As a general trend we have seen in this section how starting from a jet without decay, with an infinite reservoir, we can identify the different noise components by analysing the time series, the sound pressure level spectrum and the wavelet coefficients of the transformed signal. As we simulate smaller and smaller reservoirs, the supersonic stage of the jet is reduced in time and the BBSN loses importance. The same happens to the TMN as the parameters approach the limit of trailing jet existence. For very small reservoirs, only a compression wave and a relatively weak vortex ring are present in the fluid flow. This link between the acoustics radiated and the different features of the starting-decaying jet allows us to move to the next chapter and predict the governing parameters from acoustic measurements.

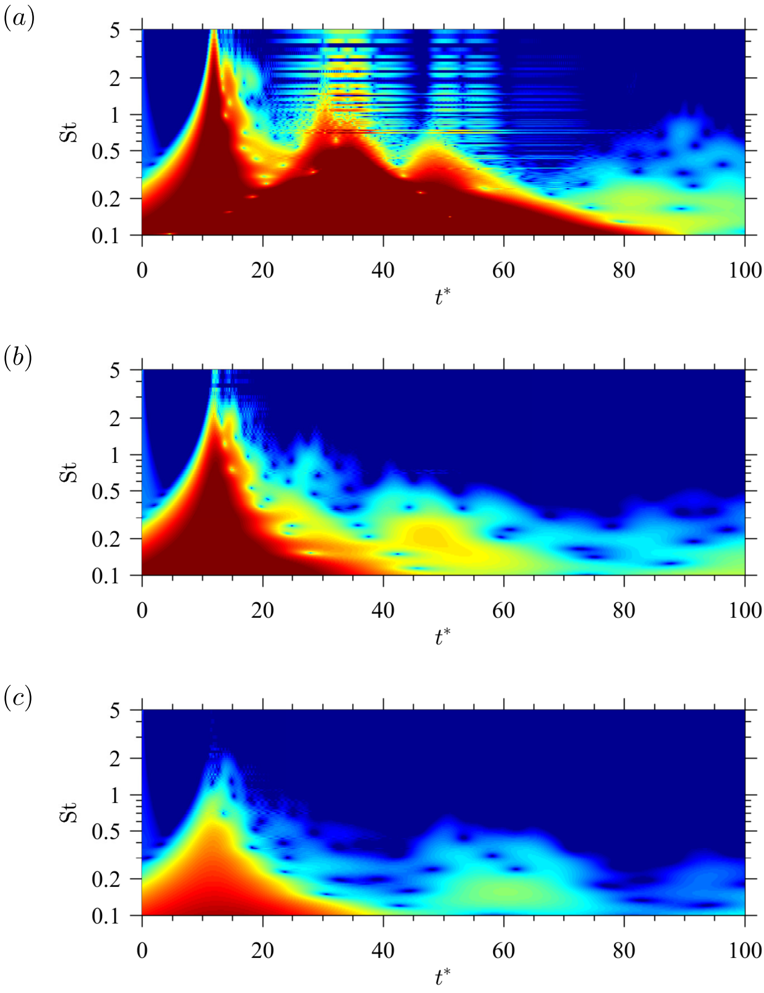

Figure 8.16: Continuous wavelet transformation coefficients in logarithmic colour scale for case 3. The colour-scale is in the range $[60, 130]$ [dB]. (*a*) Microphone located at 0°. (*b*) Signal at 45°. (*c*) Signal at 90°.

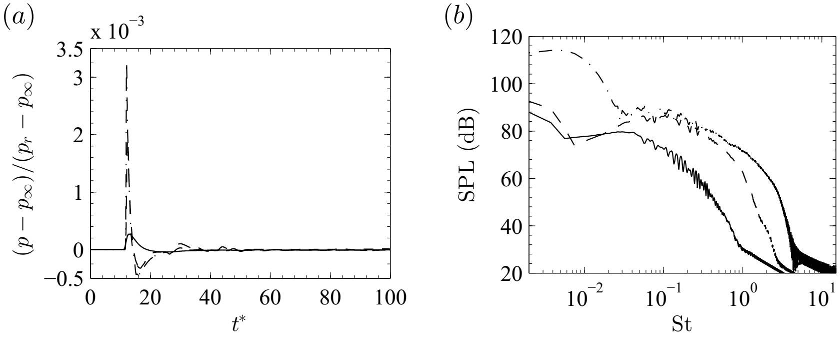

Figure 8.17: (*a*) Time series and (*b*) sound pressure level spectrum of case 1.*a*. The signal was recorded at 0° (dot-dashed), 45° (dashed) and 90° (solid).

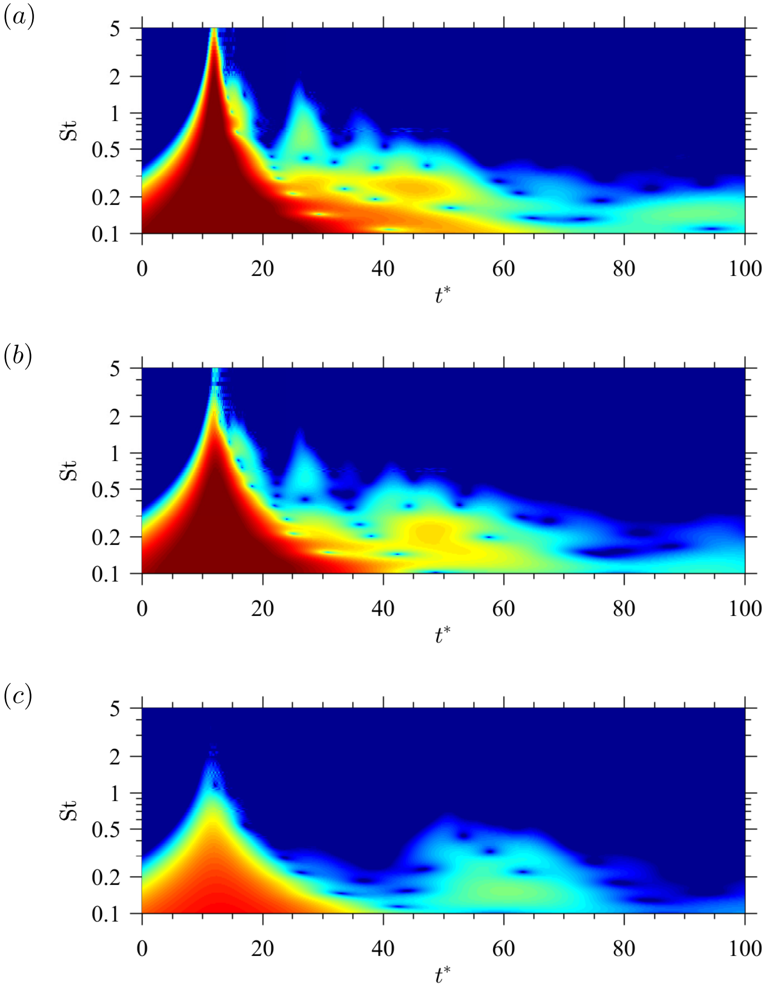

Figure 8.18: Continuous wavelet transformation coefficients in logarithmic colour scale for case 1.a. The colour-scale is in the range [60, 130] [dB]. (a) Microphone located at 0°. (b) Signal at 45°. (c) Signal at 90°.

Chapter 9

Governing parameters prediction from acoustic and optical measurements

The work corresponding to this section was presented at the International Congress on Theoretical and Computational Acoustics (ICTCA), 2015 [**J.J. Peña Fernández** and Sesterhenn, 2015d].

Once the behaviour of the system is clear and we matched the values of the governing parameters with the physical phenomena, by linking the acoustic radiation of every physical phenomenon we estimated the governing parameters from acoustic parameters.

9.1 Reynolds number

As already described in section 8.3, turbulent mixing noise is the only jet noise component where turbulence is exclusively involved. Since the Reynolds number is used to characterise turbulence in flows, it makes sense to try to predict the Reynolds number by analysing the turbulent mixing noise.

From the two components of turbulent mixing noise as proposed by Tam et al. [1996], the fine-scale similarity (FSS) spectrum shows a larger dependence on the Reynolds number, see Bailly and Bogey [2006]. The large-scale similarity (LSS) spectrum is almost independent of the Reynolds number.

It has been repeatedly reported that the peak frequency of the fine-scale similarity (FSS) spectrum is closely dependent on the Reynolds number, [Bailly and Bogey, 2006; Bogey and Bailly, 2004; Long and Arndt, 1984;

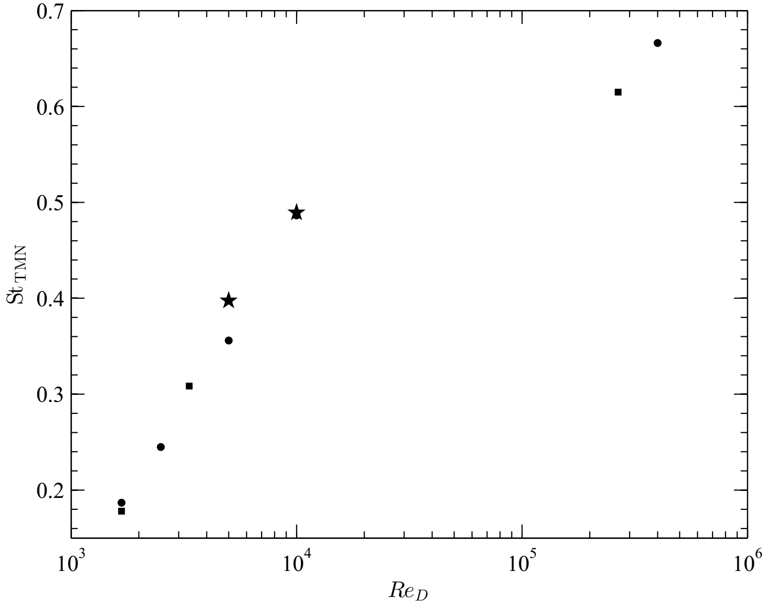

Figure 9.1: In the sideline direction, $\theta \simeq 90°$, the variation with the Reynolds number of the peak Strouhal number of the FSS spectrum is shown for jets with a Mach number of 0.9 (●) and for a Mach number of 0.6 (■). Data from Bailly and Bogey [2006]. ★ correspond to the current study, case 7.b at $Re_D = 5\ 000$ and case 7.c at $Re_D = 10\ 000$.

Lush, 1971]. This has been called the 'low Reynolds number effect'. The authors do not agree whether the correct scaling is through the Strouhal number $St = fD/u_j$, based on the fully expanded velocity u_j or on the Helmholtz number $H = fD/c_\infty$, based on the speed of sound. Our results show a better agreement with a scaling based on the Strouhal number.

In figure 9.1 the peak Strouhal number of the FSS spectra are shown for different Reynolds numbers. Cases 7.$b-c$ of this study are also represented for comparison (★) and show a good agreement.

Viswanathan [2004] reported experimentally on free jets that the limit for the so-called 'low Reynolds number effect' is about 400 000. This means that from this Reynolds number on, no changes in the acoustics of the free jet are expected when increasing this parameter.

9.2 Pressure ratio

We can easily differentiate from acoustic measurements whether a starting jet is supersonic or subsonic. The existence of broadband shock noise (BBSN) means the existence of shock-waves in the flow and therefore a supersonic flow. The supersonic flow has to be generated by a pressure ratio larger than the critical value $(p_{0r}/p_\infty)^* = ((\gamma+1)/2)^{(\gamma/(\gamma-1))}$. The peak Strouhal number $(f_p L_s/u_j)$ of BBSN radiated by the continuous jet based on the shock-cell spacing (L_s) and the eddy convection velocity $(u_c = 0.7u_j)$ was found to be unity, see Norum and Seiner [1982]:

$$1 = \frac{f_{\mathrm{BBSN}} L_s}{u_c}, \tag{9.1}$$

We want to relate this fact to the pressure ratio and for this purpose, we include the necessary information to reach the desired formulation:

$$L_s = \pi\sqrt{M_j^2 - 1}\,\frac{D_j}{\sigma_1} \tag{9.2a}$$

$$D_j = D\left(\frac{1+\frac{1}{2}(\gamma-1)M_j^2}{1+\frac{1}{2}(\gamma-1)M_d^2}\right)^{\frac{\gamma+1}{4(\gamma-1)}}\left(\frac{M_d}{M_j}\right)^{1/2} \tag{9.2b}$$

$$M_j = \left(\frac{2}{\gamma-1}\left(\left(\frac{p_{0r}}{p_\infty}\right)^{\frac{\gamma-1}{\gamma}} - 1\right)\right)^{1/2} \tag{9.2c}$$

$$\frac{c_j}{c_\infty} = \sqrt{\left(1+\frac{\gamma-1}{2}M_j^2\right)^{-1}\frac{T_r}{T_\infty}} \tag{9.2d}$$

where $\sigma_1 \approx 2.404826$ is the first root of the zero order Bessel function.

And this leads to the direct relationship between the Helmholtz number of the maximum amplitude within the BBSN and the pressure ratio.

$$\frac{f_{\mathrm{BBSN}} D}{c_\infty} = \frac{\sigma_1}{\pi\sqrt{M_j^2-1}}\,\frac{D}{D_j}\,\frac{c_j}{c_\infty}, \tag{9.3}$$

means that the peak Helmholtz number $(f_p D/c_\infty)$ based on the BBSN peak frequency, the diameter of the nozzle (D) and the speed of sound for the unbounded chamber (c_∞) decreases by increasing the pressure ratio, see figure 9.2*a* and equation (9.3). In this way, through a measured BBSN peak Strouhal number, the pressure ratio (p_{0r}/p_∞) of the jet can be estimated. This approach can be only used in the supersonic case but, in order to be able to estimate the pressure ratio in the subsonic cases, we present another different approach that regards both subsonic and supersonic jets.

For pressure ratios lower than $(p_{0r}/p_\infty)^*$, the jet is purely subsonic and only TMN is emitted. In this case, we can analyse how both (LSS and FSS) spectra change with the pressure ratio. According to Tam et al. [1996], the peak sound pressure level of the LSS spectrum ($\mathrm{SPL}_{\mathrm{LSS}}$) and the FSS spectrum ($\mathrm{SPL}_{\mathrm{FSS}}$) change with the temperature ratio reservoir to unbounded chamber (T_r/T_∞) and the pressure ratio as:

$$\mathrm{SPL}_{\mathrm{LSS}} = 35 + \frac{46}{\left(\frac{T_r}{T_\infty}\right)^{0.3}} + 10\log\left[M_j\sqrt{\frac{T_r}{T_\infty}\left(1+\frac{\gamma-1}{2}M_j\right)}\right]^{n_{LSS}}, \tag{9.4a}$$

$$M_j = \left(\frac{2}{\gamma-1}\left(\left(\frac{p_{0r}}{p_\infty}\right)^{\frac{\gamma-1}{\gamma}}-1\right)\right)^{\frac{1}{2}}, \tag{9.4b}$$

$$n_{LSS} = 10.06 - 0.495\frac{T_r}{T_\infty}, \tag{9.4c}$$

and

$$\mathrm{SPL}_{\mathrm{FSS}} = 43.2 + \frac{19.3}{\left(\frac{T_r}{T_\infty}\right)^{0.62}} + 10\log\left[M_j\sqrt{\frac{T_r}{T_\infty}\left(1+\frac{\gamma-1}{2}M_j\right)}\right]^{n_{FSS}}, \tag{9.5a}$$

$$M_j = \left(\frac{2}{\gamma-1}\left(\left(\frac{p_{0r}}{p_\infty}\right)^{\frac{\gamma-1}{\gamma}}-1\right)\right)^{\frac{1}{2}}, \tag{9.5b}$$

$$n_{FSS} = 6.4 + \frac{1.2}{\left(\frac{T_r}{T_\infty}\right)^{1.4}}, \tag{9.5c}$$

respectively. This method is valid for both subsonic and supersonic cases. Figure 9.2*b* shows experimental and analytical data and the good agreement with the current results.

Another possibility is to use imaging techniques. We can measure the relative length of the first shock-cell to the nozzle diameter (L_s/D) and use the existing correlations in the literature to relate it to the fully expanded Mach number and therefore to the pressure ratio. We use the correlation of Schulze [2011], taken from Tam et al. [1985]:

$$\frac{L_s}{D} = \frac{\pi}{\sigma_1}\sqrt{M_j^2-1}\,\frac{D_j}{D}, \tag{9.6a}$$

$$\frac{D_j}{D} = \left(\frac{1+\frac{1}{2}(\gamma-1)M_j^2}{1+\frac{1}{2}(\gamma-1)M_d^2},\right)^{\frac{\gamma+1}{4(\gamma-1)}} \tag{9.6b}$$

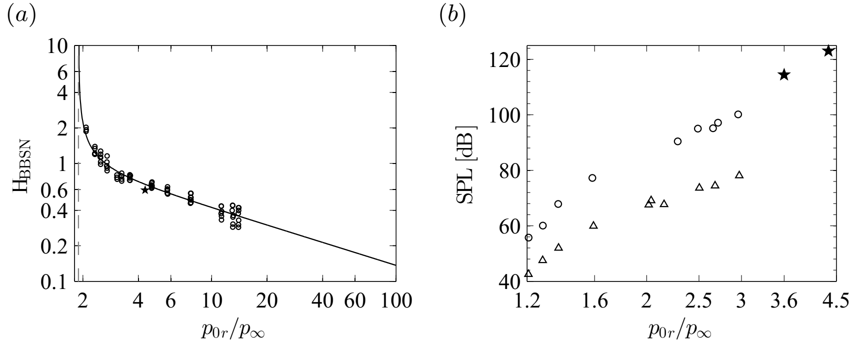

Figure 9.2: (*a*) Variation of the BBSN peak Helmholtz number with p_{0r}/p_∞ for $A^*/A = 1$. The dashed grey line correspond to $(p_{0r}/p_\infty)^*$ for $\gamma = 1.4$. ■ Norum and Seiner [1982]. (*b*) Variation of the peak sound pressure level with the pressure ratio p_{0r}/p_∞. Data from Tam et al. [1996] corresponding for $T_r/T_\infty = 1$. The large-scale similarity spectra was represented by ($\circ$) and was measured at $\theta = 160°$. The fine-scale similarity spectra was represented by ($\triangle$) and was measured at $\theta = 90°$. Cases 7.*b*, *e* are represented by ★: case 7.*b* at $p_{0r}/p_\infty = 3.6$ and case 7.*e* at $p_{0r}/p_\infty = 4.35$.

where $\sigma_1 \approx 2.404826$ is the first root of the zero order Bessel function, M_d is the design Mach number (dependent mainly on the critical to exit area ratio of the nozzle).

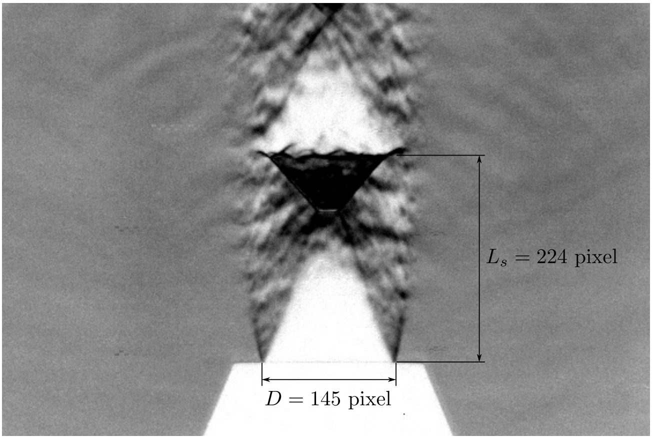

Figure 9.3: Schlieren picture of an under-expanded jet from a convergent nozzle ($A^*/A_e = 1$). $p_{0r}/p_\infty = 3.6$, $T_{0r}/T_\infty = 1$, $L/D \to \infty$, $Re_D \approx 2.52 \cdot 10^5$. Exposure time relative to characteristic time $t_{\mathrm{exp}}/(D/u_j) = 0.104$.

Figure 9.3 shows a schlieren picture where the ratio length of the first shock cell to the nozzle exit is $L_s/D \approx 224/145$. Using the correlations from the literature we get a Mach number of $M_j = 1.4833$ and a pressure ratio of $p_{0r}/p_\infty = 3.5836$. The experiment was performed with a pressure ratio of $p_{0r}/p_\infty = 3.6$, which shows a very good agreement.

For pressure ratios larger than $(p_{0r}/p_\infty)_{\text{blast}}$, a blast wave is generated. Blast waves propagate faster than the speed of sound and faster with larger pressure ratios, see section 4.1. With the knowledge of the distance between the microphone and the nozzle and the time between the release of the pressure and the reception of the blast wave at the measurement point, the Mach number of the blast wave can be computed with the help of the Rankine-Hugoniot equations and through it the pressure ratio p_{0r}/p_∞.

9.3 Dimensionless mass supply

The BBSN is radiated during the period in which the shock-waves of the trailing jet are interacting with the vortices of the shear layer. The highest frequency that BBSN radiates is related to the frequency with which two vortices are interacting with a shock-wave. The smallest frequency that BBSN radiates can be related to the duration of the supersonic stage, as explained in detail in section 8.6. From the continuous jet, we know that the lowest frequency of the BBSN is not the duration of the whole analysed record, so there exist a minimum frequency that the BBSN radiates. If the duration of the supersonic stage in the starting jet under analysis is long enough to radiate the absolute minimum BBSN frequency, there is no possibility with this method to estimate the non-dimensional mass supply. We expect that the maximum value of the non-dimensional mass supply that we can estimate with this method is approximately $L/D \sim 50$.

For subsonic jets, the previous method cannot estimate the dimensionless mass supply and therefore we use an alternative method. As shown in section 5.4, the front pressure wave shows similarity, which can be also used to estimate the non-dimensional mass supply. The normalisation variables contain the constant C, which means that collapsing a given pressure profile to the data here presented should lead to the parameter C. With the help of the estimation of the pressure ratio and assuming a temporal distribution of the inlet condition like equation (2.10), the equation (D.7) should give a good estimation of the non-dimensional mass supply.

9.4 Temperature ratio

The effects of T_{0r}/T_∞ on jet noise are still not clear for the community. Often it can be read in experimental studies that the temperature effect on jet noise is due to changes in the velocity when keeping constant the pressure ratio and therefore the Mach number, see Tanna [1977], which is clearly a coupled effect with the Reynolds number. Viswanathan [2004] reported that experimenting with hot jets, the changes found in the literature in the sound radiated are not typically due to temperature changes, but to changes in the Reynolds number, because the experiments were done with the same nozzle and pressure ratio. They found a similar spectral shape at aft angles for low subsonic jets and highly heated supersonic jets. However, they report as a general trend that the effects of heating are a broadening of the angular sector for peak radiation and a broadening of the spectral peak for aft angles.

In this work, we focused on jets with $T_{0r}/T_\infty = 1$.

Indeed, future work needs to be done to clarify the effects of the temperature ratio on the jet noise. Due to the coupling between the Reynolds number with the temperature ratio and the pressure ratio of the jet, see equation (9.7)[1], to find a suitable experimental set-up can be complex. Therefore we think further numerical work should be made in the near future in this direction.

$$Re_{D,j} = \frac{\rho_j u_j D}{\mu_j} = \frac{\rho_\infty c_\infty D}{\mu_\infty} \sqrt{\frac{2}{\gamma - 1}\left(\left(\frac{p_{0r}}{p_\infty}\right)^{\frac{\gamma-1}{\gamma}} - 1\right)} \left(\frac{p_{0r}}{p_\infty}\right)^{\frac{2\gamma}{\gamma-1}} \frac{\left(\frac{p_\infty}{p_{0r}}\right)^{\frac{\gamma}{\gamma-1}} \frac{T_{0r}}{T_\infty} + \frac{T_S}{T_\infty}}{1 + \frac{T_S}{T_\infty}} \left(\frac{T_\infty}{T_{0r}}\right)^2 \tag{9.7}$$

In this chapter we were able to predict the values of the governing parameters by linking them to acoustic properties.

Starting with the Reynolds number, there is enough evidences in the literature of the relationship between the peak frequency of the fine-scale similarity of the turbulent mixing noise with the Reynolds number, but the authors do not agree in a scaling with the Strouhal or Helmholtz number. Our results show a better agreement with the Strouhal number. [Viswanathan, 2004] reported experimentally the absence of changes in the radiated acoustics for free jets from a Reynolds number of 400 000 on.

For supersonic jets, Norum and Seiner [1982] found that the peak Strouhal number of BBSN based on the shock-cell spacing and the eddy convection velocity was one. We applied this result to predict the pressure ratio and the results agreed with data from the literature. For subsonic jets we used the model of Tam et al. [1996] in order to relate the sound pressure level of both fine and large scale components of the turbulent mixing noise with the pressure ratio and the current results show good agreement with the reported ones. We used also imaging techniques to predict the pressure ratio of free jets based on schlieren photography.

---

[1] Assuming the classical Sutherland's law for the viscosity with an exponent of 2/3 and a Sutherland temperature of T_S.

For supersonic jets with a very low non-dimensional mass supply, we related the lowest frequency of the BBSN component radiated to the duration of the supersonic stage of the jet and this to the non-dimensional mass supply to predict this last parameter. We expect to be able to predict accurately L/D for jets under $L/D = 50$ with Mach numbers of order unity.

The effects of the temperature ratio on jet noise are still not clear for the community. Viswanathan [2004] reported that the changes found in the sound radiated are not due to temperature changes, but to changes in the Reynolds number, because the experiments in the literature have been performed with the same nozzle and pressure ratio. Indeed, future work is needed to clarify the effects of the temperature ratio on the jet noise.

Chapter 10

Volcanic jets

The ejection of gas and pyroclasts from volcanoes has typically been called *plume*. In a rigorous fluid mechanics context, a plume is dominated by buoyancy. In most of the volcanic eruptions, the first stage is dominated by momentum, but it decays and leads to a stage dominated by buoyancy. This latter stage might not be present when the ash concentration is large, leading to the collapse of the jet forming a pyroclasts density current. Therefore we use the term *volcanic jets*.

Unsteadiness, compressibility, turbulence, chemical reactions and multiphase processes make volcanic jets a difficult research topic. Any of the typical approaches (analytical, experimental and numerical) are forced to make strong assumptions to face this problem.

However, individual aspects of the volcanic jet dynamics can be abstracted and scaled for experiments. Volcanic jets are commonly generated in the laboratory using a shock-tube and the main focus of the experimental work has been the link between the observed behaviour in nature with the governing parameters of the process. Kieffer and Sturtevant [1984] used Freon 12 and 22 among other gases as analog of heavy and particulate-laden volcanic gases. Anilkumar et al. [1993] investigated experimentally high-speed two-phase volcanic jets. Recently, Cigala et al. [2017] found that the maximum velocity of the pyroclasts increases with A_e/A^* (divergent nozzles) and with the temperature ratio T_r/T_∞ and it decreases with the reservoir size (L/D) and with the particle size.

Woods [1988] derived an analytical model for Plinian eruptions, with separated treatment of the momentum-driven and buoyancy-driven regions; the model was able to predict general properties of the flow such as the maximum height as a function of the initial temperature, relative sizes of the two regions (momentum- and buoyancy-driven). The main drawback of such analytical models are the strong assumptions made, typically steady flow, single phase flow and often incompressible flow. Nevertheless, this models are necessary to isolate some aspects of the dynamics for understanding.

The set of governing equations can also be solved numerically. We can relax some of the simplifications usually made by the theoretical studies. [Valentine and Wohletz, 1989] is a very good example of one of the first numerical models used based on this approach. Currently, the focus of the numerical studies is divided in two directions: (*i*) morphology of the jet in the near-field region and the release of particles into the atmosphere depending on the governing parameters of the eruption, see [Cerminara et al., 2016] and (*ii*) dispersion of particles in the atmosphere as a function of the meteorological conditions, see [Spanu et al., 2016].

Volcanoes are a perfect natural example to study the compressible starting jet and due to this a very intense collaboration with the volcanological community has been taken place during this project. In the following sections, we describe part of the outcome from the experimental work at the volcanoes in this project: the location of craters based on an acoustic array and the analysis in the frequency and time domain of volcanic eruptions.

10.1 Crater location from acoustic measurements

The work corresponding to this section was presented at the AGU Fall Meeting 2015, [Andronico et al., 2015].

During the field campaign at Mount Etna 2014 we measured the acoustics of the eruptive fissure at the flank of the North-East Crater, see section 3.3.1. We deployed three microphones at different circumferential angles around the craters covering an angle of about 120°. The objective of this study was, knowing the GPS coordinates of the three microphones, use the time of arrival of every event to the different microphones to determine the exact position of the two craters and to know which eruption was produced by which crater. Furthermore, we wanted to analyse separately the acoustic properties of the eruptions of every crater and make statistics of the eruption pattern of the different craters.

We used 3 different methodologies to locate the (11 758) eruptions that we recorded during the 2014 campaign:

1. **Vectorisation.** Assuming a location of the crater and measuring the delay of the signal at the different microphones, due to the different distance to the crater, from three microphones we can build two vectors that should intersect in the crater. We use an iterative method to converge to the final solution.

2. **Hyperbolas.** The definition of a hyperbola is the set of points,

such that for any point (P) of the set, the absolute difference of distances to two fixed points (the foci F_1 and F_2) is constant. $|PF_1| - |PF_2| = \text{constant} = 2a$. If we think about our physical problem, P would be the crater and F_1 and F_2 would be two microphones. The constant $2a$ would be the delay between the two signals converted into a distance with the speed of sound, this is, the distance that the speed of sound travels within the delay between the two signals. We had 3 microphones, so we can build two hyperbolas and the point in which these hyperbolas intersect is the location of the crater.

3. **Triangulation.** This is a classical method. Assuming that the noise waves are circumferences, we computed the location of the crater solving the intersection of these three circumferences.

Figure 10.1 shows the results obtained by the three methods. The point where we were located is denoted by 'STATION' and the three microphones are denoted with $M1$, $M2$ and $M3$. The probability density function is plotted as contours after locating more than 11 000 events.

The basic information is the same for the three plots, showing where is more probable that the craters were located. Some spurious results show the presence of wrong data, mostly due to echoes with the flank of the Mount Etna itself. Therefore the located as well the location of the echoes, which can be especially well seen in the vectorisation and triangulation methods. The two red round markers are the location of the most intense eruption that we measured, giving a very sharp edge at the measurements and therefore very accurate results. We measured the distance *in situ* between our station and the summit of the craters with laser-based distometers and we obtained 200 m, which is a very close value to the ones obtained by the acoustic measurements.

We can conclude that the three methods are able to locate the craters from acoustic measurements in a satisfactory manner.

10.2 Frequency-time domain (wavelet and STFT) analysis

Part of the work presented in this section was presented in [Stampka et al., 2014].

In order to characterise the volcanic eruptions and locate the different noise components in frequency and time, and therefore have information about the physical processes that led to this noise sources, we performed a time-frequency analysis of the signals recorded at the volcanoes. We

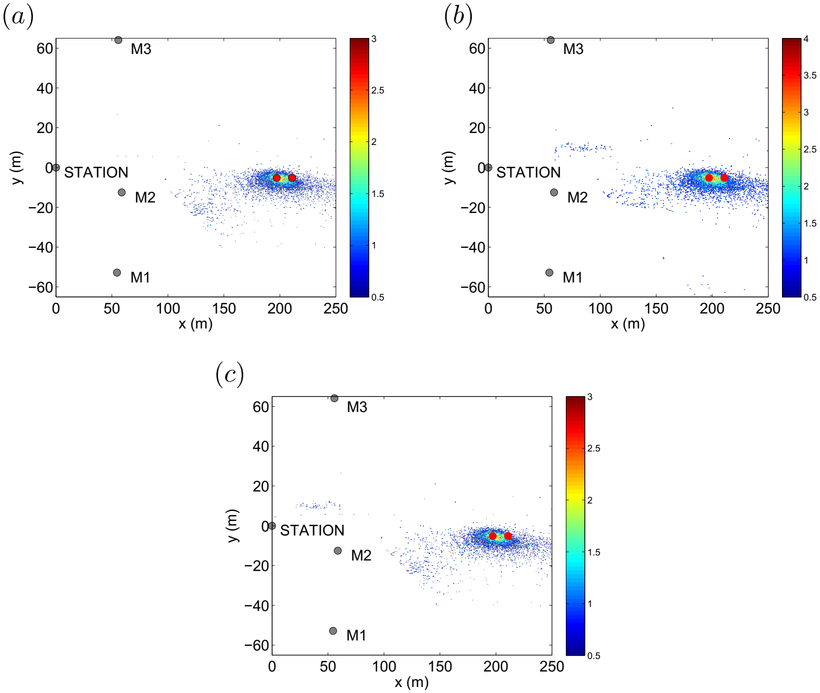

Figure 10.1: Crater location results of the eruptions measured during the mount Etna campaign in July 2014. (*a*) Vectorisation method. (*b*) Hyperbolas method. (*c*) Triangulation method.

perform both main time-frequency analyses: short-time Fourier transform (STFT) and wavelet transform.

While the STFT has a uniform resolution in frequency, the wavelet transform has an adaptive resolution, keeping constant the relative error in the frequency domain at the expense of time resolution. This is as well how human auditory perception works.

Figure 10.2 shows the spectrogram of an eruption recorded at Stromboli analysed using STFT. The Strouhal number is defined in this case as ($St = (fD_{\text{volcano}})/u_{\text{exit}}$), where $D_{\text{volcano}} = 1.5m$ is the diameter of the volcanic vent and $u_{\text{exit}} = 335m/s$ is the exit velocity of the gas phase through the volcanic vent. The diameter has been estimated from drone photographies and the velocity has been estimated assuming a sonic vent for an observed temperature of the magma with an infrared camera. The Strouhal number axis is represented in logarithmic scale and the fixed resolution can be especially well seen for low frequencies. Figure 10.3 shows the spectrogram of the same eruption recorded at Stromboli analysed using the wavelet transformation. The frequency axis is represented in logarithmic scale and the adaptive frequency resolution can be seen for low frequencies.

In figure 10.2 we see a well-defined Strouhal number, which is the upper limit of the noise radiated by this eruption of the volcano. This corresponds to a Strouhal number of about 20. The sound pressure level at higher Strouhal numbers is negligible compared to those contained in the noise signal. From the same figure, we can infer the duration of the eruption by looking at the end of the signal where the subsonic turbulent mixing noise is no longer radiated.

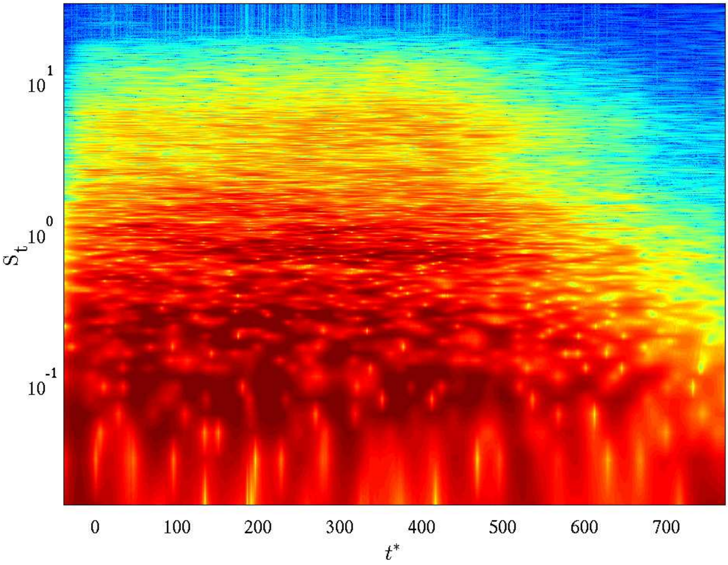

Figure 10.2: Short time Fourier coefficient contour of the acoustics recorded at Stromboli.

The same signal was analysed using the wavelet transform. The corresponding result is shown in figure 10.3. In this figure, we can identify much better the signal content for low Strouhal numbers. While in figure 10.2, for Strouhal numbers below 0.1 the frequency resolution of the STFT is too coarse, for the wavelet method (figure 10.3) the signal content can be clearly seen. From figure 10.3 we can see that for Strouhal numbers below 0.1, the amplitude of the signal decreases. The dominant Strouhal numbers are within the range $0.1 - 1$.

In this chapter we showed three very similar methods with which we could localize the position of the craters from acoustic measurements: vectorisation, hyperbolas and triangulation. The results were quantitative very similar to each other and overall successful although the presence of echoes at the wall of the mount Etna.

We analysed the same eruption measured at Stromboli using the short time Fourier transform and the wavelet transform. We conclude that the wavelet method is more convenient for this application, because it keeps constant the relative error in the frequency domain. For volcanic applications the low frequent content is crucial due to the size of the jet flowing.

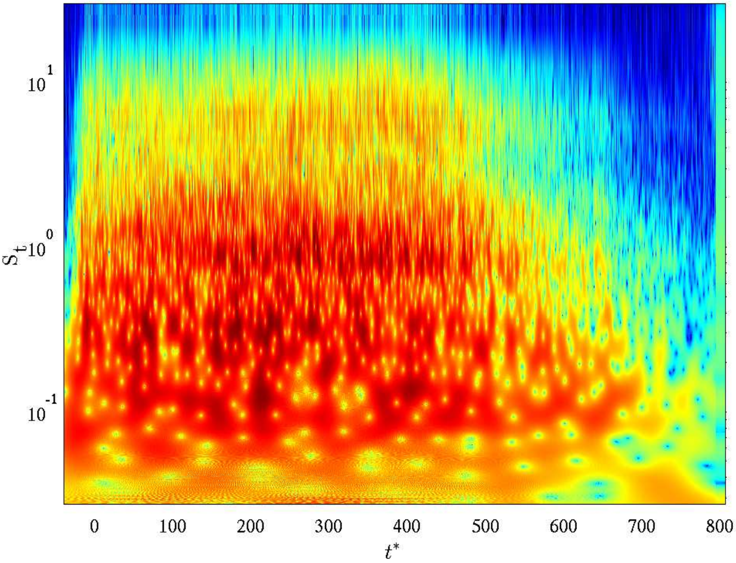

Figure 10.3: Wavelet coefficient contour of a signal recorded at Stromboli.

Chapter 11

Conclusions and perspectives

Opposed to the continuously blown jet and to the incompressible starting-decaying jet, the compressible starting-decaying jet is relatively unexplored and can be considered a new topic for the scientific community. Not only the scientific community will profit from this thesis, but also the industry, with applications in extremely different fields such as pulsejets and pulse detonation engines in the aerospace industry, air-bag devices or fuel injection in the automotive industry; aquatic locomotion or the aortic blood flow in the animal heart in biology; lava flow and volcanic jets in geological sciences and astrophysical jets in the creation of new stars. This thesis provides the first solid analysis of the compressible starting jet, giving a detailed description of the characterisation of the flow field together with the noise sources. The combination of these two aspects allows this work to give some insights to the prediction of the governing parameters from acoustic measurements. This analysis has been made mainly with a numerical approach, although experimental work was also performed to support or complement the results where appropriate.

In the first part of the thesis, the numerical background was described with all necessary details. The second part focuses on the experimental work that supports and complements the numerical results. The third part is the main body of this thesis. We examine the fluid flow and the acoustics of the compressible starting jet in detail. The most salient results are presented below.

Concerning the characterisation of the compressible jet separated by its elements we can conclude that the compression wave propagates at the speed of sound of the unbounded chamber for pressures $p_{0r}/p_\infty < 41.2$ and it is considered to be a pressure wave. For pressure ratios larger than this limit, a blast wave is generated and it moves faster than the speed of sound and faster with increasing pressure ratios. About the vortex ring dynamics, we can confirm that its axial position is a function of $(t^*)^{1/2}$ and its radius varies as $(t^*)^{1/3}$ during a considerable time interval. Moreover, it has been found that for large pressure ratios the Prandtl-Meyer expansion modifies the vortex ring radius and larger vortex rings are generated. Furthermore and surprisingly although already reported, we confirmed that compressibility makes the vortex ring to move slower.

About the effects of the turbulence level at the inflow condition, we can summarise that the jet structure remains although the presence of strong perturbations. An increase in the turbulence intensities at the inlet results in an increase of the radiated turbulent mixing noise. A side effect is, as well, a modification in the broadband shock noise due to a different interaction between the shear layer and the shock waves.

Examining the pinch-off process, the separation of the vortex ring from the trailing jet, this thesis contributes with a more general and appropriate definition of the pinch-off for compressible and turbulent cases based on a vorticity threshold $\omega_{po}/\omega_{\text{vortex}} = 0.1$. We propose a definition of the pinch-off as the creation of a region between the trailing jet and the vortex ring with a relative vorticity of $\omega_{po}/\omega_{\text{vortex}} = 0.1$ or lower. Examining the dynamics of the system vortex ring - trailing jet we found two ways in which this system interacts: the *shock - shear layer - vortex* interaction and the *shock - shear layer* interaction. They lead to two of the three principal noise components of the starting jet in the supersonic case. The former generates a strong acoustic wave few non-dimensional units after the release of the pressure. The latter is the noise generation mechanism of the broadband shock noise.

We also covered the acoustics of the starting jet. It has been found that only turbulent vortex ring radiate noise and they radiate mostly in the downstream direction. Broadband shock noise was found to be generated by the isolation of a supersonic flow region in the subsonic one; this takes place especially at the interaction of the shock waves and the shear layer but it is not exclusive.

We used the knowledge that the turbulent mixing noise is closely related to the turbulence in the jet and therefore to the Reynolds number to link a property of the turbulent mixing noise with the Reynolds number and be able to predict the latter from acoustic measurements. We confirm the results of Bailly and Bogey [2006]: the Strouhal number for the peak amplitude of the fine-scale component of the turbulent mixing noise increases with the Reynolds number. The same way, we used the result from Norum and Seiner [1982] that the Strouhal number of the broadband shock noise scales with the shock-cell spacing and the convective velocity to establish a dependency of the Helmholtz number of the peak amplitude of the broadband shock noise and the pressure ratio. We also found the similarity axes that collapse the pressure profile of the compression wave as a function of the non-dimensional mass supply, which can be used to predict this parameter.

With an array of three microphones distributed around the crater of a volcano, we were able to locate the crater from the delay of the arrival time between the microphones using three different methods: vectorisation, hyperbolas and triangulation. The three methods were successful. Analysing the noise radiated from volcanic jets in frequency-time space we found the wavelet transform to be more appropriate because it keeps the relative error constant in the frequency domain and the resolution for low frequencies is much better than the short-time Fourier transform method. The low-frequency content of volcanic jet acoustics is crucial for their analysis.

Perspectives

This thesis has shed light on the fluid flow properties and the acoustics of the compressible starting jet, but there are still some research lines that require further clarification. The first question is the limiting value of the dimensionless mass supply that leads to a trailing jet for the compressible case. It has presumably a similar value than in the incompressible case, but is is still to confirm.

We have seen that for low Reynolds numbers, the Kelvin-Helmholtz instabilities of the shear layer are not fully developed when reaching the first shock wave, while for high Reynolds numbers they do. Because of this, there is a strong interaction between the trailing jet and the vortex ring. The second question is the critical Reynolds number for which this interaction takes place.

The third and most important question still to answer is the effect of the jet temperature ratio on the jet acoustics. Further work in the near future is needed in this direction and numerical studies can clarify the changes in the noise generation mechanisms due to the jet temperature.

Appendices

Appendix A

Gas dynamics of nozzle flows

A nozzle is a very efficient device to convert the internal energy of the flow into kinetic energy. The fluid expands and accelerates through the nozzle isentropically and hence with high efficiency.

The basic principle of a nozzle is based on how channel flows evolve with a variable cross area:

- a subsonic flow:
  - expands and accelerates through a convergent channel
  - compresses and decelerates through a divergent channel
- a supersonic flow:
  - compresses and decelerates through a convergent channel
  - expands and accelerates through a divergent channel

and this is the reason to choose a convergent channel to expand the flow until sonic conditions and then a divergent channel to expand further into supersonic. From the one-dimensional isentropic conservation of mass, momentum and energy (Euler equations), we see that the performance of a nozzle depends mainly on its geometry (exit to critical area ratio[1]). The area-Mach number function can be derived obtaining:

$$\frac{A}{A^*} = \left(\frac{2}{\gamma+1}\right)^{\frac{\gamma+1}{2(\gamma-1)}} \frac{1}{M}\left(1+\left(\frac{\gamma-1}{2}M^2\right)\right)^{\frac{\gamma+1}{2(\gamma-1)}} \tag{A.1}$$

---

[1] The critical area A^* is the one in which through an isentropic process the flow would reach sonic speed ($M = 1$).

also plotted for $\gamma = 1.4$ in figure A.1.

We can relate through an isentropic process the pressure and the Mach number with:

$$\frac{p}{p_r} = \left(1 + \frac{\gamma - 1}{2} M^2\right)^{-\frac{\gamma}{\gamma - 1}}. \tag{A.2}$$

To increase the Mach number in the subsonic flow ($M < 1$) in figure A.1, A^*/A has to be increased. Since A^* is fixed, we have to decrease A. We find the opposite behaviour in the supersonic regime: to increase the Mach number we need to decrease A^*/A following figure A.1, and since A^* is fixed we need to increase A.

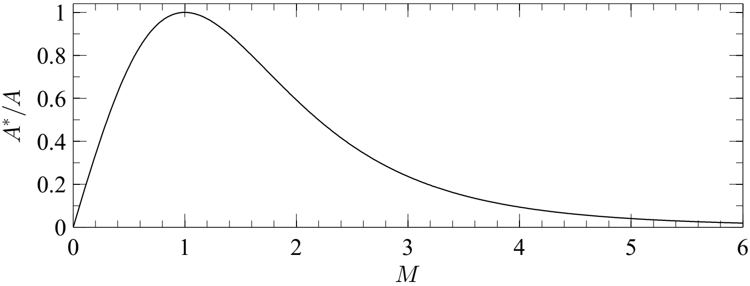

Figure A.1: Area - Mach number function for $\gamma = 1.4$. See equation (A.1).

The combination of a convergent subsonic nozzle with a divergent supersonic nozzle is usually called '*de Laval nozzle'*.

In the divergent part of a Laval nozzle, we might have shock waves. The Mach number and pressure jump over a normal shock wave is given by:

$$M_2^+ = \sqrt{\frac{(\gamma - 1)(M_e^+)^2 + 2}{2\gamma(M_e^+)^2 - (\gamma - 1)}} \tag{A.3a}$$

$$\frac{p_2^+}{p_e^+} = \frac{2\gamma(M_e^+)^2 - (\gamma - 1)}{\gamma + 1}. \tag{A.3b}$$

Minimal example:

Here we present an example with a general geometry (summarised in table A.1) with which we explain the principles of the Laval nozzle. The most important of these parameters is the exit to critical area ratio A_e/A^*.

The geometry of the nozzle defines the shape of the curves in figure A.2, but the values at the nozzle exit depend only on the area ratio A_e/A^*.

Assuming a constant reservoir pressure (p_r = const), we decrease the pressure in the chamber where the nozzle injects the flow to describe the different working regimes:

Table A.1: Parameters of the nozzle geometry used for the example.

Parameters	Value	Description
A_0/A^*	4	Inlet to critical area ratio
$\left.\frac{\partial D}{\partial(x/L)}\right\|_0$	0	Straight inlet
$\left.\frac{\partial D}{\partial(x/L)}\right\|_{x^*/L}$	0	Straight critical section
A_e/A^*	16	Outlet to critical area ratio
$\left.\frac{\partial D}{\partial(x/L)}\right\|_1$	0	Straight outlet

(a.) $p_e = p_r$. Quiescence conditions. This condition is represented in figure A.2 by the horizontal black dashed line at $p/p_r = 1$ and $M = 0$.

(b.) M_e^-. The subsonic solution of equation (A.1). It defines the fastest isentropic subsonic flow. Using equation (A.2) we obtain the nozzle exit pressure p_e^-.
For this condition, the flow reaches $M = 1$ at the throat for the first time and the narrowest cross section becomes the critical section A^* from this point on. This condition is also called *choking*, which means that the mass flow rate through the throat will not increase by increasing the exit to reservoir pressure ratio. This condition is represented in figures A.2$b-c$ by the solid black line.
For exit pressures between p_r and p_e^- there is isentropic subsonic flow in the whole nozzle, accelerating from the reservoir until the throat, but not reaching a sonic speed at this section, and then decelerating from the throat until the exit because of the divergent channel in subsonic regime. An example of this condition is represented in figures A.2$b-c$ by the solid blue line from the reservoir to the nozzle exit.
For exit pressures below p_e^-, there is supersonic flow after the critical section, leading the divergent part of the nozzle to a supersonic expansion. For slightly lower exit pressures than p_e^-, a normal shock wave is located close to the throat converting the flow into subsonic and leading to a subsonic deceleration until the exit. For lower exit pressures, the normal shock wave is located closer to the nozzle exit and the part of the divergent nozzle in supersonic flow is longer, reaching larger Mach numbers and leading to stronger shock waves and larger total pressure losses. One of these curves is represented in figures A.2$b-c$ by the combination of a solid black line from the reservoir to the critical section, then a red line from the critical section to the position of the shock wave, the vertical dashed black line represents the jump over the shock wave and the blue line as the subsonic compression until the nozzle exit. The strongest shock wave is located

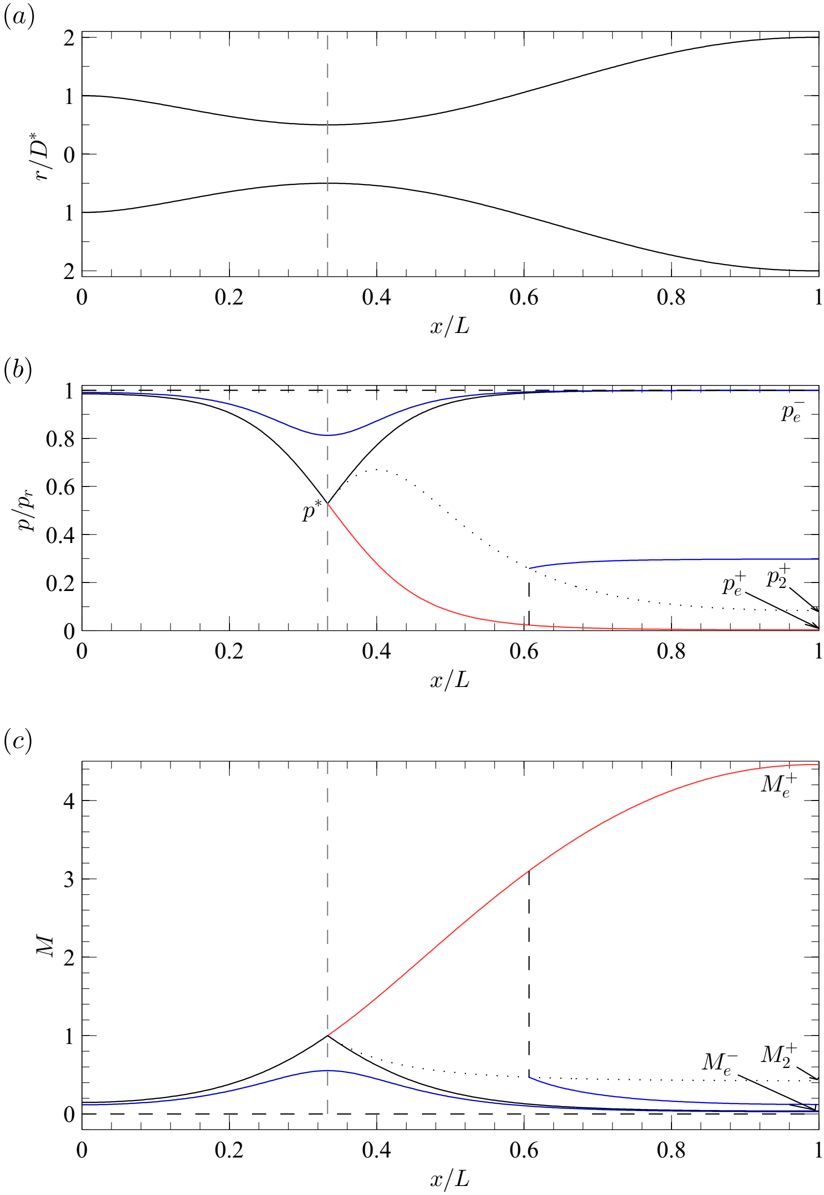

Figure A.2: (*a*) Geometry of the Laval nozzle used in this example. (*b*) Pressure distribution along the nozzle axis. (*c*) Mach number distribution along the nozzle axis.

exactly at the nozzle exit and its incoming Mach number (M_e^+) can be therefore computed from A_e/A^*.

(c.) M_e^+. The supersonic solution of equation (A.1). It defines the isentropic supersonic flow. Using equation (A.2) we obtain the corresponding nozzle exit pressure p_e^+.
For this condition, the nozzle ejects supersonic flow isentropically expanded until the pressure of the surroundings. This is the design condition of the Laval nozzle. This working regime is the most efficient. This condition is represented in figures A.2$b-c$ by the combination of the solid black line from the reservoir to the critical section and the solid red line until the nozzle exit.
For a pressure at the surrounding slightly larger than p_e^+, the nozzle (through its geometry) expanded the flow 'too much' (and therefore the name *over-expanded*) and it has to be compressed back to match the surroundings. This compression takes place through an oblique shock wave at the lip of the nozzle, but the flow inside the nozzle does not change. For larger surrounding pressures, the angle of the oblique shock wave increases, increasing as well its strength and the total pressure losses. The strongest shock wave that can take place is a normal shock located at the lip of the nozzle, being the same case as in the end of the previous point.
For surrounding pressures below p_e^+, the nozzle expanded the flow 'too less' (and therefore the name *under-expanded*) and it has to be expanded further until reaching the pressure at the surroundings. This takes place through a supersonic expansion, this is a PRANDTL-MEYER expansion fan.

Summarising, for a specific value of A_e/A^* in equation (A.1) we get two Mach numbers: M_e^- and M_e^+, which describe the limits between the different working regimes of the Laval nozzle. For exit Mach numbers below M_e^- the flow is purely subsonic in the nozzle and for larger ones, there is a part where there is supersonic flow. M_e^+ is the isentropic supersonic exit Mach number and it defines the limit between the over-expanded and the under-expanded regime. The upper limit of the over-expanded regime is the Mach number behind a normal shock with incoming Mach number M_e^+ given by equation (A.3a). The lower value of the under-expanded flow would be to expand into the vacuum. As it can be noted in this paragraph, equation (A.1) plays a crucial role in the nozzle flow dynamics and all the information about its working regimes can be obtained from this equation and the only parameter A_e/A^*.

The convergent nozzle is a particular case of all Laval nozzle flows in which $A_e/A^* = 1$. This leads to $M_e^+ = M_e^- = 1$ and $p_e^+ = p_e^- =$

$((\gamma+1)/2)^{\frac{\gamma}{(\gamma-1)}}$. For this particular case, both solutions collapse and there is only one limit between the working regimes, the isentropic flow until sonic conditions at the nozzle exit. Below this exit Mach number, the flow in the whole nozzle is subsonic. Above this working regime, the exit Mach number remains at unity, but the flow is under-expanded and just after the nozzle exit a Prandtl-Meyer expansion fan takes place. Note that in the convergent nozzle, the over-expanded flow cannot take place since it would not expand until supersonic flow, it would remain subsonic.

Appendix B

Fully expanded conditions

As a reference to study jet flows we typically use the *fully expanded conditions*. A compressible flow exiting a nozzle does not always have the same pressure than in the ambient. Depending on the geometry and the operating regime, the pressure at the nozzle exit can be higher than in the ambient (under-expanded) or lower (over-expanded). When the flow exits the nozzle and develops further, it reaches the ambient pressure at some point, and we call this fully expanded conditions, see figure B.1. In this way, we can merge the study of over-expanded and under-expanded nozzle flows taking the same reference in both cases. Typically are this conditions denoted with a subscript $(\,\cdot\,)_j$.

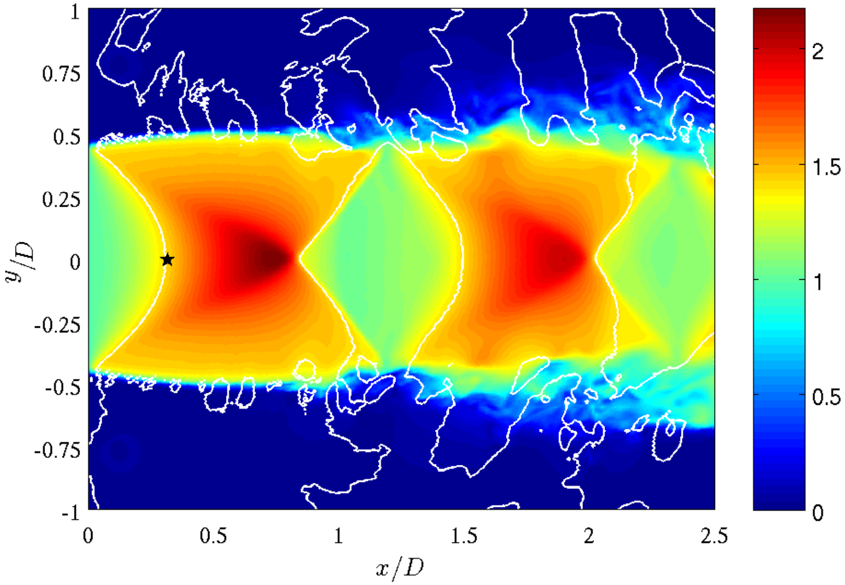

Figure B.1: Fully expanded conditions in a jet. The Mach number was plotted in colour and the white lines represent the ambient pressure (p_∞). The black star represents the fully expanded conditions.

Appendix C

Quasi-steady reservoir motion

In this chapter we describe the discharge of a reservoir by integrating the continuity equation using a $0D$ approach. We also link the state at the reservoir isentropically to the nozzle exit and the fully expanded conditions to have a global overview of the process.

The continuity equation for the one-dimensional adiabatic motion of a charge-discharge of a reservoir is given by:

$$\frac{d\left(\rho_r V\right)}{dt} \pm \dot{m} = 0 \tag{C.1}$$

where ρ_r is the density inside the reservoir, V is the volume of the reservoir and $\dot{m}$ is the mass-flow rate through the nozzle. The case with '$+$' corresponds to the discharge and the case with '$-$' corresponds to the charge of the reservoir.

From here on, we have to differentiate between two different cases: sonic choked nozzle and subsonic nozzle. Of course, the real application will switch from one solution to another depending on the set-up and the corresponding parameters.

C.1 Subsonic nozzle

When the nozzle is not choked, the mass-flow rate is not constant at the throat. The mass-flow rate is not constant and it depends on the pressure ratio between the reservoir and the unbounded chamber

$$\dot{m} = \rho_e u_e A_{\text{throat}}. \tag{C.2}$$

Relating the nozzle exit velocity with the conditions inside the reservoir via the speed of sound, we can write the mass-flow rate as

$$\dot{m} = A_{\text{throat}} M_e \sqrt{\gamma p_r \rho_r} \left(1 + \frac{\gamma - 1}{2} M_e^2\right)^{-\frac{\gamma+1}{2(\gamma-1)}} . \tag{C.3}$$

Relating the variables inside the reservoir with the stagnation ones we get

$$\begin{aligned} \dot{m} = A_{\text{throat}} \sqrt{\gamma p_{0r} \rho_{0r}} \left(\frac{\rho_r}{\rho_{0r}}\right)^{\frac{\gamma+1}{2}} \\ \left[\frac{2}{\gamma+1} \left(\frac{p_\infty}{p_{0r}}\right)^{\frac{\gamma+1}{\gamma}} \left(\frac{\rho_{0r}}{\rho_r}\right)^{\gamma+1} \left[\left(\frac{p_{0r}}{p_\infty}\right)^{\frac{\gamma+1}{\gamma}} \left(\frac{\rho_r}{\rho_{0r}}\right)^{\gamma-1} - 1\right]\right]^{\frac{1}{2}} . \end{aligned} \tag{C.4}$$

Plugging the mass-flow rate into the continuity equation C.1, we get

$$\begin{aligned} \left[\left(\frac{\rho_r}{\rho_{0r}}\right)^{\gamma-1} - \left(\frac{p_\infty}{p_{0r}}\right)^{\frac{\gamma-1}{\gamma}}\right]^{\frac{1}{2}} d\left(\frac{\rho_r}{\rho_{0r}}\right) = \\ = \frac{-A_{\text{throat}}}{V} \sqrt{\frac{\gamma p_{0r}}{\rho_{0r}}} \sqrt{\frac{2}{\gamma-1} \left(\frac{p_\infty}{p_{0r}}\right)^{\frac{\gamma+1}{\gamma}}} \left(\frac{p_{0r}}{p_\infty}\right)^{\frac{\gamma-1}{2\gamma}} dt. \end{aligned} \tag{C.5}$$

and integrating we finally get to a relationship for the density ratio over time

$$\begin{aligned} \frac{-2\left(\frac{\rho_r}{\rho_{0r}}\right)\sqrt{1 - \left(\frac{p_\infty}{p_{0r}}\right)^{\frac{\gamma-1}{\gamma}} \left(\frac{\rho_r}{\rho_{0r}}\right)^{1-\gamma}}}{(\gamma-3)\sqrt{\left(\frac{\rho_r}{\rho_{0r}}\right)^{\gamma-1} - \left(\frac{p_\infty}{p_{0r}}\right)^{\frac{\gamma-1}{\gamma}}}} \\ {}_2F_1\left(\frac{1}{2}, \frac{\gamma-3}{2(\gamma-1)}; \frac{5-3\gamma}{2-2\gamma}; \left(\frac{p_\infty}{p_{0r}}\right)^{\frac{\gamma-1}{\gamma}} \left(\frac{\rho_r}{\rho_{0r}}\right)^{1-\gamma}\right) \\ + \frac{2\left(\frac{\rho_r}{\rho_{0r}}\right)_{\text{initial}} \sqrt{1 - \left(\frac{p_\infty}{p_{0r}}\right)^{\frac{\gamma-1}{\gamma}} \left(\frac{\rho_r}{\rho_{0r}}\right)^{1-\gamma}_{\text{initial}}}}{(\gamma-3)\sqrt{\left(\frac{\rho_r}{\rho_{0r}}\right)^{\gamma-1}_{\text{initial}} - \left(\frac{p_\infty}{p_{0r}}\right)^{\frac{\gamma-1}{\gamma}}}} \\ {}_2F_1\left(\frac{1}{2}, \frac{\gamma-3}{2(\gamma-1)}; \frac{5-3\gamma}{2-2\gamma}; \left(\frac{p_\infty}{p_{0r}}\right)^{\frac{\gamma-1}{\gamma}} \left(\frac{\rho_r}{\rho_{0r}}\right)^{1-\gamma}_{\text{initial}}\right) = \\ = \frac{-A}{V} \sqrt{\frac{\gamma p_{0r}}{\rho_{0r}}} \sqrt{\frac{2}{\gamma-1} \left(\frac{p_\infty}{p_{0r}}\right)^{\frac{\gamma+1}{\gamma}}} \left(\frac{p_{0r}}{p_\infty}\right)^{\frac{\gamma-1}{2\gamma}} t, \end{aligned} \tag{C.6}$$

where ${}_2F_1$ is the ordinary hypergeometric function.

Minimal example:

For the sake of clarity, we show the evolution of a specific reservoir with the set of parameters summarised in table C.1.

Table C.1: Parameters of the example in the subsonic nozzle flow.

Parameter	Value	Description
p_{0r}/p_∞	1.5	Total reservoir to ambient pressure ratio
L/D	30	Non-dimensional mass supply
T_{0r}/T_∞	1	Total reservoir to ambient temperature ratio

We show in figure C.1 the pressure evolution in the reservoir for the example of a subsonic nozzle flow. The discharge of the reservoir takes place in $t^* \approx 15.19$ and the end of the process is denoted by ($\star$). At this point a pressure $p_r/p_{0r} = 1/1.5 \approx 0.66$ is reached.

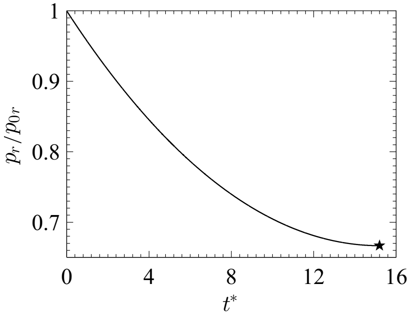

Figure C.1: Dimensionless pressure evolution in the reservoir. The end of the process is denoted by ($\star$).

The exit and fully expanded Mach numbers are shown in figure C.2. Note that both Mach numbers are identical to each other since the subsonic flow is perfectly expanded at the nozzle.

C.2 Choked nozzle

In this case, the mass-flow rate is constant (critical mass-flow rate $\dot{m}^*$) and given by the critical section area, the critical density and the critical speed of sound:

$$\dot{m}^* = \rho^* c^* A^*. \tag{C.7}$$

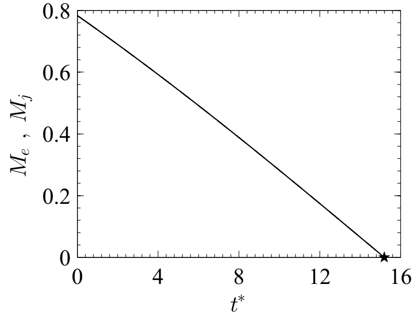

Figure C.2: Exit and fully expanded Mach number evolution in the subsonic nozzle.

Assuming ideal gas ($p = \rho RT$) and using the definition of the speed of sound ($c^2 = \gamma RT$) we can write the mass-flow rate as

$$\dot{m}^* = \sqrt{\gamma p^* \rho^*}\, A^*.$$

Using the one-dimensional isentropic theory we can relate the thermodynamic state of the flow with the stagnation conditions with:

$$\frac{T_0}{T} = \left(1 + \frac{\gamma - 1}{2} M^2\right). \tag{C.8}$$

We can relate the different thermodynamic variables using the isentropic relations: $p \sim \rho^\gamma$, $T \sim p^{\gamma/(\gamma-1)}$, etc. We can also write the critical mass-flow rate as:

$$\dot{m}^* = \sqrt{\gamma p_r \rho_r}\, A^* \left(\frac{2}{\gamma + 1}\right)^{\frac{\gamma+1}{2(\gamma-1)}}.$$

Relating the conditions in the reservoir (p_r, ρ_r) with the stagnation reservoir conditions we get to:

$$\dot{m}^* = \sqrt{\gamma p_{0r} \rho_{0r}}\, A^* \left(\frac{2}{\gamma + 1}\right)^{\frac{\gamma+1}{2(\gamma-1)}} \left(\frac{\rho_r}{\rho_{0r}}\right)^{\frac{\gamma+1}{2}}.$$

Plugging this into the continuity equation (C.1) and dividing by ρ_{0r} we get

$$\left(\frac{\rho_r}{\rho_{0r}}\right)^{\frac{-(\gamma+1)}{2}} d\left(\frac{\rho_r}{\rho_{0r}}\right) = -\frac{A^*}{V}\sqrt{\frac{\gamma p_{0r}}{\rho_{0r}}} \left(\frac{2}{\gamma + 1}\right)^{\frac{\gamma+1}{2(\gamma-1)}} dt,$$

which by integration results in

$$\frac{\rho_r}{\rho_{0r}} = \left[1 + \frac{\gamma - 1}{2}\frac{A}{V}\left(\frac{2}{\gamma + 1}\right)^{\frac{\gamma+1}{2(\gamma-1)}} \sqrt{\frac{\gamma p_{0r}}{\rho_{0r}}}\, t\right]^{\frac{-2}{\gamma-1}} \tag{C.9}$$

and therefore

$$\frac{p_r}{p_{0r}} = \left[1 + \frac{\gamma-1}{2}\frac{A}{V}\left(\frac{2}{\gamma+1}\right)^{\frac{\gamma+1}{2(\gamma-1)}}\sqrt{\frac{\gamma p_{0r}}{\rho_{0r}}}\,t\right]^{\frac{-2\gamma}{\gamma-1}} . \tag{C.10}$$

Writing this relation in dimensionless variables we get

$$\frac{p_r}{p_{0r}} = \left[1 + \frac{\gamma-1}{2}\frac{1}{L/D}\left(\frac{2}{\gamma+1}\right)^{\frac{\gamma+1}{2(\gamma-1)}} t^*\right]^{\frac{-2\gamma}{\gamma-1}} , \tag{C.11}$$

where $A/V = 1/L = D/L\ 1/D$ and $t^* = tc_{0r}/D$.

Minimal example:

We present here an example with a specific set of parameters summarised in table C.2.

Table C.2: Parameters of the example in the supersonic nozzle flow.

Parameter	Value	Description
p_{0r}/p_∞	3.6	Total reservoir to ambient pressure ratio
L/D	30	Non-dimensional mass supply
T_{0r}/T_∞	1	Total reservoir to ambient temperature ratio

Figure C.3 shows the evolution of the reservoir pressure. The nozzle remains choked until $t^* \approx 5.96$, which is denoted by (●). The process ends at $t^* \approx 15.46$, and this is denoted by ($\star$). At this point, a pressure of $p_r/p_{0r} = 1/3.6 \approx 0.278$ is reached.

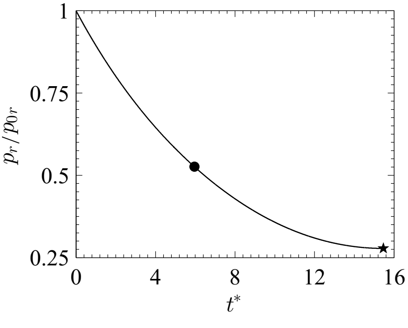

Figure C.3: Dimensionless pressure evolution in the reservoir for the supersonic nozzle flow. The end of the nozzle choking is denoted by (●). The end of the process is denoted by ($\star$).

In order to get the conditions of the nozzle exit, we can relate the reservoir conditions with the nozzle exit ones by means of:

$$M_e = \sqrt{\frac{2}{\gamma - 1}\left[\left(\frac{p_r}{p_e}\right)^{\frac{\gamma-1}{\gamma}} - 1\right]}, \tag{C.12}$$

and the same way we can relate the reservoir conditions with the fully expanded conditions:

$$M_j = \sqrt{\frac{2}{\gamma - 1}\left[\left(\frac{p_r}{p_\infty}\right)^{\frac{\gamma-1}{\gamma}} - 1\right]}. \tag{C.13}$$

Note that the exit Mach number is given by the isentropic expansion until the pressure at the nozzle exit and the fully expanded Mach number is given by the isentropic expansion until the pressure at the surroundings.

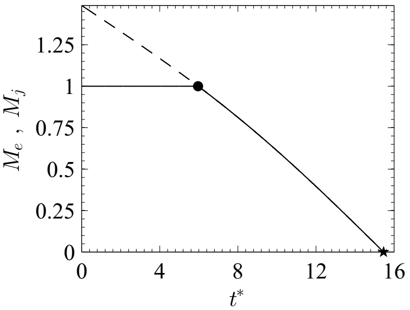

Figure C.4: Exit (solid) and fully expanded (dashed) Mach number evolution in the choked nozzle.

Figure C.4 shows the exit and fully expanded Mach numbers evolution for the example of the supersonic nozzle flow. The solid line corresponds to the exit Mach number and it shows a constant $M_e = 1$ until the nozzle is no longer choked ($t^* \approx 5.96$). From this point on, the nozzle works in the subsonic regime and it expands the flow perfectly. This makes the fully expanded and the exit Mach number to be equal to each other.

Figure C.5 shows the time evolution of the Prandtl-Meyer angle that defines this supersonic expansion. Having a Mach number of unity at the nozzle exit, we can compute the angle that the flow is deflected while expanding supersonically with equation (C.14). The flow starts in the under-expanded regime with a Prandtl-Meyer angle of $\nu_{\mathrm{PM}} \approx 11.51°$ and it decreases with time until the nozzle is no longer choked. In this point, the supersonic expansion does not take place any longer and the flow is purely subsonic.

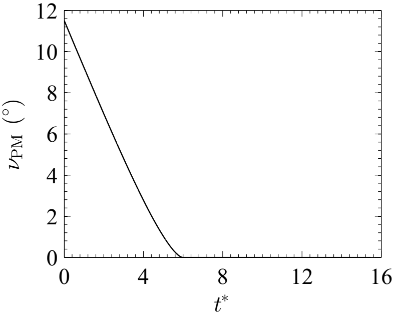

Figure C.5: Prandtl-Meyer expansion angle evolution in the choked nozzle.

$$\nu_{PM}(M) = \sqrt{\frac{\gamma+1}{\gamma-1}}\,\mathrm{atan}\left(\sqrt{\frac{\gamma-1}{\gamma+1}\left(M^2-1\right)}\right) - \mathrm{atan}\left(\sqrt{M^2-1}\right) \tag{C.14}$$

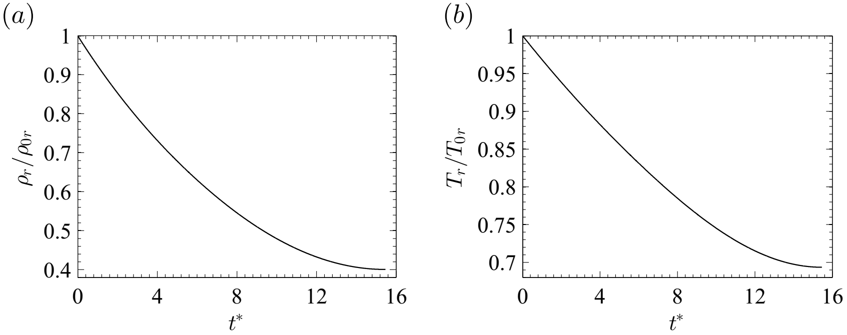

Figure C.6: Evolution of the thermodynamic state in the reservoir during the discharge of the choked nozzle. (*a*) Reservoir density and (*b*) reservoir temperature.

We focus now on the thermodynamics of the nozzle flow. During the discharge of the reservoir is the internal energy of the fluid converted into kinetic energy. Therefore, as the fluid is ejected through the nozzle, the remaining fluid inside the reservoir expands and the temperature decreases with time, see figure C.6. The same behaviour is observed in the density.

Assuming an isentropic process between the reservoir and the nozzle exit, we show in figure C.7 that while the nozzle is choked, the temperature and the density remain constant and during the subsonic stage, they increase with time until the end of the process.

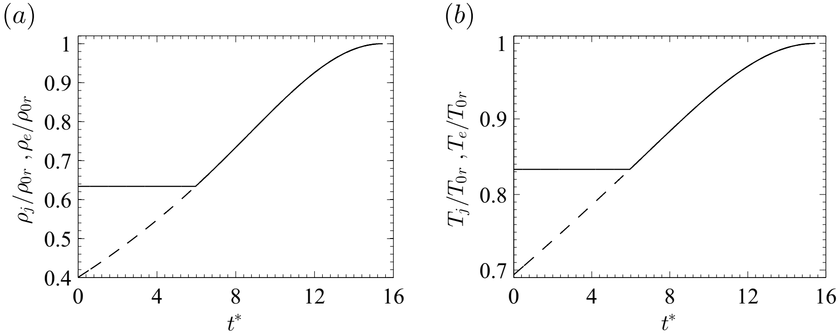

Figure C.7: (*a*) Fully expanded (dashed) and exit (solid) density evolution of the choked nozzle. (*b*) Fully expanded (dashed) and exit (solid) temperature evolution.

For the fully expanded conditions, both the temperature and the density increase monotonically with time, see figure C.7.

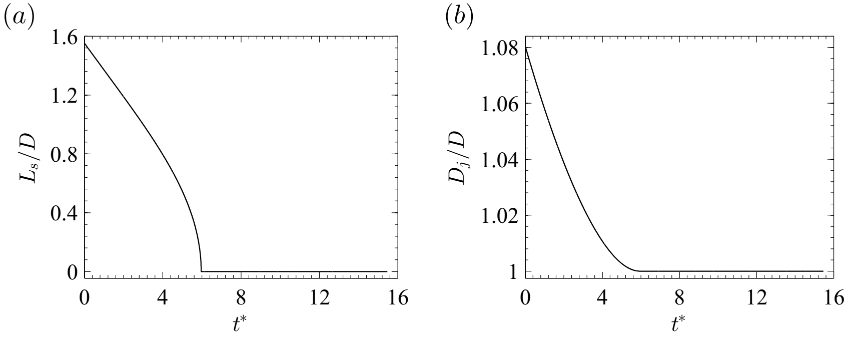

Figure C.8: Evolution of the shock-cell spacing (*a*) and fully expanded diameter (*b*) during the discharge of the choked nozzle.

In order to have a better idea about the flow characteristics, we show in figure C.8 as well the length of the first shock cell given by the correlation from Schulze [2011]:

$$L_s \approx \pi\sqrt{M_j^2 - 1}\,\frac{D_j}{\sigma_1} \tag{C.15}$$

where σ_1 is the first root of the zero order Bessel function ($\sigma_1 \approx 2.4048$).

The fully expanded diameter D_j is related to the fully expanded Mach number as follows:

$$D_j = D \left(\frac{1 + \frac{1}{2}(\gamma + 1) M_j^2}{1 + \frac{1}{2}(\gamma + 1) M_d^2} \right)^{\frac{\gamma+1}{4(\gamma-1)}} \sqrt{\frac{M_d}{M_j}} \, . \tag{C.16}$$

Its time evolution is also represented in figure C.8.

C.3 Effect of the main parameters

In this section, the effect of the main parameters in the process is analysed. As in the previous sections, a quasi-steady one-dimensional flow was assumed. The previous method was used repetitively to compute enough cases to see a trend when changing the value of the governing parameters. A base flow was chosen, which is summarised in table C.3.

Table C.3: Set of parameters chosen as base flow for this analysis.

Parameter	Value	Description
p_{0r}/p_∞	10	Total reservoir to ambient pressure
L/D	10	Non-dimensional mass supply
T_{0r}/T_∞	1	Total reservoir to ambient temperature ratio

We show the solution of the reservoir discharge for this set of parameters in figure C.9. The maximum fully expanded Mach number is approximately 2.16, decreasing with time until $t^* \approx 1.997$, where the nozzle is no longer choked; this is denoted in figure C.9*a* with (•). The rest of the process is subsonic until the end of the process at $t^* \approx 3.32$; also represented in C.9*a*, this time with ($\star$).

Figure C.10 is a contour plot of the effect of the pressure ratio over the discharge process. The colour corresponds to the fully expanded Mach number. The subsonic regime is in green, in yellow we have the sonic velocities and the red tones represent the supersonic flow. The black dotted line represents the end of the discharge and the dashed line the end of the supersonic stage.

As expected, for reservoir to ambient pressure ratios smaller than $(p_r/p_\infty)^* = 1.893$ (for $\gamma = 1.4$), the nozzle cannot be choked and there is no supersonic flow, and this is the reason the dashed line to start at 1.893. In this range of pressure ratios, the discharge takes place in a relatively long time, up to $t^* \approx 5.556$ for a $p_r/p_\infty = 2.093$, which is the longest process for this set of parameters when changing the pressure ratio. Interestingly, this pressure ratio does not correspond to the longest supersonic stage, but for $p_r/p_\infty = 5.465$. For this pressure ratio, the supersonic stage takes place in $t^* \approx 2.226$ and all other pressure ratios lead to shorter supersonic stages.

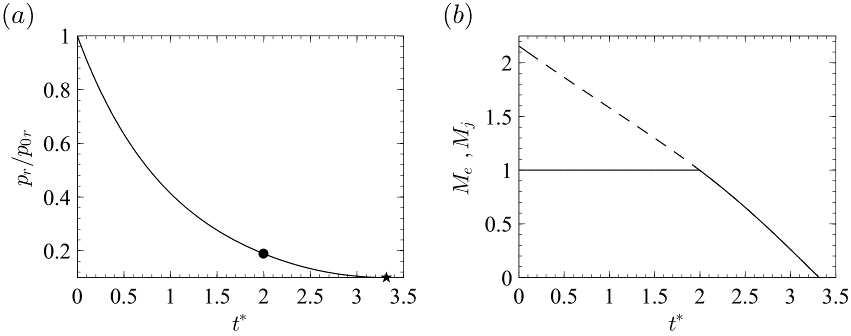

Figure C.9: (*a*) Evolution of the pressure in the reservoir. (*b*) Exit (solid) and fully expanded (dashed) Mach number evolution.

The maximum fully expanded Mach number of this plot is larger than the one of the base flow due to the higher pressure ratios used for the analysis.

Concerning the non-dimensional mass supply (L/D), figure C.11 shows the evolution of the fully expanded Mach number. As expected, we see a linear behaviour when increasing L/D. A reservoir with twice the value of L/D would be the same as discharging two reservoirs of L/D after each other and it should take twice the time. We observe the same behaviour with the sonic line. In this case, the maximum fully expanded Mach number remains the same for all cases since all of them have the same pressure ratio.

Concerning the reservoir to ambient temperature ratio, figure C.12 shows the evolution of the fully expanded Mach number for this analysis. It shows longer discharges when increasing the reservoir temperature, but actually this is only an effect of the normalisation used for the time $t^* = t\ c_{0r}/D = t\sqrt{\gamma R T_{0r}}/D$. When re-normalising the time we find no changes with the temperature ratio as shown in figure C.13. This does not strike with the current theory when looking at equation (C.11): it does not depend on the reservoir thermodynamic conditions but p_{0r}, which was kept constant in this last analysis.

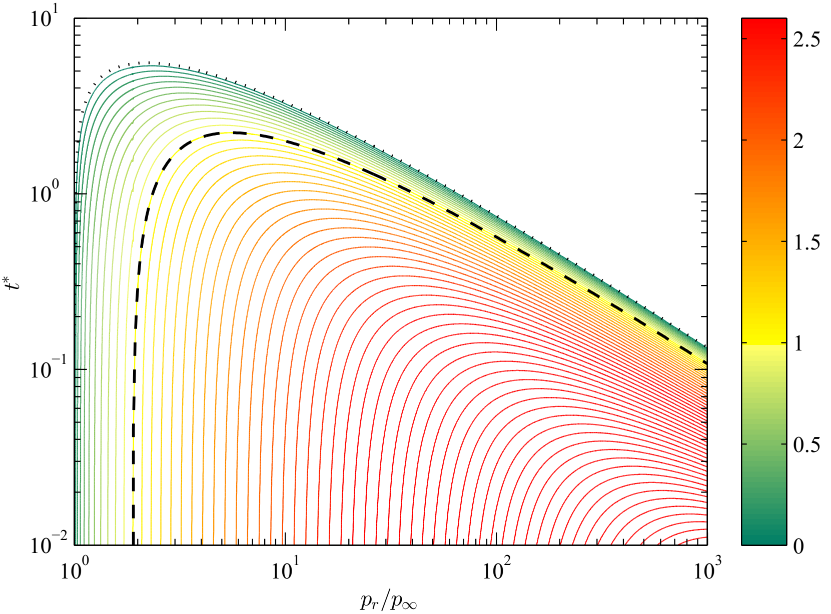

Figure C.10: Fully expanded Mach number contour plot over the pressure ratio and the non-dimensional time. The dashed black line represents the end of the supersonic flow and the black dotted line the end of the process.

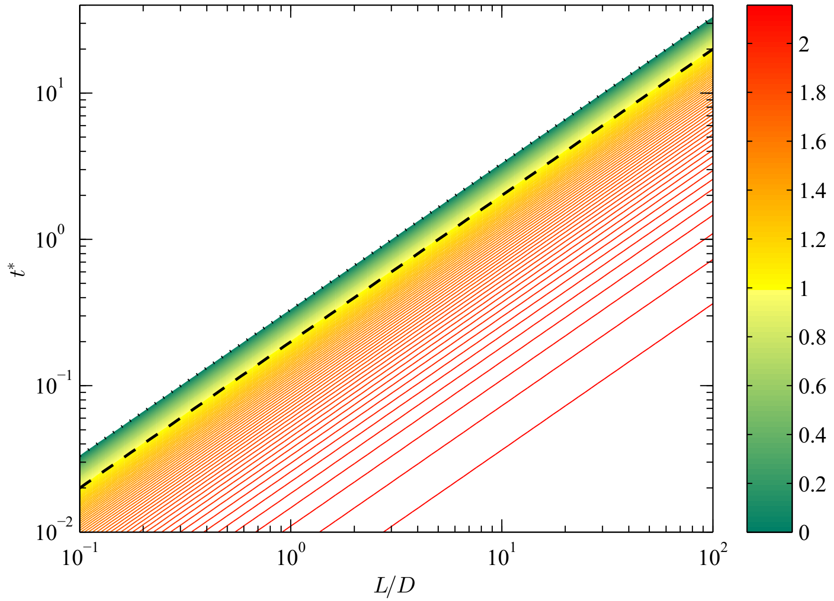

Figure C.11: Fully expanded Mach number evolution with the non-dimensional time as a function of the non-dimensional mass supply. The dashed black line represents the end of the supersonic flow and the black dotted line the end of the process.

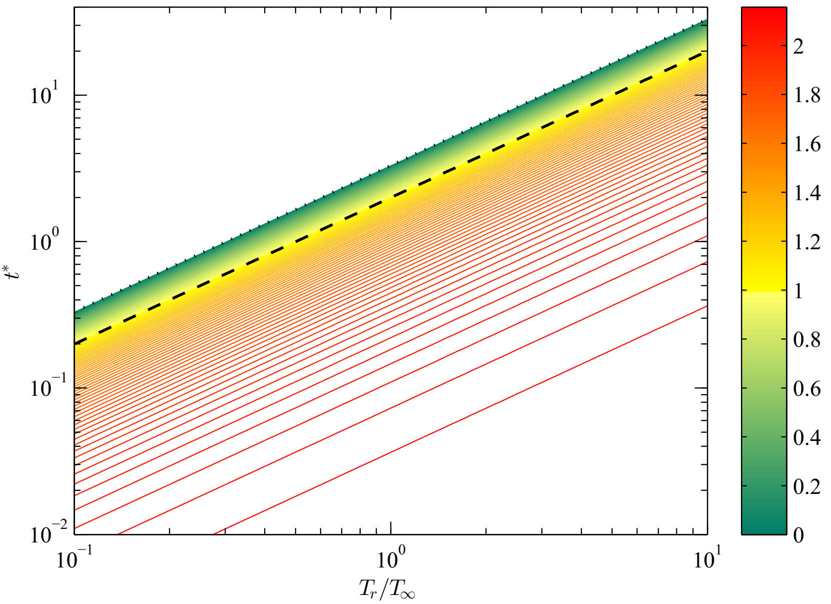

Figure C.12: Fully expanded Mach number evolution with the non-dimensional time when changing the reservoir to ambient temperature ratio. The dashed black line represents the end of the supersonic flow and the black dotted line the end of the process.

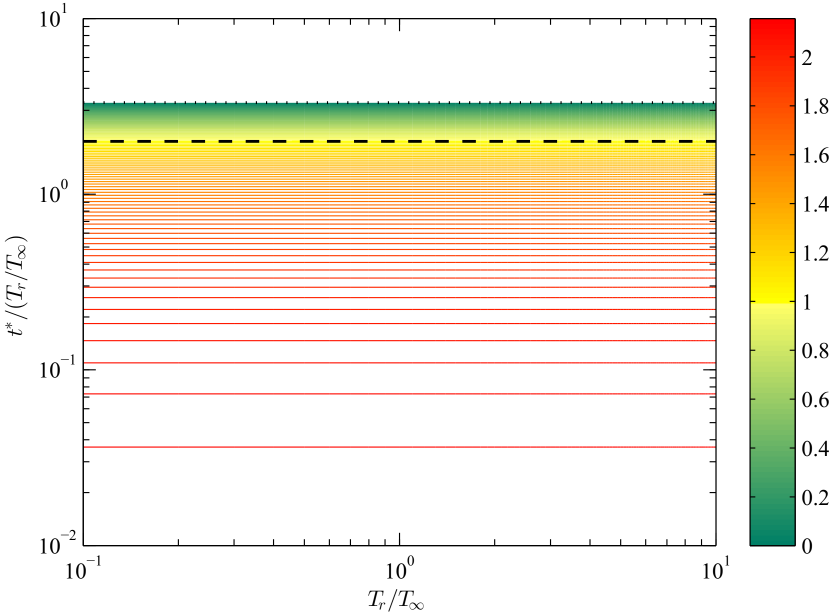

Figure C.13: Fully expanded Mach number evolution with the normalised non-dimensional time $t^*/(T_r/T_\infty)$ when changing the reservoir to ambient temperature ratio. The dashed black line represents the end of the supersonic flow and the black dotted line the end of the process.

Appendix D

Cylindrical reservoir analogy

In order to compare the results obtained in this study with those in the literature, we show in the following discussion the analogy between the main non-dimensional parameters of the cylinder-piston device typically used in the literature in the incompressible case with the discharge of a pressurised reservoir in the current study. To make this analogy we assume that the reservoir has a cylindrical form with the same diameter as the nozzle (D) in which the unknown variable is the length (L) of this hypothetical reservoir. By applying the continuity equation and integrating the mass injected (m_{injected}) into the unbounded chamber with the help of the temporal and spatial inlet condition distributions, equations (2.10) and (2.11), respectively, we compute the mass supplied through the nozzle and therefore the length of the hypothetical reservoir that would have supplied the same mass. In other words, using the continuity equation, the mass contained in the unknown reservoir at high pressure ($m_{\text{cyl,0}}$) is equal to the injected mass plus the mass contained in the reservoir at low pressure after the discharge ($m_{\text{cyl,f}}$),

$$m_{\text{cyl,0}} = m_{\text{injected}} + m_{\text{cyl,f}}. \tag{D.1}$$

We can integrate the inlet condition to know the injected mass

$$m_{\text{injected}} = \int\limits_{0}^{\infty} \int\limits_{-D/2}^{D/2} \int\limits_{-D/2}^{D/2} \rho_e(y,z,t) u_e(y,z,t)\ dy\ dz\ dt, \tag{D.2}$$

we can express the non-dimensional mass supply (L/D) as a function of the inlet condition parameters. For this purpose we write the density and velocity as a function of the main parameters:

$$u_e = M_e c_e = c_e \sqrt{\frac{2}{\gamma - 1}\left[\left(\frac{p_{0r}}{p_e}\right)^{\frac{\gamma-1}{\gamma}} - 1\right]} \tag{D.3a}$$

$$\rho_e = p_e^{\frac{1}{\gamma}} \exp\left(\frac{-s_e}{C_p}\right) \tag{D.3b}$$

so we can write the injected mass as a function of the governing parameters:

$$m_{\text{injected}} = \int_0^{\infty} \int_{-D/2}^{D/2} \int_{-D/2}^{D/2} p_e^{\frac{1}{\gamma}} \exp\left(\frac{-s_e}{C_p}\right) c_e \sqrt{\frac{2}{\gamma - 1}\left[\left(\frac{p_{0r}}{p_e}\right)^{\frac{\gamma-1}{\gamma}} - 1\right]}\, dy\, dz\, dt. \tag{D.4}$$

Having the amount of injected mass, we use the continuity equation (D.1) assuming a cylindrical shape for the reservoir:

$$\pi\left(\frac{D}{2}\right)^2 L\rho_{0r} = m_{\text{injected}} + \pi\left(\frac{D}{2}\right)^2 L\rho_{\infty}, \tag{D.5}$$

where the initial density is the total density in the reservoir (ρ_{0r}) and the final density is that of the surroundings (ρ_{∞}). By ordering the terms we have

$$\frac{\pi D^2 L}{4RT_{0r}}(p_{0r} - p_{\infty}) = \int_0^{\infty} \int_{-D/2}^{D/2} \int_{-D/2}^{D/2} p_e^{\frac{1}{\gamma}} \exp\left(\frac{-s_e}{C_p}\right) c_e \sqrt{\frac{2}{\gamma - 1}\left[\left(\frac{p_{0r}}{p_e}\right)^{\frac{\gamma-1}{\gamma}} - 1\right]}\, dy\, dz\, dt, \tag{D.6}$$

where R denotes the specific gas constant, T_r the temperature of the reservoir, s_e the entropy at the nozzle exit, c_p the heat capacity at constant pressure and c_e the speed of sound at the nozzle exit. Just by re-organising the different terms we can write the non-dimensional mass supply as a function of the governing parameters and the inlet condition parameters

$$\frac{L}{D} = \frac{4RT_r}{\pi D^3}\frac{p_\infty^{\frac{1-\gamma}{\gamma}}\, e^{\frac{-s_e}{c_p}}\, c_e}{\frac{p_{0r}}{p_\infty} - 1}\sqrt{\frac{2}{\gamma - 1}}$$

$$\int\limits_0^\infty \int\limits_{-D/2}^{D/2} \int\limits_{-D/2}^{D/2} \sqrt{\left(\frac{p_{0r}/p_\infty}{\mathrm{NPR}}\right)^{\frac{\gamma-1}{\gamma}} - 1}\, \left(\frac{p_{0r}/p_\infty}{\mathrm{NPR}}\right)^{\frac{1}{\gamma}} dy\; dz\; dt^*. \qquad \text{(D.7)}$$

Appendix E

Instrumentation

E.1 Acoustic measurements

Microphones:

PCB-378B02: Frequency range: 3.75 to 20 000 Hz; Dynamic range: 16.5 – 138 dB(A)

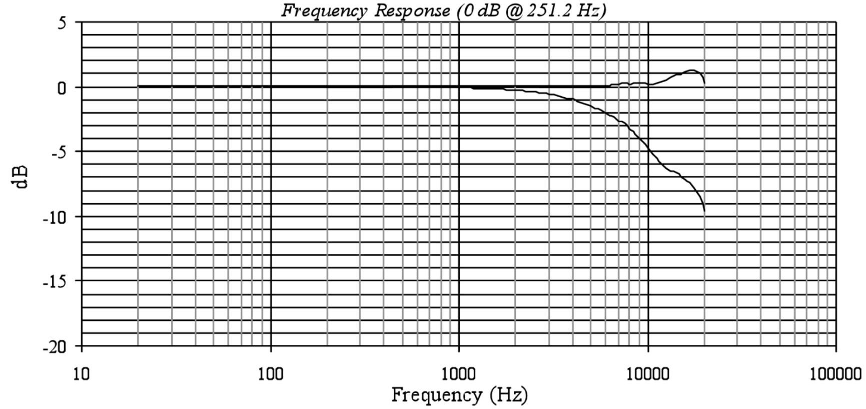

Figure E.1: Frequency response of the microphone with the grid cap at 0 degrees incidence. The top curve is the corrected free-field curve and the bottom curve is the pressure response generated by the electronic actuator. Copied from the manufacturer specifications.

G.R.A.S. 40AZ: Frequency range: 0.5 to 20 000 Hz; Dynamic range: 14 – 148 dB(A)

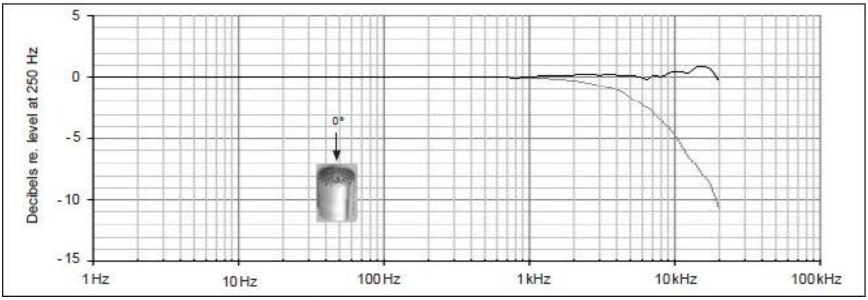

Figure E.2: Frequency response of the G.R.A.S. microphone with the grid cap at 0 degrees incidence. The top curve is the corrected free-field curve and the bottom curve is the pressure response generated by the electronic actuator. Copied from the manufacturer specifications.

E.2 Schlieren components

High-speed camera Phantom® v2512:

- 1 Megapixel sensor (1280 × 800)
- 25 Gigapixel/s throughput
- Minimum exposure time: 265 ns
- Maximum fps at (1280 × 800): 25 700
- Maximum fps at (256 × 32): 1 000 000
- Connected with 10GB Ethernet

Lenses Used:

- NIKKOR 18-140mm f/3.5-5.6G DX
- NIKKOR 200-500mm f/5.6E FX

Light source:
High power LED – CREE CXA1830-0000-000N00S430F

- 57 W
- 3060 lm
- Beam angle 115°

Publications related to this work

D. Andronico, T. Barnie, M. Burton, T. Caltabiano, A. Cannata, D. Carbone, F. Ciancitto, A. Chiarugi, D. Contrafatto, S. Corradini, F. D'Amato, E. Del Bello, F. Donnadieu, **J.J. Peña Fernández**, F. Ferrari, A. Ferro, S. Gambino, F. Greco, A. Harris, U. Kueppers, A. La Spina, P. Labazuy, L. Lodato, R. Maugeri, L. Merucci, S. Moune, R. Paris, E. Privitera, M. Queisser, T. Ricci, G. Salerno, P. Scarlato, M. Sciotto, S. Scollo, L. Scuderi, J. Sesterhenn, L. Spampinato, L. Spina, J. Taddeucci, and L. Zuccarello. Multiparametric experiment at mt. etna: investigation on both degassing and eruptive dynamics. In *AGU Fall Meeting*, 2015.

A. Cannata, E. Del Bello, U. Küppers, E. Privitera, T. Ricci, P. Scarlato, M. Sciotto, L. Spina, J. Tadeucci, **J.J. Peña Fernández**, and J. Sesterhenn. Multiparametric approach to unravel the mechanism of strombolian activity at a multivent system: Mt. etna case study. In *European Geosciences Union General Assembly (EGU)*, 2016.

V. Cigala, U. Küppers, **J.J. Peña Fernández**, J. Taddeucci, J. Sesterhenn, and D.B. Dingwell. The dynamics of volcanic jets: Temporal evolution of the exit velocity of pyroclasts from shock-tube experiments. *Submitted to Journal of Geophysical Research*, 2017.

J.J. Peña Fernández and J. Sesterhenn. Numerical simulations of a supersonic impulsively starting jet and its acoustics. In *Jahrestagung für Akustik der DEGA*, 2013a.

J.J. Peña Fernández and J. Sesterhenn. Numerical simulations of a supersonic jet at high reynolds number and its acoustic field. In 20^{th} *International Congress on Sound and Vibration (ICSV20)*, 2013b.

J.J. Peña Fernández and J. Sesterhenn. Acoustics of a short strombolian eruption. In *European Geosciences Union General Assembly (EGU)*, 2014a.

J.J. Peña Fernández and J. Sesterhenn. *Computational acoustics of supersonic turbulent free round jets*, chapter 3, Engineering and Computational Fluid Dynamics, pages 144–145. Bayerische Akademie der Wissenschaften, 2014b.

J.J. Peña Fernández and J. Sesterhenn. Noise radiated by the interaction between the shear layer, shock-wave and vortex ring in a starting free jet. In *Jahrestagung für Akustik der DEGA*, 2015a.

J.J. Peña Fernández and J. Sesterhenn. Numeric and experimental investigation of the sound generating mechanisms of a starting jet in volcanic eruptions. In *European Geosciences Union General Assembly (EGU)*, 2015b.

J.J. Peña Fernández and J. Sesterhenn. Interaction between the shear layer, shock-wave and vortex ring in a starting free jet injecting into a plenum. In 15^{th} *European Turbulence Conference (ETC15)*, 2015c.

J.J. Peña Fernández and J. Sesterhenn. Estimation of the governing parameters in an impulsively starting jet by means of acoustic measurements. In *International Congress on Theoretical and Computational Acoustics*, 2015d.

J.J. Peña Fernández and J. Sesterhenn. Acoustic signature of an impulsively starting jet. In *Physics of volcanoes*, 2015e.

J.J. Peña Fernández and J. Sesterhenn. Estimation of the main fluid flow parameters of strombolian eruptions from acoustic measurements. In *Jahrestagung für Akustik der DEGA*, 2016a.

J.J. Peña Fernández and J. Sesterhenn. *Computational acoustics of supersonic turbulent free round jets*, chapter 4, Engineering and Computational Fluid Dynamics, pages 150–151. Bayerische Akademie der Wissenschaften, 2016b.

J.J. Peña Fernández and J. Sesterhenn. Linking bubble size with the governing parameters of a volcanic jet. In *Physics of volcanoes*, 2016c.

J.J. Peña Fernández and J. Sesterhenn. Compressible starting jet: pinch-off and vortex ring-trailing jet interaction. *Journal of Fluid Mechanics*, 817:560–589, 2017a.

J.J. Peña Fernández and J. Sesterhenn. Effects of the reynolds number on the starting jet. In *Physics of volcanoes*, 2017b.

J.J. Peña Fernández, S. Bengoechea, S. Hoßbach, and J. Sesterhenn. Comparison of acoustic properties in dns of a supersonic jet with three different inlet boundary conditions. In *ERCOFTAC workshop* 9th *Direct and Large-Eddy Simulation* 9 *(DLES9)*, 2013.

J. Sesterhenn, F. Cavalcanti Miranda, and **J.J. Peña Fernández**. Direct numerical simulation of (pocket-size) volcanic jets. In *IAVCEI 2013 Scientific Assembly*, 2013.

L. Spina, J. Taddeucci, A. Cannata, M. Sciotto, E. Del Bello, P. Scarlato, U. Küppers, D. Andronico, E. Privitera, T. Ricci, **J.J. Peña Fernández**, J. Sesterhenn, and D.B. Dingwell. Multi-parametric investigation of fissure-fed multi-vent activity: the 2014 eruption of etna volcano (italy). *Bulletin of Vulcanology*, 2017.

K. Stampka, J. Sesterhenn, C. Graurock, and **J.J. Peña Fernández**. Arraymessung von ausbrüchen des vulkans stromboli. In *Jahrestagung für Akustik der DEGA*, 2014.

J. Taddeucci, J. Sesterhenn, P. Scarlato, K. Stampka, E. Del Bello, **J.J. Peña Fernández**, and D. Gaudin. High-speed imaging, acoustic features and aeroacoustic computations of jet noise from strombolian (and vulcanian) explosions. *Geophysical Research Letters*, 2014.

P.Y. Tournigand, J. Tadeucci, **J.J. Peña Fernández**, D. Gaudin, J. Sesterhenn, P. Scarlato, and E. Del Bello. Retrieving eruptive vent conditions from dynamical properties of unsteady volcanic plume using high-speed imagery and numerical simulations. In *European Geosciences Union General Assembly (EGU)*, 2016.

Bibliography

N. A. Adams and K. Shariff. A high-resolution hybrid compact scheme for shock-turbulence interaction problems. *Journal of Computational Physics*, 127:27–51, 1996.

D. Anderson, J. Tannehill, and R. Pletcher. *Computational Fluid Mechanics and heat transfer.* Series in Computational and Physical Processes in Mechanics and Thermal Sciences. Hemisphere Publishing, 1984. ISBN 9781560320463.

A.V. Anilkumar, R.S.J. Sparks, and B. Sturtevant. Geological implications and applications of high-velocity two-phase flow experiments. *Journal of Volcanology and Geothermal Research*, 56:145–160, 1993.

C. Bailly and C. Bogey. Current understanding of jet noise-generation mechanisms from compressible large-eddy-simulations. In *Direct and Large-Eddy Simulation VI*, pages 39–48. Springer, 2006.

C.G. Ball, H. Fellouah, and A. Pollard. The flow field in turbulent round free jets. *Progress in Aerospace Sciences*, 50:1–26, 2012.

E. Becker. *Gas dynamics.* Academic Press, 1968.

C. Bogey and C. Bailly. Investigation of subsonic jet noise using les: Mach and reynolds number effects. In 10^{th} *AIAA/CEAS Aeroacoustics Conference*, 2004.

C. Bogey, C. Bailly, and D. Juvé. Noise investigation of a high subsonic, moderate reynolds number jet using a compressible large eddy simulation. *Theoretical and Computational Fluid Dynamics*, 16(4):273–297, 2003.

C. Bogey, N. de Caqueray, and C. Bailly. A shock-capturing methodology based on adaptative spatial filtering for high-order non-linear computations. *Journal of Computational Physics*, 228(5):1447 – 1465, 2009.

C. Bogey, O. Marsden, and C. Bailly. Large-eddy simulation of the flow and acoustic fields of a reynolds number 10 5 subsonic jet with tripped exit boundary layers. *Physics of Fluids*, 23(3):035104, 2011.

C. Bogey, O. Marsden, and C. Bailly. Influence of initial turbulence level on the flow and sound fields of a subsonic jet at a diameter-based reynolds number of 105. *Journal of Fluid Mechanics*, 701:352–385, 006 2012.

M. Cerminara, T.E. Ongaro, and A Neri. Large eddy simulation of gas-particle kinematic decoupling in volcanic plumes and pyroclastic density currents by using the equilibrium-eulerian approach. In *SIMAI 2016*, 2016.

C. Cimarelli, M. A. Alatorre-Ibargüengoitia, U. Kueppers, B. Scheu, and D.B. Dingwell. Experimental generation of volcanic lightning. *Geology*, 42:79–82, 2014.

H. Darcy. *Les fontaines publiques de la ville de Dijon.* Victor Dalmont, 1856.

N. Didden. On the formation of vortex rings: Rolling-up and production of circulation. *Zeitschrift für angewandte Mathematik und Physik ZAMP*, 30(1):101–116, 1979.

P.E. Dimotakis. The mixing transition in turbulent flows. *Journal of Fluid Mechanics*, 409:69–98, 4 2000.

J.B. Freund, S.K. Lele, and P. Moin. Direct numerical simulation of a Mach 1.92 jet and its sound field. *4th AIAA/CEAS Aeroacoustics Conference, AIAA journal*, 2000.

L. Gao and S. C. M. Yu. A model for the pinch-off process of the leading vortex ring in a starting jet. *Journal of Fluid Mechanics*, 656:205–222, 8 2010.

L. Gao and S. C. M. Yu. Starting jets and vortex ring pinch-off. In D. T. H. New and S. C. M. Yu, editors, *Vortex Rings and Jets*, volume 111 of *Fluid Mechanics and Its Applications*, pages 1–31. Springer Singapore, 2015.

M. Gharib, E. Rambod, and K. Shariff. A universal time scale for vortex ring formation. *Journal of Fluid Mechanics*, 360:121–140, 4 1998.

A. Glezer. The formation of vortex rings. *Physics of Fluids*, 31(12):3532–3542, 1988.

J.C. Hermanson, R. Dugnani, and H. Johari. Structure and flame length of fully-modulated, turbulent diffusion flames. *Combustion Science and Technology*, 155(1):203–225, 2000.

R. Ishii, H. Fujimoto, N. Hatta, and Y. Umeda. Experimental and numerical analysis of circular pulse jets. *Journal of Fluid Mechanics*, 392:129–153, 8 1999.

S. James and C. K. Madnia. Direct numerical simulation of a laminar vortex ring. *Physics of fluids*, 8(9):2400–2414, 1996.

H. Johari, M. Rose Q. Zhang, and S. Bourque. Impulsively started turbulent jets. *AIAA Journal*, 35:657–662, 1997.

Lord Kelvin. The traslatory velocity of a circular vortex ring. *Phil. Mag.*, 33:511–512, 1867.

S.W. Kieffer and B. Sturtevant. Laboratory studies of volcanic jets. *Journal of Geophysical Research*, 89:8253 – 8268, 1984.

C.M. Kim, E.A. Krejsa, and A. Khavaran. Significance of shock structure on supersonic jet mixing noise of axisymmetric nozzles. *AIAA journal*, 32(9):1920–1923, 1994.

H. Kleine, C.V. Le, K. Takehara, and T.G. Etoh. Time-resolved visualization of shock-vortex systems emitted from an open shock tube. *Journal of Visualization*, 13(1):33–40, 2010.

A.M. Kuethe. Investigations of the turbulent mixing regions formed by jets. *Journal of Applied Mechanics*, 11(3):87–95, 1935.

S.K. Lele. Compact finite difference schemes with spectral-like resolution. *Journal of Computational Physics*, 1992.

C. Liess. Experimentelle Untersuchung des Lebenslaufes von Ringwirbeln. *Tech. Rep. Max-Planck-Institut für Strömungsforschung Göttingen*, 82, 1978.

T. T. Lim and T. B. Nickels. Vortex rings. In S.I. Green, editor, *Fluid Vortices*, volume 30 of *Fluid Mechanics and Its Applications*, pages 95–153. Springer Netherlands, 1995.

D.F. Long and R.E.A. Arndt. Jet noise at low reynolds number. *AIAA Journal*, 1984.

P.A. Lush. Measurements of subsonic jet noise and comparison with theory. *Journal of Fluid Mechanics*, 1971.

T. Maxworthy. The structure and stability of vortex rings. *Journal of Fluid Mechanics*, 51:15–32, 1 1972.

D.W. Moore. The effect of compressibility on the speed of propagation of a vortex ring. *Proceedings of the Royal Society of London A*, 397:87–97, 1985.

T. D. Norum and J. M. Seiner. Broadband shock noise from supersonic jets. *AIAA Journal*, 20:68–73, 1982.

T.D. Norum. Screech suppression in supersonic jets. *AIAA journal*, 1983.

J. Panda. Shock oscillation in underexpanded screeching jets. *Journal of Fluid Mechanics*, 363:173–198, 1998.

G. Pawlak, C. Marugan Cruz, C. Martinez Bazan, and P. Garcia Hrdy. Experimental characterization of starting jet dynamics. *Fluid Dynamics Research*, 39(11-12):711–730, 2007.

A. Powell. On the mechanism of chocked jet noise. *Proc. Phys. Soc. B.*, 66: 1039–1056, 1953.

H. Ran and T. Colonius. Numerical simulation of the sound radiated from a turbulent vortex ring. *International Journal of Aeroacoustics*, 8(4): 317–336, 2009.

F. Ricou and D.B. Spalding. Measurements of entrainment by axisymmetric turbulent jets. *Journal of Fluid Mechanics*, 11:21–32, 8 1961.

M. Rosenfeld, E. Rambod, and M. Gharib. Circulation and formation number of laminar vortex rings. *Journal of Fluid Mechanics*, 376:297–318, 12 1998.

P. Ruden. Turbulente Ausbreitungsvorgänge im Freistrahl. *Naturwissenschaften*, 21(21-23):375–378, 1933.

IL. Ryhming. Analysis of unsteady incompressible jet nozzle flow. *Zeitschrift für angewandte Mathematik und Physik*, 24(2):149–164, 1973.

P. G. Saffman. The velocity of viscous vortex rings. In *Aircraft wake turbulence and its detection*, pages 9–10, 1971.

M. D. Salas and A. Iollo. Entropy jump across an inviscid shock wave. *Theoretical and Computational Fluid Dynamics*, 8(5):365–375, 1996.

J. Schulze. *Adjoint based jet-noise minimization.* PhD thesis, Technische Universität Berlin, 2011.

J. Seiner, J Manning, and M. Ponton. The preferred spatial mode of instability for a mach 2 jet. *AIAA journal*, 1986.

J. M. Seiner and J. C. Yu. Acoustic near-field properties associated with broadband shock noise. *AIAA journal*, 22:1207–1215, 1984.

J. Sesterhenn. A characteristic-type formulation of the navier-stokes equations for high order upwind schemes. *Computers and Fluids*, 30(1):37–67, 2000.

K. Shariff and A. Leonard. Vortex rings. *Annual Review of Fluid Mechanics*, 24(1):235–279, 1992.

A. Spanu, M.M. Vitturi, and S. Barsotti. Reconstructing eruptive source parameters from tephra deposit: a numerical study of medium-sized explosive eruptions at etna volcano. *Bulletin of Volcanology*, 78:1–19, 2016.

C. K. W. Tam. Supersonic jet noise. *Annual Review of Fluid Mechanics*, 27(1):17–43, 1995.

C. K. W. Tam and H. K. Tanna. Shock associated noise of supersonic jets from convergent-divergent nozzles. *Journal of Sound and Vibration*, 81 (3):337 – 358, 1982.

C. K. W. Tam, M. Golebiowski, and J. M. Seiner. On the two components of the turbulent mixing noise from supersonic jets. *Aeroacoustics Conference, AIAA journal*, 1996.

C. K. W. Tam, K. Viswanathan, K. K. Ahuja, and J. Panda. The sources of jet noise: experimental evidence. *Journal of Fluid Mechanics*, 615: 253–292, 11 2008.

C.K.W. Tam and D.E. Burton. Sound generated by instability waves of supersonic flows. part 2. axisymmetric jets. *Journal of Fluid Mechanics*, 1994.

C.K.W. Tam, J.A. Jackson, and J.M. Seiner. A multiple-scales model of the shock-cell structure of imperfectly expanded supersonic jets. *Journal of Fluid Mechanics*, 153:123–149, 1985.

H.K. Tanna. An experimental study of jet noise part ii: Shock associated noise. *Journal of Sound and Vibration*, 50(3):429 – 444, 1977.

G. Taylor. The formation of a blast wave by a very intense explosion. i. theoretical discussion. *Proceedings of the Royal Society of London A: Mathematical, Physical and Engineering Sciences*, 201(1065):159–174, 1950.

W. Tollmien. Berechnung turbulenter Ausbreitungsvorgänge. *Zeitschrifft für Angewandte Mathematik und Mechanik*, 6:468–478, 1926.

J. Turner. The starting plume in neutral surroundings. *Journal of Fluid Mechanics*, 13:356–368, 7 1962.

G.A. Valentine and K.H. Wohletz. Numerical models of plinian eruption columns and pyroclastic flows. *Journal of Geophysical Research*, 94:1867–1887, 1989.

K. Viswanathan. Aeroacoustics of hot jets. *Journal of Fluid Mechanics*, 516:39–82, 2004.

P. O. Witze. The impulsively started incompressible turbulent jet. *Sandia Laboratories Report, SAND80-8617*, 1980.

P.O. Witze. Hot-film anemometer measurements in a starting turbulent jet. *AIAA Journal*, 1983.

A.W. Woods. The fluid dynamics and thermodynamics of eruption columns. *Bulletin of Volcanology*, 50:169–193, 1988.

M.Y. Zaitsev, V.F. Kopiev, and A.N.Kotova. Representation of the sound field of a turbulent vortex ring as a superposition of quadrupoles. *Acoustical Physics*, 47(6):699–706, 2001.

W. Zhao, S. H. Frankel, and L. G. Mongeau. Effects of trailing jet instability on vortex ring formation. *Physics of Fluids*, 12(3):589–596, 2000.